Versatile short-wave and mid-infrared sources based on wideband parametric conversion

THÈSE N^{O} 7602 (2017)

PRÉSENTÉE LE 26 MAI 2017

À LA FACULTÉ DES SCIENCES ET TECHNIQUES DE L'INGÉNIEUR
LABORATOIRE DE SYSTÈMES PHOTONIQUES
PROGRAMME DOCTORAL EN GÉNIE ÉLECTRIQUE

ÉCOLE POLYTECHNIQUE FÉDÉRALE DE LAUSANNE

POUR L'OBTENTION DU GRADE DE DOCTEUR ÈS SCIENCES

PAR

Adrien BILLAT

acceptée sur proposition du jury:

Prof. C. Moser, président du jury
Prof. C. S. Brès, directrice de thèse
Dr T. Sylvestre, rapporteur
Prof. L. Oxenløwe, rapporteur
Prof. L. Thevenaz, rapporteur

ÉCOLE POLYTECHNIQUE
FÉDÉRALE DE LAUSANNE
Suisse
2017

Acknowledgement

In the first place, I want to express all my gratitude to my advisor, Prof. Camille-Sophie Brès. Back in 2012, she trusted me and gave me the opportunity to spend four enriching and greatly instructive years as part of the Photonic Systems Laboratory. I am also very grateful to the committee members, Drs. Christophe Moser, Leif Øxenlowe, Luc Thevenaz and Thibaut Sylvestre for the time they spent reviewing this manuscript and the precious comments and questions they raised during the oral examination.

Then naturally come the names of people who warmly welcomed me and taught me the fundamentals of photonics during the first month of my doctorate: Drs. Steevy Cordette, Armand Vedadi and Amin Shoaie. I also wish to thank all my colleagues at PHOSL, listed here by order of arrival: Corinne Dubois, Fatemeh Alishahi, Svyatoslav Kharitonov, Yu-Pei Tseng, Deniz Aydin, Françoise Behn, Dr. Davide Grassani, Sida Xing, Dr. Can Yao, Dr. Thibault North, Simon Fabbri, Ivan Cardea, Jianqi Hu and Eirini Tagkoudi. Together with our close colleagues from the Group for Fiber Optics, they all contributed to instating a friendly and intellectually stimulating atmosphere on the workplace. Out of the PHOSL, my special thanks go to Martin Pfeiffer from the Laboratory of Photonics of Quantum Measurement, who dedicated time to teach me the basics of cleanroom microfabrication (along with the very obliging CMI staff members), and later extensively helped us in our experiments with silicon nitride.

Beyond the workplace, I naturally want to thank my parents, Florence and Pierre, and my sister Laure, for their continuous support during my journey as a student. I will finally close this acknowledgement by mentioning all my friends in Lausanne, Grenoble and beyond, who all contributed to making these four years so fulfilling.

Abstract

The mid-infrared part of the optical spectrum is of high interest in a wide range of applications such as environmental gas monitoring, contaminant detection in the chemical, food or pharmaceutical industry, medical diagnosis, or defense and security. Relevant molecules can readily be identified through their mid-infrared absorption spectra, as the latter contains the fundamental resonances of a number of pollutant and toxic gases. Consequently, spectroscopic apparatus, light detection and ranging systems or free-space communication links all benefit from the progress accomplished by mid-infrared technologies over the last years. However some shortcomings in the light emitters' capabilities are still to be addressed.

In this research work, we aim at designing a mid-infrared laser as versatile as possible and based on nonlinear wavelength conversion. The conversion relies on third-order parametric effects in waveguides such as optical fibers made of various types of glass, or integrated semiconductor chips. The objective is to leverage mature communication-band components to generate and shape the seed optical signals, then mixed in the abovementioned waveguides to down-convert them towards mid-infrared. The wavelength conversion is performed in two stages, and the first stage consists of a parametric source emitting in the short-wave infrared range.

This thesis mostly focuses on the design and realization of this stage. As such, it is closely linked to the field of nonlinear fiber optics, where the use of silica is preponderant. We build on the research performed over the last years on parametric amplifiers, initially used for the re-amplification of communication signals, and we combine it with technologies dedicated to short-wave infrared fiber lasers. As such, we are able to build wavelength tunable and modulation-capable short-wave infrared sources, significantly more powerful and versatile than previous broadband parametric converter designs. The end of the dissertation is then dedicated to the solutions that are then envisioned to realize the second conversion stage, towards mid-infrared. Very promising numerical and experimental results indicate a successful outcome to the project, confirming the validity of the laser concept.

Keywords: nonlinear fiber optics, optical fibers, optical parametric amplification, rare earth-based amplification, fiber lasers, infrared technologies.

Résumé

La partie du spectre correspondant à l'infrarouge médian trouve toute son importance pour des applications telles que la surveillance des gaz polluants, la détection de contamination dans l'industrie chimique, agroalimentaire ou pharmaceutique, le diagnostic médical ou encore la sécurité et défense. L'identification des molécules en jeu dans ces applications est immédiate grâce à leur spectre d'absorption dans l'infrarouge médian, car cette bande englobe les résonances fondamentales de nombreux composés polluants et gaz toxiques. Ainsi, les spectroscopes, la télédétection par laser ou les transmissions optiques en espace libres bénéficient tous des progrès réalisés ces dernières années dans le domaine des technologies infrarouge. Cependant les sources présentent certaines limites qui doivent encore être dépassées.

Dans ce travail de recherche, notre objectif est de concevoir un laser émettant dans l'infrarouge médian et fonctionnant sur le principe de la conversion non linéaire de longueur d'onde. Cette conversion est effectuée grâce à des processus paramétriques du troisième ordre, dans des guides d'onde telles que des fibres optiques ou des circuits photoniques intégrés. Nous souhaitons utiliser au mieux les composants déjà existant dans les bande de télécommunications pour générer et mettre en forme les signaux optiques, qui seront ensuite mélangés dans les guides d'onde en question et convertis vers l'infrarouge médian. La conversion s'effectue en deux étapes, la première d'entre elle étant assurée par un convertisseur paramétrique émettant dans l'infrarouge onde-courte.

Cette thèse se concentre principalement sur la conception et la réalisation de ce premier convertisseur. En conséquence, elle est étroitement liée au domaine de l'optique fibrée non linéaire. Nous avons combiné les avancées réalisées dernièrement dans le domaine des amplificateurs paramétriques à fibres pour les télécoms avec des technologies dédies aux lasers à fibre dans l'infrarouge onde-courte. Ainsi, nous sommes à même de fabriquer des sources modulables et ajustables en longueur d'onde dans l'infrarouge onde-courte, nettement plus puissantes et modulaires que les précédentes réalisations de convertisseurs paramétriques. La fin de la dissertation présente certaines solutions envisagées pour concevoir le deuxième convertisseur paramétrique, vers l'infrarouge médian. Des résultats numériques et expérimentaux très prometteurs laissent espérer une issue positive au projet, et démontrent la validité de notre concept.

Mot clefs : optique fibrée non-linéaire, fibres optiques, amplification paramétrique à fibre, amplification basée sur les terres rares, lasers à fibre, technologies infrarouge.

Content

Table of content

List of Figures

Chapter 1 Introduction

This introductory chapter gives the technological motivations behind the research work presented in this dissertation. For this purpose, its first section presents the applications benefiting from the use of short-wave infrared (SWIR) or mid-infrared (MIR) laser sources of moderate power. It illustrates why versatility in the laser emission characteristics is desirable. Afterward, the technological solutions currently addressing these applications' needs, mostly related to spectroscopy, are reviewed. It puts an emphasis on coherent sources emitting in the milliwatt to watt range, in continuous or pulsed regime. The last section summarizes the constitutive principles behind the MATISSE project (Middle Infrared Broadly Tunable Compact Cavity-Less Source based on Parametric Conversion). This project targets the design of such a versatile SWIR/MIR laser source exploiting wavelength conversion in third-order nonlinear media, seeded only by telecom-grade, commercially available components. The thesis organization and novel contributions to the state-of-the-art are finally quickly exposed.

1.1. Applications of lasers emitting in the short-wave and mid-infrared

The definitions of the spectral bands named short-wave infrared and mid-infrared fluctuate in literature, but a convenient way to refer to them has emerged in recent publications in the field. According to these definitions, SWIR covers wavelengths from the longer edges of the telecom bands and up to the transparency limit of silica optical fibers. Otherwise stated it roughly spans the 1.7—2.5 μm portion of the spectrum [1.1], beyond which multi-phonon absorption in silica prevents light to propagate over more than a few meters. The MIR spans from 2.5 μm to far-infrared. The far-infrared limit is set at 50 μm, according to the ISO 20473 scheme. However when speaking about MIR in this document, we will set a longer limit to about 7 μm in wavelength. It is an arbitrary choice, but the 2.5—7 μm band encompasses many strong molecular transitions, which makes it very interesting for sensing, and deserving of such a restricted definition. Moreover SWIR and MIR contain two atmospheric transmission windows where the air allows for km-long light transmission, which are fundamental for remote sensing: between 2 and 2.5 μm and between 3 and 5 μm [1.2]. Transparency of the host medium is indeed crucial for molecular spectroscopy, of which principle is described below.

Generally speaking, infrared spectroscopy takes advantage of the strong resonant transitions that molecular compounds (apart of homonuclear diatomic molecules) exhibit under illumination in this band. The absorbed frequencies correspond to the transition energies of vibrating bonds or group of bonds, which induce fluctuations in the dipole moments [1.3]. For instance the CH_2X_2 group (where X represents another atom), often found in organic compounds, can vibrate in nine different ways. Six modes involve

only the CH_2 portion: symmetric and antisymmetric stretching, scissoring, rocking, wagging and twisting. Each of these vibration modes has a characteristic excitation energy and consequently a characteristic absorption line (several lines counting the overtones). As seen from the example of carbon groups, an infrared absorption spectrum depends on the physical properties of the molecule, and each molecule can be characterized by a unique spectral signature in MIR. These spectroscopic data are very well documented and accessible from an online database run by the HITRAN project [1.4]. An excerpt of this database is shown in Fig. 1.1(a). It reports the MIR absorption lines for several simple molecular gases at room temperature, computed for a 1 cm absorption length between 2 and 12 µm. Schematically, Fig. 1.1(b) presents some MIR bond resonances as a function of the irradiation wavelength, as well as some molecular compounds associated to these resonances.

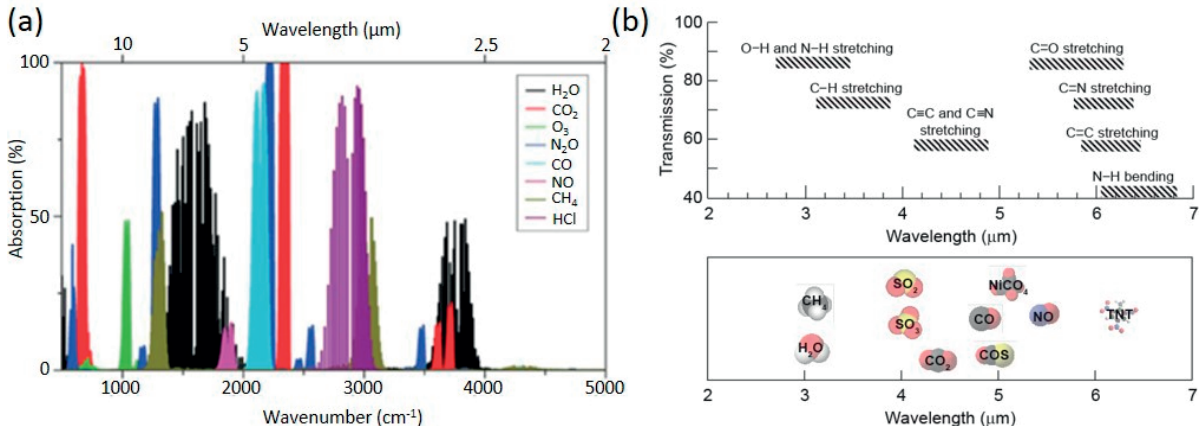

Figure 1.1: (a) Excerpt of the HITRAN database computing the MIR absorption lines of some simple molecular gases, at room temperature and for a 1 cm absorption length. (b) Correlation between molecular vibrations and sample transmission, and spectral location of the main MIR absorption lines for some relevant molecular gases.

The MIR transitions for such common gases are at least one or two orders of magnitude stronger than the corresponding overtone transitions in the near-infrared [1.5]. For this reason, narrow-band MIR sources are widely used in applications related to trace gas detection. Direct absorption spectroscopy technics simply measure the attenuation of a laser propagating in a gas sample. The laser linewidth has to be narrow enough to probe one spectral line at a time, and its central wavelength must be locked to the targeted transition. The absorption is then straightforwardly described by the Beer-Lambert law, and with long interaction lengths it is possible to detect concentrations down to the part-per-million level provided that the laser emission is stable enough [1.6]. Ultimately, parasitic effects such as the presence of laser sidemodes, or unwanted reflections in multi-pass gas cells prevent reaching of a quantum-noise limited sensitivity. More advance schemes involve optical cavities, tuned to resonate at the laser frequency when filled with gas. In a resonant cavity, the equivalent number of passes for a photon is approximated $2\frac{F}{\pi}$ for

weakly absorbing sample [1.7], and can be much higher than in a multi-pass cell. In this formula, F is the cavity finesse, defined as the free-spectral range divided by the resonance bandwidth. Cavity ring down spectroscopy is another way to employ cavity filled with gas. A continuous laser is first injected through the structure. Once the optical energy stored in the cavity is sufficient, the laser is stopped and the decay rate of light escaping the cavity is measured. The exiting light intensity decays exponentially, with a time constant that is directly related to the optical losses in the cavity, and therefore to the gas concentration. Concentrations below the part-per-billion levels become measurable with this method in MIR [1.8]. Finally, another scheme involves the measurement of the acoustic shockwave emitted by a laser heated sample (in a gaseous or solid form). A train of acoustic pulses, such as that produced in a gas by a chopped beam, constitutes an acoustic wave that can be detected using a microphone (generally a quartz fork). The concentration of gas can theoretically be estimated from the acoustic wave amplitude, while the latter disappears if the laser is detuned from the absorption line. As for other schemes, this one is extremely sensitive in conjunction with an MIR source [1.9]. On top of these laboratory-intended characterization schemes, MIR spectroscopy also finds applications for in-situ monitoring in the pharmaceutical [1.10] or food industry [1.11].

On the SWIR side, CO_2 detection probably represents the main application since this molecule features a strong overtone resonance around 2050 nm [1.12]. Given nowadays concerns about global warming, mapping the concentration of carbon dioxide in atmosphere is of primary interest. Yet, the abovementioned CO_2 line is especially advantageous since it is spectrally detuned from water absorption lines and quite insensitive to temperature fluctuations [1.13]. This type of measurement can be accomplished remotely thanks to LIDAR (Light Detection and Ranging) technology, provided that high peak power, frequency stable, tunable laser sources are used in conjunction with low-noise photodetectors [1.14]. LIDARs for atmospheric monitoring rely on backscattering processes (mostly Rayleigh and Mie scatterings) taking place in air. A small fraction of the emitted pulse is continuously back-scattered toward to the receiver along the propagation path. It allows the reconstruction of a trace, of which amplitude at a given time is proportional to the pulse power at the corresponding spatial point. The local presence of CO_2 in the probed air column will result in a pulse amplitude drop, once again proportional to the gas concentration. Embedding a LIDAR on a plane, it is possible to obtain CO_2 mappings of large air volumes [1.15]. To obtain the best range and resolution possible, wavelength tunable, highly coherent and stable pulsed lasers are desired. Moreover, since the laser has to be embedded on a vibrating vehicle like a plane or a truck, it must be as robust as possible against de-alignment and aging. From that respect, fiber lasers have a major advantage over free-space apparatus.

Alternatively, fiber communications in the SWIR represent an emerging field since the demonstration of the hollow-core fibers low-loss transmission capabilities [1.16]. Fig. 1.2 shows the cross section of such a fiber, as well as its transmission spectrum. This discovery has soon been followed by reports on high gain amplifiers covering the entire allowed band [1.17] [1.18]. Combined with the advent of extended InGaAs semiconductor lasers for the 2 µm region, this band could become a solution to address the expected capacity crunch in communication networks [1.19]. Communications at 2 µm is therefore seen as a new application field for SWIR lasers. It is therefore of interest to implement a fully tunable and modulation-capable source to serve as a data transmitter in the potential future network.

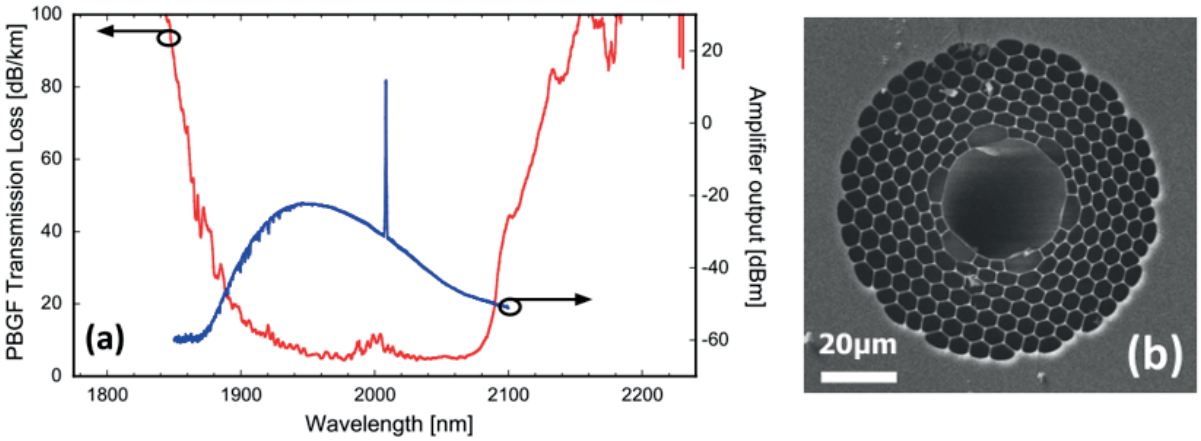

Figure 1.2: (a) Hollow-core fiber transmission loss in red, superimposed with the spectrum of the input signal at 2 µm, amplified in a thulium-doped fiber, in blue. (b) Scanning electron microscope image of the fiber cross section. Adapted from [1.16].

1.2. Overview of mid-infrared sources

In this section, we rapidly introduce the main solutions to produce temporally and spatially coherent radiation in the SWIR and MIR. Three main categories exist: doped-fiber lasers, semiconductor lasers, and parametric frequency converters. The first category addresses well the need for sources in SWIR, while the second and third categories still represent preferential solutions for MIR emission.

1.2.1. Thulium, holmium and erbium doped fiber lasers

As will be developed further in this document, thulium (Tm^{3+}) ions embedded in silica provide the fibers with a broad emission cross section, spanning roughly from 1.8 µm to 2.05 µm [1.20][1.17]. Moreover, thulium-doped silica fibers are now widely commercially available in core-pumped version making their integration in setups based on standard single mode fiber possible. Since the loss of silica fibers up to 2.05 µm is below the dB/m level, a large number of publications and commercial products related to thulium-doped fiber amplifiers and lasers have been released over the past years. Holmium (Ho^{3+}) in silica is

another solution, since it features fluorescence between 2 and 2.15 µm. This emission has also been leveraged to fabricate diversely powerful lasers [1.21]. Since Tm- and Ho-doped fibers are used intensively along the project we describe in this dissertation, a more detailed review of their underlying physics will be the topic of a further section.

In this introduction, it appears more interesting to focus on less conventional fiber hosts, such as fluoride glasses. They are non-oxide optical glasses, mainly based on zirconium fluoride (ZBLAN) or aluminum fluoride glasses. Even though material crystallization makes their drawing into fiber complex, these glasses feature low phonon energy, which prevents photon-to-phonon conversion in MIR and renders them transparent in this band [1.2]. Once doped with thulium or erbium, the fluoride matrix unlocks MIR electronic transitions that would otherwise be quenched in a silica host [1.22]. Early work focused on the 2.3 µm emission of thulium-doped fluorozirconate fibers, pumped near 800 nm. They led to the demonstration of lasers in this band [1.23]. The $^3H_4$-$^3H_5$ transition, responsible for this emission, is favored by the reabsorption of light around 1.9 µm [1.24]. Nevertheless the necessity to implement a dual-wavelength pumping scheme and the small slope efficiency hampered the development of Tm-doped fluorozirconate fiber lasers emitting at 2.3 µm. Nowadays Er:ZBLAN shows much more promises and is an active field of research. Via the $^4I_{11/2}$-$^4I_{13/2}$ transition, erbium ions emit around 2.8 µm, right in the center of the first atmospheric transparency window [1.25]. There have been various demonstrations of high power, tunable and continuous-wave (CW) lasers [1.26], in spite of a large quantum defect. Operation of mode-locked fluoride lasers in the femtosecond regime was demonstrated recently [1.27]. Moreover, thanks to dual-wavelength pumping again (at 980 nm and 1973 nm), it is possible to unlock another transition of Er^{3+} and obtain coherent emission near 3.5 µm [1.28]. Even though the tuning range is limited to some tens of nm in doped-fiber sources, they can readily pump frequency conversion stages to target wavelengths deeper in the MIR. This type of conversion is reviewed in the following section.

1.2.2. Parametric amplifiers and oscillators

Optical parametric amplifiers and oscillators (OPAs and OPOs) are versatile and convenient devices to generate coherent light at wavelengths where conventional lasers perform poorly or are unavailable, such as deep in MIR. Be they resonant or not, they are all based on the parametric conversion of NIR or SWIR pump photons into lower energy idler photons (in the MIR), with or without the help of a signal laser. Modern sources generally leverage high pulse energy such as fiber lasers near 1 µm (Yb doping), 1.5 µm (Er doping) or 2 µm (Tm doping), and crystals exhibiting large second-order nonlinearity. The combination of both permits the fabrication of wavelength-tunable sources at longer wavelengths via difference frequency generation (DFG). This process is non-negligible only if the energy and momentum conservation conditions are fulfilled. The latter means that the wave vectors of the pump, signal and idler

have to respect a certain relationship, namely $\boldsymbol{k}_{pump} = \boldsymbol{k}_{signal} + \boldsymbol{k}_{idler}$. For bulk crystals, such as barium borate or potassium titanyl phosphate, momentum conservation is generally achieved thanks to birefringence. Often in an OPA/OPO, the pump is injected without any signal, and the wavelength of both the signal and idler is selected via angle tuning [1.29]. Rotating the crystal varies the pump distribution along the ordinary and extraordinary crystal axes, changing the effective phase-matching condition.

More modern realizations generally take advantage of quasi-phase matching in periodically patterned second-order crystals, and use collinear beams. Quasi phase-matching consists in reversing the second-order tensor element sign periodically, with a period that depends on the coherence length of the targeted waves [1.30]. The power transfer then always takes place from the pump to the signal and idler. The most widespread periodically poled material is lithium niobate [1.31], of which second-order tensor elements can reach 20 pm/V [1.32]. However its transparency window does not extend further than 5 µm, which prevents deep MIR generation. Moreover the poling period is generally of the order of 30 microns, such that the domain inversion can be challenging. An interesting material recently used to overcome these limitations is gallium arsenide [1.32]. It is at least 4 times more nonlinear than lithium niobate while its transparency window reaches 16 µm. On top of this it has a lower index dispersion that enables a longer inversion period and facilitates the crystal patterning. From a power point of view and independently on the crystal used, these OPOs and OPAs can operate at a watt-level average power, with MIR pulse energy in the millijoule range. However they are bulky, require free-space optics with stringent alignment, and feature low repetition rates (in the MHz range at most). This can be a limit for embedded applications, where ruggedness and footprint are crucial. An OPO setup is illustrated in Fig. 1.3(a). Its tuning curve is shown in Fig. 1.3(b) and presents the phase matching pattern characteristic of DFG.

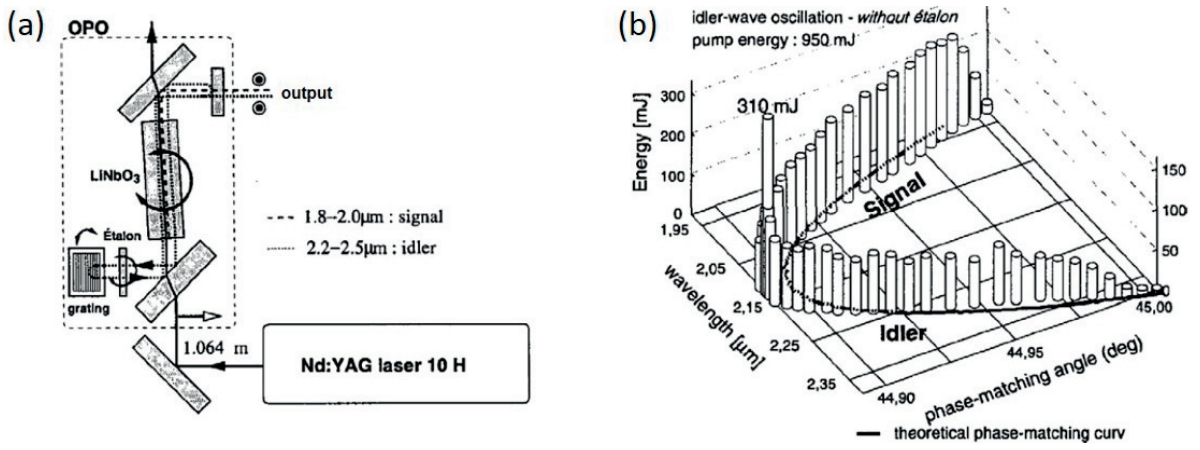

Figure 1.3: (a) Schematic diagram of a high-energy LiNbO3 parametric oscillator. (b) OPO tuning curve giving the output energy as a function of the signal or idler wavelengths, for a pump energy of 950 mJ. Adapted from [1.33].

1.2.3. Semiconductor lasers

The SWIR is well covered by GaSb-based diode lasers [1.34], which rely on classical interband transitions and are now commercially available. Type-I GaInAsSb/AlGaAsSb quantum well laser diodes show good performance at room temperature, generally up to 2.6 µm only [1.34], with a record at 3 µm [1.35]. Decreasing hole confinement and increasing Auger recombination limit their usability at longer wavelengths. However their output power can reach several tens or even hundreds of milliwatts per facet, even at room temperature. Fig. 1.4(a) shows the conduction band diagram of such a quantum well structure, while Fig. 1.4(b) presents an overview of the maximum powers attained by various CW semiconductor lasers in MIR. For longer wavelengths, stimulating radiative interband transition is made very difficult by the tiny bandgaps corresponding to MIR photon energy. For instance, a photon at 5 µm has an energy of 0.28 eV only. Until recently, only lead salt addressed this small bandgap material need. Nonetheless lead salt lasers must be operated at cryogenic temperature, and their output hardly exceeds 1 mW. But the advent of quantum cascade laser and interband cascade lasers brought new solutions to the spotlight.

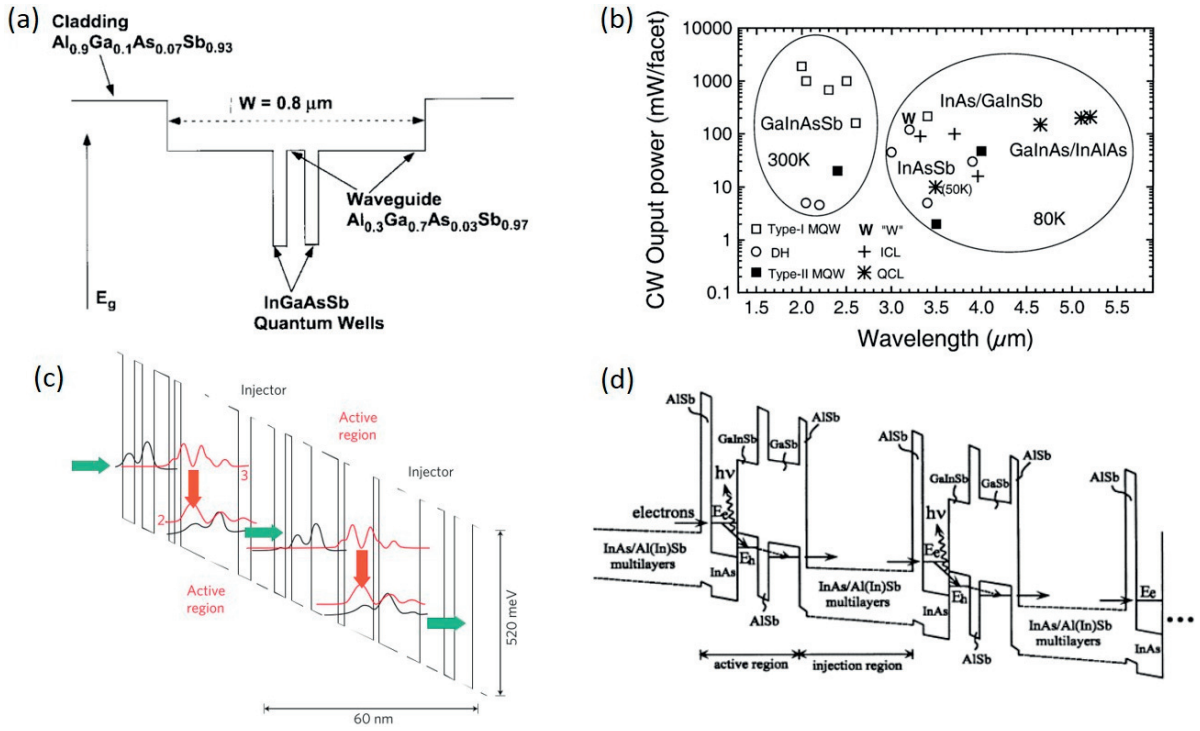

Figure 1.4: (a) Schematic of a type-I GaInAsSb/AlGaAsSb quantum well conduction band. Adapted from [1.36]. (b) Overview of the output power of semiconductor laser diodes operating CW in MIR, based on different technologies. Adapted from [1.34]. (c) Simplified schematic of a quantum cascade laser conduction band, where the radiative scatterings are indicated by red arrows. Adapted from [1.38]. (d) Schematic band diagram of a type-II interband cascade laser band structure, where radiative recombinations are indicated by curvy arrows. Adapted from [1.39].

Since their first demonstration twenty years ago [1.37], quantum cascade lasers (QCL) have undergone extensive enhancements, and can now operate at room temperature from 3 to 16 µm [1.35]. Such a spectral coverage with a single laser type is possible because the emission in QCL relies on intersubband transitions within the conduction band. Therefore, by properly engineering the many-layer heterostructure, the energy separation of the upper and lower laser level can be tailored to emit at any wavelength in MIR [1.38]. Under proper biasing of the junction, the electrons that just scattered from one energy state to a lower one in a given well subsequently tunnels to the next structure period. This cascaded process gives its name to this class of lasers, and is schematized on Fig. 1.4(c). Interband cascade laser (ICL), on the other hand, rely on interband recombination of electrons and holes. They take advantage of the broken-gap band alignment in type-II InAs/Ga(In)Sb heterostructures to reuse electrons for sequential photon emissions from successively connected active region. In each cascade stage, the thin InAs layer acts as a quantum well layer for electrons, and barrier for holes. The GaSb (or GaInSb) layer conversely acts as a well for holes and barrier for electrons, while the AlSb layer serves as a barrier for both electrons and holes [1.39]. A band structure example is shown in Fig. 1.4(d). They are now able to emit in a CW way at room temperature from 3 µm to more than 5 µm [1.40] [1.41] Overall, all these heterostructures can be integrated along with corrugated waveguides to constitute distributed feedback cavities. The cavity resonant frequency can then be adjusted by current injection or temperature control.

1.3. Project objectives and thesis organization

1.3.1. Project objectives

The abovementioned lasers are the main solutions to address MIR applications. Although these different sources all present distinct benefits, no MIR device simultaneously satisfies all the desirable specifications in terms of versatility, contrarily to transmitters in telecom bands. They have yet to fulfill the whole of the requirements imposed by the nature of LIDAR or spectroscopic applications, such as mode-hop free tuning over a wide range, narrow linewidth, and modulation capabilities, in phase and amplitude. In the scope of gas spectroscopy, a large tuning range allows for the probing of various compounds with the same instrument. However fiber lasers exhibit a tuning range restricted to the ion fluorescence band, limited to a few hundreds of nm in MIR, while wavelength selection by temperature or current control in semiconductor lasers is ultimately limited by the heterojunction engineering. Crystal-based OPOs suffer from mode-hop and are often pulsed devices, while OPAs remain bulky, vibration sensitive and not fully suitable for embedded missions. On the modulation-capability side, devices to modulate CW emitters in phase or amplitude are not as developed in MIR as in NIR. Guided-wave modulators start to emerge in laboratories [1.42], but commercial solutions are restricted to acousto-optic modulators with a limited bandwidth [1.43].

The MATISSE project objective is to address all these requirements at once, thanks to guided-wave parametric conversion based on the third-order nonlinearity of commonly found devices, such as optical fibers or CMOS compatible integrated waveguides. This project explores the synergy between widespread fiber optic telecommunication devices (tunable lasers, fiber amplifiers, fiber-connectorized modulators) and MIR parametric conversion platforms. It aims at combining two fundamental building blocks: a silica-based front end for SWIR generation and a non-silica waveguide mixer to generate MIR light. Efficient four-wave mixing (FWM, see chapter 2 for more details) in the silica front-end is exploited for the generation of a high quality pumps in SWIR, then used to pump a cascaded mixer stage specifically designed to obtain phase-matching in MIR. Figure 1.4 sketches the idea, by presenting a quantum picture of degenerate FWM and a spectral representation of the targeted conversion stages. FWM being a fully coherent and instantaneous process, to the project leverages the possibility to replicate in the MIR any modulation format imprinted on the initial pump near 1.55 µm, or alternatively on the initial signal near 1.3 µm. Moreover, due to photon energy conservation, the targeted tuning range is expected to cover several microns in the MIR. This range could be browsed only by modifying the input waves in telecom bands, with the help of reliable, narrow linewidth, and CW tunable diode lasers.

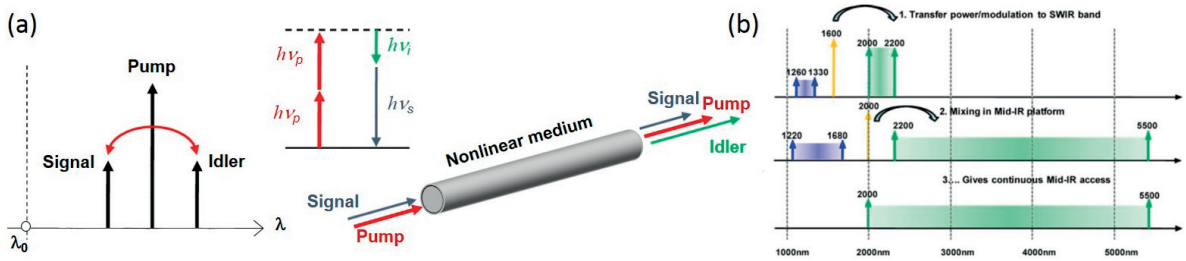

Figure 1.4: (a) Quantum mechanics picture of degenerate FWM. Two pump photons are annihilated to generate an idler and a signal photon. Energy conservation dictates the idler frequency when the signal and the pump are injected together in a nonlinear medium. (b) Schematic of the two-stage conversion towards MIR. A 1.55 µm pump and small probe around 1.3 µm are used to project power, multiple tones and modulation to SWIR. The second stage then generates arbitrary MIR wavelengths. 2000 nm is used as an illustration but any SWIR light could pump the second stage.

The work presented in this dissertation focuses on the first conversion stage based on silica fibers. In its simplest form, a parametric converter uses a single pump wave that is coupled with a signal seed into a nonlinear waveguide. Efficient amplification and wavelength conversion is achieved by satisfying phase-matching between the pump, signal and idler waves. Degenerate FWM-based wavelength conversion towards SWIR can be achieved by coupling an O-band signal (1260—1360 nm) with a C- (1530—1560 nm) or L-band (1560—1625 nm) pump into a highly nonlinear fiber (HNLF) made of silica. However, due to the stringent phase-matching constraints and achievable nonlinearity in silica, the parametric converter typically operates in an un-depleted pump regime, such that most of the pump power

remains unused. The consequential poor conversion efficiency (CE, defined as the idler output power over the signal input power) results in extremely low and usually inadequate idler powers. The operating principle of our proposed SWIR source is depicted in Fig. 1.5 and relies on the simple combination of a fiber optical parametric amplifier (FOPA) stage, together with an thulium-doped fiber amplifier (TDFA) directly pumped by the parametric pump. The absorption and emission cross sections of Tm:silica are such that the parametric pump can be used for excitation while the idler wave falls in the fluorescence band. Due to the very wide gain spectrum of TDFAs, the entire range of idlers can be amplified. This recycling of the parametric pump enables a much higher power transfer from the pump to the idler. We propose different architectures to leverage this complementarity between both optical stages.

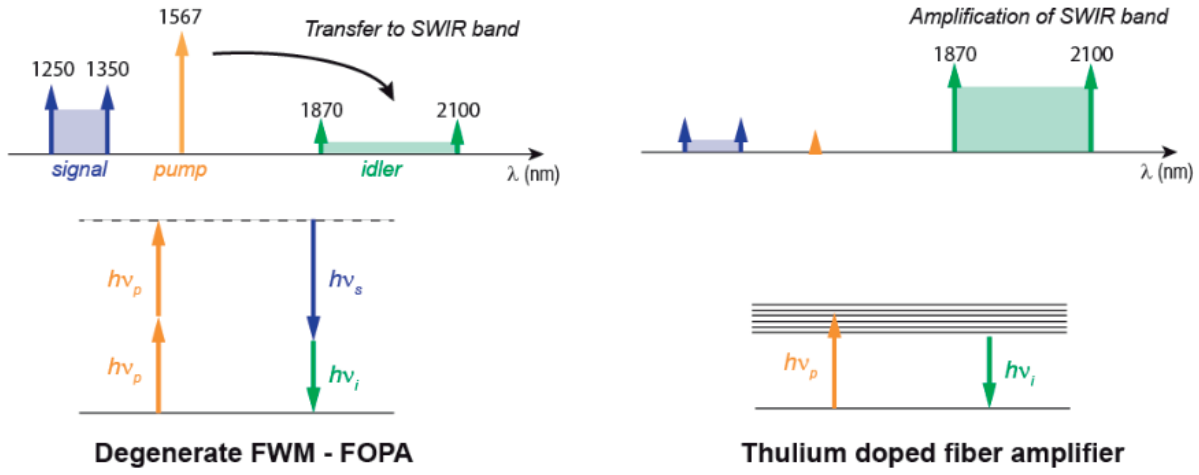

Figure 1.5: Operating principle of high efficiency SWIR source. Degenerate FWM in the FOPA leads to the generation of an initial weak idler in the SWIR. A thulium doped fiber amplifier enables the re-use of the parametric pump and the amplification of the initial idlers. The signal is also attenuated. The FOPA-TDFA architecture results in results in a versatile and energy-efficient source.

The combination of TDFAs to fiber-based parametric converters represents a major enhancement compared to setups reported over the past years. To obtain a sufficient conversion efficiency from O-band to SWIR, researchers had to use hundreds of Watts of pump power in the quasi-CW regime [1.44]. This means that the CW pump laser is chopped into long pulses (of the nanosecond order) before amplification. This represents a strong constraint in terms of source modularity. Alternative examples of parametric converters pumped by a CW laser resulted in low idler powers [1.45], even though they feature interesting capabilities in terms of data transmission. A bibliographic review about broadband FOPAs is performed in the next chapters.

1.3.2. Thesis organization

Following this general introduction, chapter 2 presents a basic review on light propagation in passive and active optical fibers. We put a special emphasis on effects arising from the silica third-order susceptibility. Brillouin scattering, a very hindering effect in the field of FOPAs, is also described. Chapter 3 numerically analyses FWM in HNLFs when the pump-signal detuning exceeds several tens of THz. In such a configuration, FWM becomes very sensitive to parameters fluctuations, and the impact of such fluctuations has to be quantified. We also introduce and evaluate protocols to characterize the dispersion of fibers. From an experimental point of view, after reporting on the performances of our FOPA-TDFA setups in CW regime in chapter 4, we demonstrate their full capability to operate in intensity-modulated and pulsed mode in chapter 5. This latter chapter also introduces a side project about wavelength conversion based on cascaded Raman scattering. In both chapter 4 and 5, the physics of thulium- and holmium-doped silica fibers is also reviewed. In chapter 6, some platforms dedicated to the second conversion stage, namely silicon-on-insulator waveguides, silicon nitride waveguides, and chalcogenide microstructured fibers, are experimentally studied. Some preliminary conclusions are drawn from these tests, and chalcogenide appears as a promising candidate for the project concretization. Finally, we close this dissertation in chapter 7.

1.4. References

[1.1] S. Moro, *Parametrically-aided sensing in the short-wave infrared frequency band and beyond*, PhD thesis, University of California in San Diego, 2011.

[1.2] G. Tao et al., "Infrared fibers," Adv. Opt. Photon. 7, 379-458 (2015).

[1.3] P. *Paula, J. Atkins. Elements of physical chemistry (5th ed.). Oxford: Oxford U.P, 2009.*

[1.4] L.S. Rothman et al., "The HITRAN 2008 Molecular Spectroscopic Database," J. Quant. Spectrosc. Radiat. Transf., 110, 533–572 (2009).

[1.5] S. Schilt et al., "Diode laser spectroscopic monitoring of trace gases. Encycl. Anal. Chem. 1–29," 1–29 (2011).

[1.6] G. Zhao, "Intensity-Stabilized Fast-Scanned Direct Absorption Spectroscopy Instrumentation Based on a Distributed Feedback Laser with Detection Sensitivity down to 4×10^{-6}," *Sensors 16*, 1544 (2016).

[1.7] G. Meijer et al., "Coherent Cavity Ring Down Spectroscopy," Chem. Phys. Lett., 217, 112 (1994).

[1.8] B. A. Paldus et al., "Cavity ringdown spectroscopy using mid-infrared quantum-cascade lasers," Opt. Lett. 25, 666-668 (2000).

[1.9] T. Berer et al., "Remote mid-infrared photoacoustic spectroscopy with a quantum cascade laser," Opt. Lett. 40, 3476-3479 (2015)

[1.10] S. Wartewig et al., "Pharmaceutical applications of Mid-IR and Raman spectroscopy," Advanced Drug Delivery Reviews 57, 1144-1170 (2005).

[1.11] M.-L. Brandily et al., "Identification of foodborne pathogens within food matrices by IR spectroscopy," Sens. Actuators B Chem. 160(1), 202–206 (2011).

[1.12] S. Moro et al., "Widely-tunable parametric short-wave infrared transmitter for CO_2 trace detection," Opt. Express 19, 8173-8178 (2011).

[1.13] R. T. Menzies et al., "Differential Laser absorption spectrometry for global profiling of tropospheric carbon dioxide: selection of optimum sounding frequencies for high-precision measurements," Appl. Opt. 42, 6569-6577 (2003)

[1.14] C. Weitkamp, *Lidar: Range-Resolved Optical Remote Sensing of the Atmosphere.* Springer, 2005.

[1.15] J. B. Abshire et al., "Pulsed airborne lidar measurements of atmospheric CO2 column absorption," Tellus B 52, 770 (2010).

[1.16] M. N. Petrovich et al., "Demonstration of amplified data transmission at 2 μm in a low-loss wide bandwidth hollow core photonic bandgap fiber," Opt. Express 21, 28559-28569 (2013).

[1.17] Z. Li et al., "Thulium-doped fiber amplifier for optical communications at 2 μm," Opt. Express 21, 9289-9297 (2013).

[1.18] N. Simakov et al., "High gain holmium-doped fibre amplifiers," Opt. Express 24, 13946-13956 (2016).

[1.19] A. D. Ellis et al., "Communication networks beyond the capacity crunch," Phil. Trans. R. Soc. A 374, 2015019 (2016).

[1.20] S. D. Agger et al., "Emission and absorption cross section of thulium doped silica fibers," Opt. Express 14, 50-57 (2006).

[1.21] N. Simakov et al., "A cladding-pumped, tunable holmium doped fiber laser," Opt. Express 21, 28415-28422 (2013).

[1.22] R. G. Smart et al., "Continuous-wave oscillation of Tm3+-doped fluorozirconate fibre lasers at around 1.47 μm, 1.9 μm and 2.3 μm when pumped at 790 nm," Opt. Commun. 82, 563–570 (1991).

[1.23] J. N. Carter et al., "Thulium-doped fluorozirconate fibre laser," J. Non-Cryst. Solids 140, 10–15 (1992).

[1.24] S. Xing et al., "Generation of high-brightness spectrally flat supercontinuum in 1900-2450 nm range inside a small core thulium-doped fiber amplifier," in Lasers Congress 2016, paper AM5A.8.

[1.25] S. D. Jackson, "Towards high-power mid-infrared emission from a fibre laser," Nat. Photonics 6(7), 423–431 (2012).

[1.26] S. Tokita et al., "Stable 10 W Er:ZBLAN fiber laser operating at 2.71–2.88μm," Opt. Lett. 35, 3943-3945 (2010).

[1.27] S. Duval et al., "Femtosecond fiber lasers reach the mid-infrared," Optica 2, 623-626 (2015).

[1.28] O. Henderson-Sapir et al., "Versatile and widely tunable mid-infrared erbium doped ZBLAN fiber laser," Opt. Lett. 41, 1676-1679 (2016).

[1.29] K. L. Vodopyanov, "Mid-infrared optical parametric generator with extra-wide (3–19-μm) tunability: applications for spectroscopy of two-dimensional electrons in quantum wells," J. Opt. Soc. Am. B 16, 1579-1586 (1999).

[1.30] R. W. Boyd. *Nonlinear Optics (3rd ed.)*. Academic Press, 2008.

[1.31] M. W. Haakestad et al., "Mid-infrared optical parametric oscillator synchronously pumped by an erbium-doped fiber laser," Opt. Express 18, 25379-25388 (2010).

[1.32] A. Grisard et al., "Quasi-phase-matched gallium arsenide for versatile mid-infrared frequency conversion," Opt. Mater. Express 2, 1020-1025 (2012).

[1.33] G. Mennerat et al., "High-energy narrow-linewidth tunable source in the mid infrared," in *Advanced Solid State Lasers*, W. Bosenberg and M. Fejer, eds., Vol. 19 of OSA Trends in Optics and Photonics Series (Optical Society of America, 1998), paper FC13.

[1.34] A. Joullié et al., "GaSb-based mid-infrared 2–5 μm laser diodes," C. R. Physique 4 (2003).

[1.35] W. Zeller et al., "DFB Lasers Between 760 nm and 16 μm for Sensing Applications," Sensors 10, 2492–2510 (2010).

[1.36] D.Z. Garbuzov et al., "2.3–2.7 μm room temperature CWoperation of InGaAsSb– AlGaAsSb broad waveguide SCH-QW diode lasers," IEEE Photon. Technol. Lett. 11, 794–796 (1999).

[1.37] J. Faist et al., "Quantum Cascade Laser," Science 264, 553 (1994).

[1.38] Y. Yao et al., "Mid-infrared quantum cascade lasers," Nat. Photonics 6(7), 432–439 (2012).

[1.39] R. Q. Yang, "Mid-infrared interband cascade lasers based on type-II heterostructures" Microelectron. J. 30, 1043 (1999).

[1.40] L. Nähle et al., "Mid Infrared Interband Cascade Lasers for Sensing Applications," Appl. Phys. B-Lasers Opt. 100, 275–278 (2010).

[1.41] W. W. Bewley et al., "Continuous-wave interband cascade lasers operating above room temperature at λ = 4.7-5.6 μm," Opt. Express 20, 3235-3240 (2012).

[1.42] J. Chiles et al., "Mid-infrared integrated waveguide modulators based on silicon-on-lithium-niobate photonics," Optica 1, 350-355 (2014).

[1.43] https://goochandhousego.com/product-categories/acousto-optic-modulator/ (consulted in November 2016).

[1.44] J. M. Chavez Boggio et al., "Tunable Parametric All-Fiber Short-Wavelength IR Transmitter," J. Lightw. Technol. 28, 443 (2010).

[1.45] B. P.-P. Kuo et al., "Continuous-wave, short-wavelength infrared mixer using dispersion-stabilized highly-nonlinear fiber," Opt. Express 20, 18422-18431 (2012).

Chapter 2 Basics of light propagation in fibers

Light guiding in optical fibers is reviewed in the section, with emphasis on linear and nonlinear effects taking place during propagation and relevant in the scope of third-order parametric amplification. We first present some governing equations of light confinement in fibers, as well as the design of common models, before introducing nonlinearities and their treatment thanks to the nonlinear Schrödinger equation. Afterward the simple gain formula for degenerate four-wave mixing is derived from the coupled wave model. A special section is then dedicated to stimulated Brillouin scattering in optical fibers - as it plays a major detrimental role in FOPAs – and to the ways of quenching it. Finally, a brief introduction to light amplification in rare-earth doped fibers is presented, in view of presenting the TDFA stage used in our experimental setups.

2.1. Light guiding and introduction to Kerr effect

In the basic picture, light guiding in optical fibers originates from the total internal reflection at the interface between a higher index dielectric core and a lower index dielectric cladding, an effect known for more than a century [2.1]. This schematic picture is relatively accurate for step index fibers, but reaches its limits when photonic crystal fibers are concerned [2.2]. In fact, propagation is better described by an electromagnetic radiation propagating over a set of modes, similarly to a Gaussian beam in free space. Nonetheless higher-order modes are of little interest in the scope of FOPAs, as they introduce complexity in the calculation of phase-matching. Coupling light onto these modes is generally regarded as a power waste, and researchers preferentially use single-mode fibers (SMFs) to leverage parametric effects [2.3]. Such fibers exhibit a sufficiently small core and a high enough index difference (as described below) to cut-off all modes but the fundamental one at the wavelengths of concern. Even though intermodal phase matching is a way to enhance fiber-based parametric processes [2.4][2.5], it will be left aside in this dissertation as we use only the fundamental mode of our waveguides.

A silica step-index fiber structure is depicted in Fig. 2.1. The index of the core is raised through doping with germanium or phosphorus oxides whereas the cladding index is depressed with fluorine or boron inclusion. The core radius a and the normalized index difference between the core and the cladding Δn both play a fundamental role to guarantee the single-mode nature of the waveguide, characterized by a V parameter value lower than 2.405. The formulas corresponding to these quantities are the following.

$$\Delta n = \frac{n_{core} - n_{clad}}{n_{core}} \tag{2.1}$$

$$V = \frac{2\pi}{\lambda} a \sqrt{{n_{core}}^2 - {n_{clad}}^2} \tag{2.2}$$

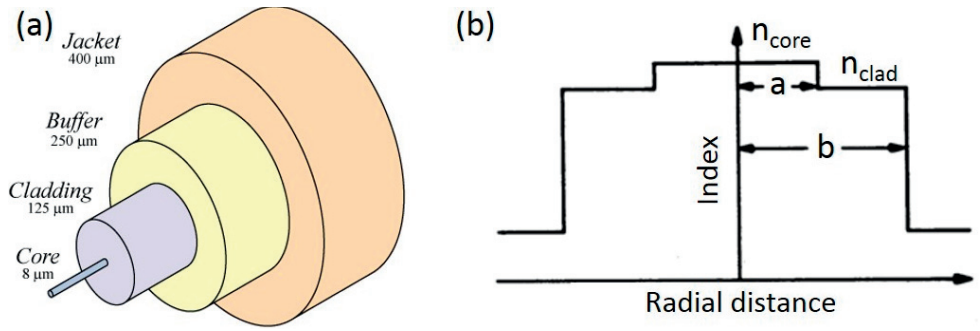

Figure 2.1: (a) Schematic structure of a silica step index SMF, where the buffer and jacket are generally made of polymer and do not contribute to light guiding. (b) Schematic index profile of such a fiber, with *a* the core radius and *b* the cladding radius. Adapted from [2.6].

Where λ is the vacuum wavelength of light and $n_{core/clad}$ the core/cladding bulk material index at the wavelength of interest ($n \approx 1.44$ for undoped silica at 1.55 µm). Therefore if a step-index fiber is single-mode at a given wavelength, it remains single-mode for longer wavelengths given the slight relative index variations. A linearly polarized, quasi-monochromatic electromagnetic wave propagating on the fundamental mode, along the optical axis z, can then be described by Eq. 2.3, where c. c. designates the complex conjugate.

$$\boldsymbol{E}(r, \Phi, z, t) = [A(z,t)F(r,\Phi)e^{-i(\omega_0 t - \beta(\omega_0)z)} + \text{c. c.}]\boldsymbol{u_r} \tag{2.3}$$

$A(z,t)$ is the complex field envelope, varying slowly in time with respect to the carrier frequency ${\omega_0}/{2\pi}$, and in space with respect to the vacuum wavelength λ_0. $F(r,\Phi)$ is the normalized transverse mode distribution in radial coordinates, $\beta(\omega_0) = n_{eff}(\omega_0)\frac{\omega_0}{c}$ the propagation constant (with n_{eff} the mode effective index) and $\boldsymbol{u_r}$ a unitary vector perpendicular to the optical axis. The transverse mode distribution has to be a solution of the Helmholtz equation in radial coordinates, due to the cylindrical symmetry of fibers. As such, it can be written $F(r,\Phi) = A_{m,n}(r)\cos(n\Phi)$, where m and n are integer. The fundamental mode profile does not depend on Φ, which translates to $n = 0$. It is therefore called the LP_{01} mode, and its distribution is well approximated by a Gaussian function of the radial coordinate. On the other hand, the evolution of the field envelope along the fiber, which is the quantity of interest in this dissertation, is described by the nonlinear Schrödinger equation (NLSE) [2.6].

$$\frac{\partial A}{\partial z} + \beta_1 \frac{\partial A}{\partial t} + \frac{i\beta_2}{2}\frac{\partial^2 A}{\partial t^2} + \frac{\alpha}{2}A = i\gamma|A|^2 A \tag{2.4}$$

Several linear and nonlinear effects are taken into account in this model and described independently by the various terms.

2.1.1. Attenuation

The term including α accounts for the attenuation of the wave as it propagates in the fiber. If $P(z)$ is the optical power at some distance z along the fiber, then $P(z) = P(0)e^{-\alpha z}$. This coefficient is therefore often expressed in dB/km and should be as low as possible to favor nonlinear interactions all over the fiber length. In this scope, it is useful to define the fiber effective length $L_{eff} = \frac{1-e^{-\alpha L}}{\alpha}$. This is the length of a fictitious fiber in which the pump power would be uniform, and that would exhibit equivalent nonlinear effects as the original fiber. This quantity represents the fiber portion useful for nonlinear optics. It should be noted that α depends upon the wavelength as both the fiber guiding properties and the material absorption are chromatic. For instance, early silica fibers featured attenuation peaks near 1.2 µm and 1.4 µm due to O-H molecular transitions that have been suppressed thanks to modern fabrication technologies. Moreover, they strongly attenuate light in the SWIR and MIR due to multi-phonon absorption. In practice silica fibers mentioned in this dissertation can be used to transmit light around 2 µm over tens of meters. They exhibit an attenuation in the 0.01 dB/m range at this wavelength, which results in an 89 m effective length for a 100 m fiber. However, fibers become more sensitive to bend losses in SWIR since light confinement decreases with increasing wavelengths. Bend losses correspond to the light leaking out of the core for short bend radii: the lower this radius, the higher the loss.

2.1.2. Dispersion

The coefficients β_1 and β_2 are the first and second derivative of the propagation constant $\beta(\omega) = n_{eff}\frac{\omega}{c}$ with respect to the angular frequency ω. Note that β is associated to a given mode (the fundamental one in our case), and therefore intermode dispersion is not taken into account here. β_1 accounts for the group delay of a wave packet – the time it takes to travel an infinitesimal length – while β_2 accounts for the packet dispersion, so to speak stretching or compression of the envelope in time. The Taylor expansion of dispersion shown in the NLSE is limited to the second order term, but higher order ones can also be included if the curvature of β_2 is significant. Fibers chromatic dispersion, corresponding to β_2 non-null, cannot be avoided as it directly stems from their frequency dependent attenuation mentioned in the previous paragraph, which has material and optical origins. In fact, the effective index of a waveguide

mode n_{eff} is linked to its attenuation α by the Kramers-Kronig relations [2.7]. It must however be noted that Rayleigh scattering is not accounted for in these relations.

$$n_{eff}(\omega) = 1 + \frac{c}{\pi} P \int_0^{+\infty} \frac{\alpha(\Omega)}{\Omega^2 - \omega^2} d\Omega \tag{2.5}$$

Where P denotes the integral Cauchy principal value. Theoretically, measuring the attenuation profile allows to know entirely the dispersion profile of the fiber. However, in practice it is impossible to know exactly α over the whole optical spectrum (from extreme UV to THz waves) and the calculation of β with Eq. 2.5 is therefore inapplicable. Numerical simulations or direct dispersion measurements are used instead, as detailed in chapter 3. In the scope of FOPAs, it is useful to define the normal dispersion regime, corresponding to $\beta_2(\omega) > 0$, and the anomalous dispersion regime ($\beta_2(\omega) < 0$). Generally, an optical fiber exhibits both regimes, depending on the incident light frequency. The wavelength where the dispersion switches from one regime to the other is called the zero-dispersion wavelength (ZDW) and is of special relevance in the field of nonlinear fiber optics. For the most common SMFs, this point is located near 1.3 µm. Another quantity D (generally expressed in ps/nm/km), coming from the field of telecommunication, is often used instead of β_2. The two are linked by Eq. 2.6, while Fig. 2.2 presents the dispersion profile $D(\lambda)$ of a standard SMF-28, as well as those of dispersion shifted fibers.

$$D = -\frac{2\pi c}{\lambda^2} \beta_2 \tag{2.6}$$

D is often mathematically defined as the summation of the dispersion contributions from the material (D_m) and from the waveguide (D_{wg}), i.e. $D = D_m + D_{wg}$. With a proper waveguide design, e.g. by varying the core size, the index profile or the index difference, it is often possible to compensate for a non-appropriate material dispersion. Doing so, the ZDW of specialty fibers can be shifted up to 1.55 µm in order to bolster nonlinear processes, as described in the next chapter.

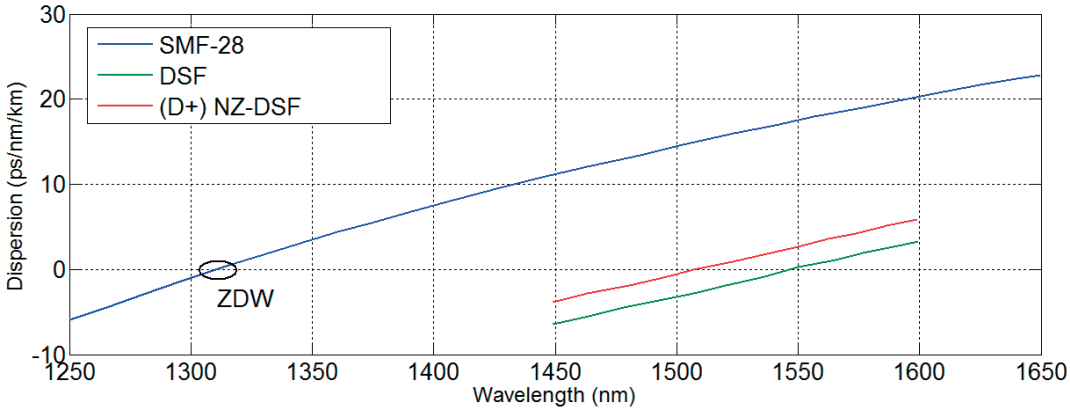

Figure 2.2: Dispersion profile of a standard SMF (SMF-28), of a dispersion-shifted fiber (DSF) featuring a ZDW at 1550 nm, and of a DSF with increased dispersion at 1550 nm ((D+) NZ DSF). Data are from [2.8].

2.1.3. Third-order nonlinearity

The term on the right-hand side in the Eq. 2.4 encapsulates all the instantaneous parametric effects stemming from the third-order susceptibility. The nonlinear coefficient γ is a measure of the fiber nonlinearity and is defined by Eq. 2.7 [2.7]. In this equation A_{eff} is the mode effective area, computed from $F(r,\Phi)$ but well approximated for a Gaussian mode by $A_{eff} = \pi w^2$, w being the mode effective radius. The effective area can vary notably with wavelength, as analyzed in chapter 3, but is in the range of 10 to 50 µm^2 for the fibers used throughout this work. The nonlinear refractive index n_2 is directly linked to the third-order susceptibility tensor of silica $\boldsymbol{\chi}^{(3)}$. The tensor element used to compute n_2 depends on the light polarization, as underlined in Eq. 2.8 for a wave fully polarized along x.

$$\gamma = \frac{n_2(\omega_0)\omega_0}{cA_{eff}(\omega_0)} \tag{2.7}$$

$$n_2(\omega_0) = \frac{3}{8n_{core}} Re(\chi^{(3)}_{xxxx}(\omega_0)) \tag{2.8}$$

Taking all the frequency and polarization dependences of $\boldsymbol{\chi}^{(3)}$ into account is highly complex. Since it features little chromatic dispersion in the infrared [2.9] and given the amorphous nature of silica, we can approximate the tensor by a scalar and constant value. In the core of silica fibers, a common value of $n_2 = 2.7 \cdot 10^{-20}$ m^{2}W^{-1} is often assumed [2.10].

Three main nonlinear processes can be simulated with the NLSE: self-phase modulation (SPM), cross-phase modulation (XPM) and modulation instability (MI), related to FWM. Raman scattering could also be included, as discussed later.

- SPM corresponds to an increase of the refractive index experienced by the propagating wave, which depends on the wave own intensity. The wave therefore modulates its own phase. If a pulsed laser is used, the power variations during the rise and fall time of the pulse translate into a time dependent index variation that leads to a carrier frequency shift, and to the generation of new spectral components [2.11]. The frequency shift can be approximated by Eq. 2.9 and 2.10, where $I(t)$ is the pulse instantaneous intensity, $\omega(t)$ its instantaneous frequency and z the propagation distance. $\omega(t)$ represents the newly generated frequency during the rise time (corresponding to a blueshift) and fall time (redshift) of the pulse, detuned from the original carrier frequency ω_0. A simulation of cascaded frequency shifts from the carrier towards sidebands is shown in Fig. 2.3. In extreme cases, the broadening leads to the generation of a supercontinuum of frequencies [2.12].

$$\Delta n_{core}(t) = n_2 I(t) \tag{2.9}$$

$$\omega(t) = \frac{d}{dt}\left(\omega_0 t - \frac{\omega_0}{c} n(t) z\right) = \omega_0 - \frac{\omega_0}{c} z n_2 \frac{dI}{dt} \tag{2.10}$$

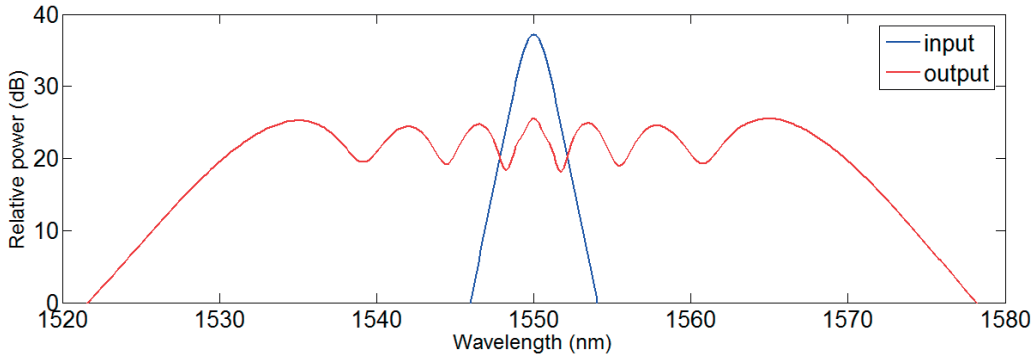

Figure 2.3: Example of the broadening of a 1 ps pulsed shaped as a hyperbolic secant through the propagation in an arbitrary fiber, very close to the ZDW. The threefold frequency shift is clearly visible on each side of the input pulse spectrum. Computed with an NLSE solver base on the Runge-Kutta methods [2.13].

- XPM happens when the phase change of a wave A at a frequency ω_A is caused by another wave B at another frequency ω_B. The index change experienced by A amounts to $2n_2 I_B$. This effect can for instance be used to measure the nonlinear properties of fibers with both a pump and an independent probe wave [2.6].

- MI is slightly more complex because it involves interplay between the fiber nonlinearity and its dispersion. It generally only appears in the anomalous regime, with notable exceptions [2.14]. It corresponds to the temporal break-up of a continuous-wave beam and the appearance of oscillations in its intensity, at a frequency dictated by the fiber dispersion. This effect is also named parametric

fluorescence, and is analogous to FWM in the presence of quantum noise. It will be treated in the next chapter as a way to estimate fiber parameters.

- On top of these effects, Raman scattering corresponds to the delayed and inelastic response of the material [2.6]. Incident photons stimulate the material molecular transitions and consequently generate optical phonons (of high energy and low momentum). In the process the molecule scatters another photon, of which energy is reduced compared to the incident one, by an amount equal to the phonon's energy. By definition, this is not a parametric process and the scattering occurs mostly in the forward direction. Its main signature in silica is a spectral peak of emission, red-shifted from the pump by approximately 13 THz at the fiber output. When occurring in FOPAs, this effect is assumed to decrease the pump power effectively available for parametric pumping by about 18% [2.3]. However, we will neglect its impact on the pump phase and amplitude evolution. It could be taken into account in the NLSE by adding a delayed term on the right hand side, provided that the material Raman impulse response is known.

2.2. Gain equation for degenerate four-wave mixing

In this part we adopt a formalism different from the NLSE, namely the coupled equations model, to derive the simple gain equation describing a single pump FOPA operating in the un-depleted regime, in the absence of loss. Considering the low value of gain we obtain throughout the experiments described in this dissertation, the non-depletion approximation is valid. This approximation means that the power transfer from the pump to the signal and idler has no significant impact on the pump power evolution. Moreover, the pump lasers we use emit in the communication band near 1.55 μm, where the loss of silica fibers is extremely low (<1 dB/km [2.15]). And as the fibers are way shorter than a kilometer, considering them lossless is a fair approximation. These approximations dramatically simplify the equation derivation and its final form. To do so, we assume that all the waves involved in the FWM process are spectrally located close to each other. Once again it simplifies the analysis because the fibers parameters involved can be assumed identical for all waves. Since our FOPAs span a wavelength range from 1.3 μm to more than 2 μm, we will strongly deviate from this case. Tthe quantitative shift caused by a large spectral signal-pump-idler detuning is studied in the next chapter, in the frame of the model we assume here. The present derivation also assumes that the pump is CW or quasi-CW, and the implications of using a short-pulse pump are devised in chapter 5. Quasi-CW means that the pulses are in the nanosecond range or longer, and that SPM-based broadening is negligible.

A simple way to obtain these coupled equations is to assume that the wave described by Eq. 2.3 is in fact composed of three components at three angular frequencies ω_p (pump), ω_s (signal), and ω_i (idler), which

have β_p, β_s, and β_i as propagation constants (respectively). The principle of energy conservation entails that the pump frequency must be the barycenter of the signal and idler in the spectral domain, i.e. $2\omega_p = \omega_s + \omega_i$. By convention the signal is located on the anti-Stokes side (shorter wavelengths) and the idler on the Stokes side (longer wavelengths). Following these definitions, the combined wave envelope can be rewritten in the following form.

$$A(z,t) = A_p + A_s e^{-i[(\omega_s-\omega_p)t-(\beta_s-\beta_p)z]} + A_i e^{-i[(\omega_i-\omega_p)t-(\beta_i-\beta_p)z]} \tag{2.11}$$

Once this is injected in the NLSE, we obtain a set of coupled-equations describing the evolution of each wave, where $\Delta\beta = \beta_s + \beta_i - 2\beta_p$.

$$\begin{aligned}
\frac{dA_p}{dz} &= i\gamma\left(\left(|A_p|^2 + 2|A_i|^2 + 2|A_s|^2\right)A_p + 2A_p^* A_s A_i \exp(-i\Delta\beta z)\right) \\
\frac{dA_s}{dz} &= i\gamma\left(\left(|A_s|^2 + 2|A_i|^2 + 2|A_p|^2\right)A_s + 2A_i^* A_p^2 \exp(-i\Delta\beta z)\right) \\
\frac{dA_i}{dz} &= i\gamma\left(\left(|A_i|^2 + 2|A_p|^2 + 2|A_s|^2\right)A_i + 2A_s^* A_p^2 \exp(-i\Delta\beta z)\right)
\end{aligned} \tag{2.12}$$

The non-depletion assumption implies that the pump is much more powerful than the signal and the idler at every point of the fiber. Therefore its phase or intensity is almost not impacted by the two other waves via the XPM and FWM processes. Since its attenuation is also neglected, we can rewrite the first equation as $\frac{dA_p}{dz} = i\gamma|A_p|^2 A_p$. Only its phase varies, consequently we derive $A_p = \sqrt{P}\exp(i\gamma P z)$ with $P = |A_p|^2$. It is then possible to reinject this value in the signal and idler evolution equations to obtain Eq. 2.13, where it is assumed that XPM between the signal and the idler is once again negligible compared to that driven by the pump.

$$\begin{aligned}
\frac{dA_s}{dz} &= i\gamma\left(2PA_s + A_i^* P\exp(i(\gamma P - \Delta\beta)z)\right) \\
\frac{dA_i}{dz} &= i\gamma\left(2PA_i + A_s^* P\exp(i(\gamma P - \Delta\beta)z)\right)
\end{aligned} \tag{2.13}$$

To solve Eq. 2.13, we proceed to a variable change: $A_s' = A_s e^{i\left(\gamma P - \frac{\Delta\beta}{2}\right)}$ and $A_i' = A_i e^{i\left(\gamma P - \frac{\Delta\beta}{2}\right)}$. This allows us to write Eq. 2.14 and to combine them to a general formula for A_s, where $\kappa = 2\gamma P + \Delta\beta$.

$$\begin{aligned}
\frac{dA_s'}{dz} &= i\frac{\kappa}{2}A_s' + i\gamma P A_i'^* \\
\frac{dA_i'}{dz} &= i\frac{\kappa}{2}A_i' + i\gamma P A_s'^*
\end{aligned} \tag{2.14}$$

$$A_s = (ae^{gz} + be^{-gz})\exp\left(i\left(2\gamma P - \frac{\kappa}{2}\right)z\right)$$
$$g^2 = (\gamma P)^2 - (\frac{\kappa}{2})^2 \tag{2.15}$$

To obtain an actual gain, g must be real, i.e. $|\kappa| < 2\gamma P$. An identical expression is derived for the idler, and since we target frequency down-conversion from the signal to the idler, it implies that $A_s(z=0) = A_{s0}e^{i\varphi_0}$ and $A_i(z=0) = 0$. We therefore find $a = b^* = A_{s0}e^{i\varphi_0}\left(1 + i\frac{\kappa}{2g}\right)$. Finally, we deduce the most interesting quantity for a FOPA, which is the conversion efficiency (CE) after a fiber length L.

$$CE = \frac{|A_i(L)|^2}{|A_s(0)|^2} = \left(\frac{\gamma P}{g}\sinh(gL)\right)^2 \tag{2.16}$$

In the case where both the parametric gain and the loss undergone by the signal are low, it is reasonably accurate to experimentally measure the CE as $\frac{|A_i(L)|^2}{|A_s(L)|^2}$. In any case, this quantity strongly depends on the magnitude of g (assuming it's real), which is maximum when κ is null. For a given pump power and fiber nonlinear coefficient, the efficiency of the process is therefore driven by the linear phase mismatch $\Delta\beta$. However, we mentioned previously that measuring experimentally propagation constant over a spectral range as broad as 1.3 – 2 µm is extremely difficult. Unfortunately, simulations with a mode solver are not reliable neither since the fiber geometry and glass composition are never exactly known. On the contrary, higher-order dispersion terms can be measured locally or continuously over the spectrum, as shown later in this dissertation. It is therefore interesting to find an approximation for $\Delta\beta$ that involves only the derivatives of β and the pump-signal detuning $\Omega = \omega_s - \omega_p = \omega_p - \omega_i$. For this purpose, we express its Taylor expansion at the pump frequency, and inject this expression in the phase mismatch term.

$$\beta(\omega) = \beta(\omega_p) + \sum_{m=1}^{\infty}\frac{\beta_m(\omega_p)}{m!}(\omega - \omega_p)^m \tag{2.17}$$

$$\begin{aligned}\Delta\beta &= 2\beta(\omega_p) + \sum_{m=1}^{\infty}\frac{\beta_m(\omega_p)}{m!}(\Omega^m + (-\Omega)^m) - 2\beta(\omega_p) \\ &= 2\sum_{m=1}^{\infty}\frac{\beta_{2m}(\omega_p)}{(2m)!}\Omega^{2m}\end{aligned} \tag{2.18}$$

In practice, going up to the fourth order dispersion is sufficient, even for broadband FOPAs. Moreover, as the ZDW is often a quantity given by the fiber manufacturer, or because it can be retrieved

experimentally, it is convenient to calculate $\beta_2(\omega_p)$ in the following manner: $\beta_2(\omega_p) \approx \beta_3(\omega_{ZDW})(\omega_p - \omega_{ZDW})$. It assumes that the pump is located close to the ZDW, which is often the case. Using these formulas, the gain profile ($G = 1 + CE$) can be computed in fictitious fibers pumped in the C-band. Some results are plotted in Fig. 2.4 (a) and (b), along with an experimental broadband FWM spectrum.

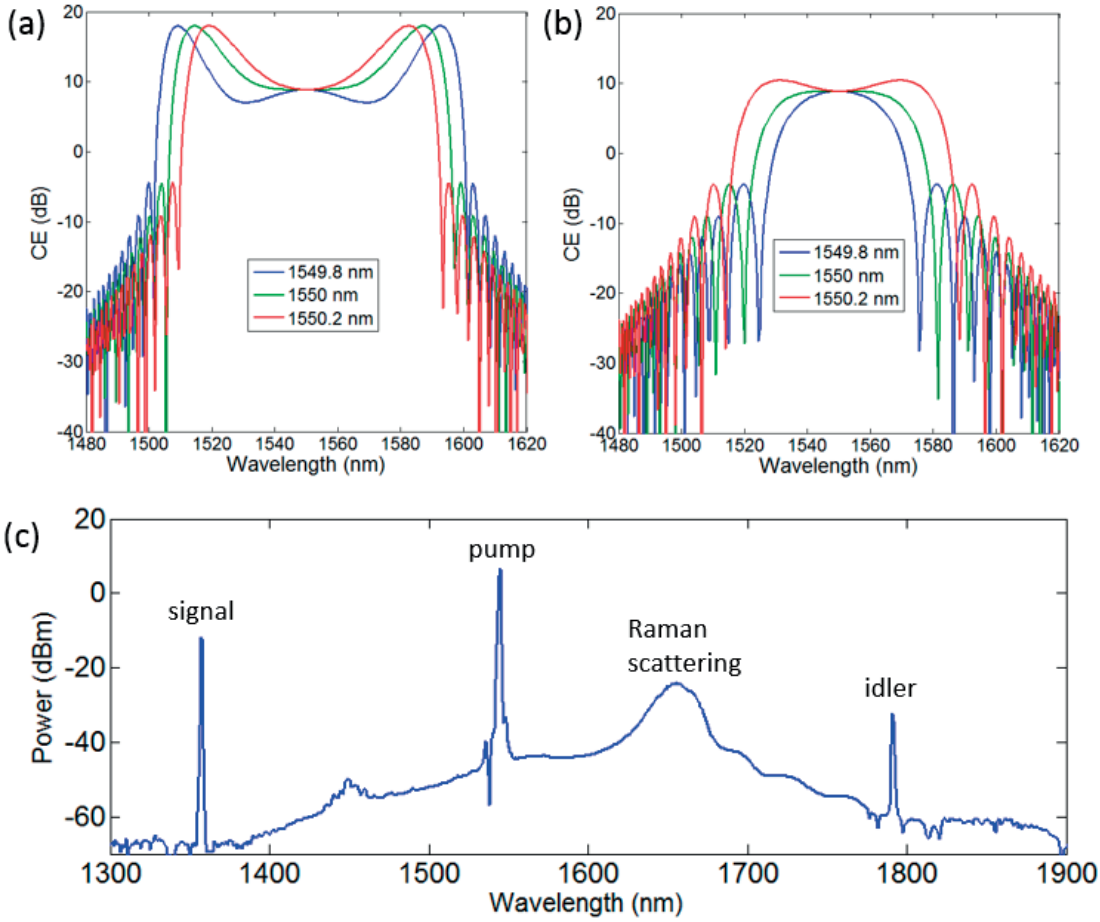

Figure 2.4: (a)-(b) Example of numerical CE spectra for different pump wavelengths, computed for a 200 m long fiber having a nonlinear coefficient of 2 $W^{-1}km^{-1}$ and pumped at 7 W. The dispersion properties are λ_{ZDW}= 1550 nm, β_3 = 1.2 x 10^{-40} s^3m^{-1} and (a) β_4 = -5 x 10^{-55} s^4m^{-1} or (b) 5 x 10^{-55} s^4m^{-1}. The pump wavelength is given in legend. (c) Example of experimental FWM spectrum between a C-band pump and an O-band signal. The 1 W CW pump is located at 1545 nm, while the ZDW is 1551 nm, and γ=11 $W^{-1}km^{-1}$. Some Raman scattering is visible as 1.65 µm, as well as its replication by FWM at 1.45 µm.

FOPAs operating in the telecom band were seen as a promising solution to amplify wavelength-multiplexed optical signals instead of erbium-doped fiber amplifiers (EDFAs) [2.16], since their gain spectrum can be tailored almost at will by changing the fiber type and the pump wavelength. The profile can also be made broad and flat by concatenating various pieces of fibers [2.17]. This appeared highly

advantageous over EDFAs that have a fixed gain region and may suffer from gain competition between channels [2.18], something absent from FOPAs operated in the small signal regime. However, Brillouin scattering represents a major FOPA limitation and crippled these efforts.

2.3. Stimulated Brillouin scattering

Stimulated Brillouin scattering - abbreviated SBS - manifests itself by a distributed reflection of a large fraction of the optical power injected in the fiber. As a result, the effective length is dramatically reduced and all other nonlinear effects are almost entirely quenched. This section reviews some physics at the origin of the phenomenon, from which the Brillouin threshold is derived. Technics to suppress it are also presented.

SBS is comparable to stimulated Raman scattering from a quantum physics point of view: it involves one pump photon and one Stokes photon coupled by one acoustic phonon. Such phonon has a much lower energy than the optical one, therefore the frequency shift is only of the order of 10 GHz in silica fibers at telecommunication wavelengths [2.6]. In a classical description, the pump wave (at frequency ω_p) beats with a counter propagating Stokes wave (at frequency ω_S) to form a forward travelling beat wave. This beat wave modulates the medium refractive index via electrostriction and generates a Bragg grating, forward travelling at an acoustic velocity v_a. This Bragg grating scatters backward a fraction the pump wave, with a frequency downshift $\Omega_B = \omega_p - \omega_S$ due to Doppler effect, which reinforces the Stokes wave. The process is schematized on Fig 2.5. It should be noted that no Stokes wave is seeded at the output of the fiber in FOPAs. Nonetheless the latter grows from noise at a frequency matching exactly the Brillouin shift Ω_B, until the stimulated regime is reached.

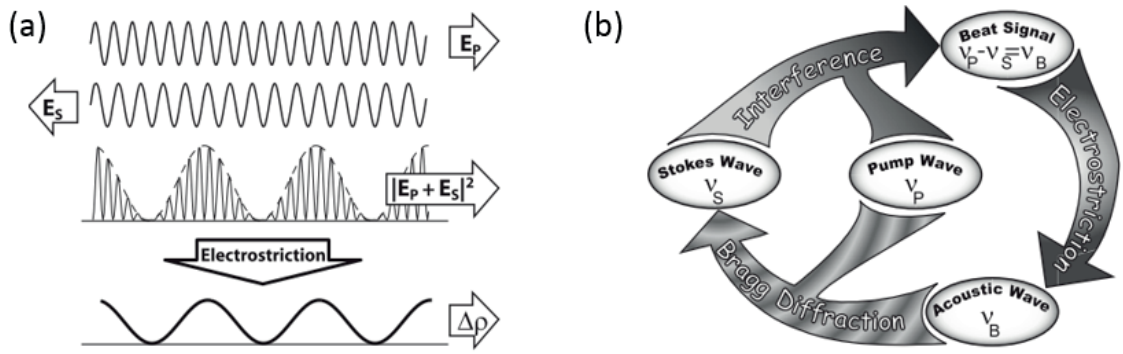

Figure 2.5: Schematic view of SBS with (a) a wave representation of the pump and Stokes beams forming a beat wave and a material density/index modulation through electrostriction. (b) Graph of the interactions between the optical and acoustic waves. Adapted from [2.19].

Some equations describing the main quantities involved in SBS are presented below. In Eq. 2.18, $\boldsymbol{k_a}$, $\boldsymbol{k_p}$ and $\boldsymbol{k_S}$ are the wave vectors of the acoustic, pump and Stokes waves, respectively. The spectral detuning between the last two being as small as 10 GHz, $k_p \approx k_S$ is a fair approximation. Since the waves are counter-propagating, the only allowed case in a fiber [2.6], it entails a simplification of the dispersion relation presented in Eq. 2.20.

$$\boldsymbol{k_a} = \boldsymbol{k_p} - \boldsymbol{k_S} \tag{2.19}$$

$$\Omega_B = v_a|\boldsymbol{k_a}| \approx 2v_a k_p = 2v_a n_{eff}(\omega_p)\frac{\omega_p}{c} \tag{2.20}$$

Assuming standard values for the sound velocity and effective index of silica, a value of 11.5 GHz is found for the detuning at 1.55 µm [2.6]. Hence this relation implies that a monochromatic pump will generate a monochromatic Stokes wave, but the latter is generally broadened due to the mechanical damping of acoustic phonon, taking place over a characteristic time Γ_B. Taking this into account, the Stokes gain spectrum is expressed by the relation below, where Ω is the Stokes detuning from the pump.

$$g_B(\Omega) = g_0 \frac{1}{1 + 4\left(\frac{\Omega - \Omega_B}{\Gamma_B}\right)^2} \tag{2.21}$$

The maximum SBS gain g_0 can be as high as 5 x 10^{-11} m/W. It is also useful to define the Brillouin gain bandwidth $\Delta\nu_B = {}^{2\pi}/_{\Gamma_B}$, of the order of several tens of MHz in optical fibers at room temperature. Following some mathematical developments, it is possible to express the threshold pump power, from which Brillouin scattering starts rejecting any additional power fed into the fiber [2.20].

$$P_{th} = \frac{21A_{eff}}{g_0 L_{eff}} \cdot \frac{\Delta\nu_B + \Delta\nu_P}{\Delta\nu_B} \tag{2.21}$$

Where $\Delta\nu_P$ is the pump laser linewidth. The power needed to reach the stimulated regime can be as low as a few milliwatt in kilometer long fibers seeded by a monochromatic laser [Fishman]. In the field of FOPAs, the fibers are shorter but the pump power is much higher, leading to its total rejection if no care is taken. With this in mind, one way to raise the threshold is to increase A_{eff} or decrease L_{eff}, but both are detrimental to the efficiency of parametric amplification.

The most widespread method is to use a pump of which linewidth far exceeds the SBS gain bandwidth, for instance a pulsed pump. This means that the transient optical illumination is too fast compared to the response time of the Bragg grating formation in the material. In theory pulses with a bandwidth of the GHz order should completely cancel SBS. However, if the repetition rate is high and if the pulses are mutually coherent, the acoustic wave can build-up from adjacent pulses [2.21]. Given the high peak powers at play in parametric amplifiers (1 W – 1 kW), it is necessary to use pulses significantly broader than 1 GHz if the repetition period is of the order of Γ_B~1 ns. For instance, in the FOPA described in chapter 5, using coherent pulses that are 40 ps long totally circumvented SBS, even at multi-GHz rate. Nonetheless working in pulsed regime is not necessarily an option, and shortening the pulse duration favors SPM and supercontinuum generation over FWM. In most configurations, having a CW or quasi-CW pump is necessary. Telecom-grade diode lasers are often used, and their very low linewidth (<100 KHz) entails a strong SBS. One option is to decrease their coherence time, i.e. artificially broaden their spectrum, by applying a phase dithering through a phase modulator. The driving radio-frequency (RF) signal can be a random digital sequence [2.22]. The best quenching occurs for a uniform pump spectral density [2.23]. However, in the case of degenerate FWM, this pump broadening necessarily decreases the coherence time of the generated idler. This can to be a problem if a narrow idler linewidth is targeted, for instance for spectroscopy. Using a two-pump OPA with a phase-conjugated dithering of each pump can theoretically solve the problem [2.24], but the complexity of two-pump OPAs renders their implementation impractical for broadband conversion.

Static options that consist in modifying the fiber are an alternative of interest since they do not lead to idler broadening. It is possible to dope the fiber core with aluminum oxide instead of germanium oxide, in order to reduce the acoustic wave guiding, but it reduces the nonlinear coefficient as well [2.25]. Other technics randomly modify the fiber parameters over its length in order to scramble the Brillouin shift Ω_B. A change in the fiber temperature or strain induces a change in the Brillouin shift, a property leveraged in fiber sensors [2.26]. Unfortunately, this also induces local dispersion changes, very detrimental to broadband phase matching. Nonetheless a fiber design was recently proposed, which renders the fiber

dispersion insensitive to longitudinal stress, allowing for efficient FWM in a piecewise strained fiber [2.27].

Finally, we have considered phase-dithering and piecewise fiber straining to suppress SBS in our FOPAs in CW or quasi-CW regime. However, stretching tests performed on an arbitrary 100 m long HNLF demonstrated the complexity and modest benefit of the method, which leads to a threshold increase of a few dB only. A common SBS characterization consists in measuring the reflected power (P_{SBS}) as a function of the input power (P_{in}) (here with a 1550 nm laser). Then a parameter μ is set to define the SBS threshold, which corresponds to the input power for which $P_{SBS} = \mu P_{in}$ [2.28]. Some fiber stretching results are presented on Fig. 2.6(a) and (b), they show only a 1.3 dB increase in the threshold, for $\mu = 0.01$. Fig. 2.6(c) shows the strain profile applied to the fiber. On the contrary, pump phase dithering allows the injection of a multi-Watt CW pump into the fiber with a reflected power smaller than a milliwatt, as seen in chapter 4. This is the solution we implemented throughout the project.

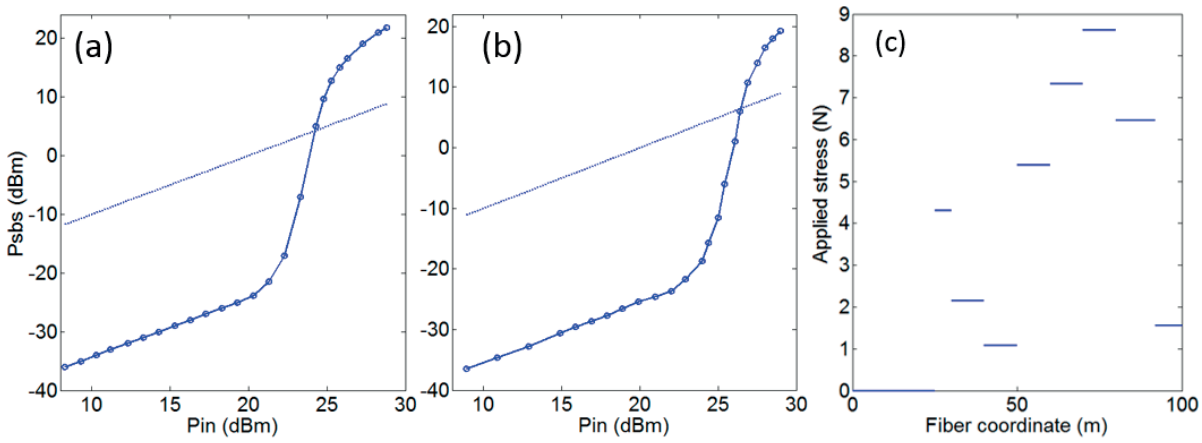

Figure 2.6: Power backscattered by SBS from a 100 m long HNLF when it is un-stretched (a), and piecewise stretched (b), using the stress profile shown in (c). The laser is an amplified 1550 nm telecom diode laser.

As seen in the introduction, fiber amplifiers are realized by doping glass fiber with rare earth ions that have radiative electronic transitions in the infrared. The trivalent ions of ytterbium, erbium, thulium and holmium are the most common dopants. Erbium, of which the discrete energy levels are pictured in Fig. 2.7(a), is the most widespread. Indeed, erbium-doped fiber amplifiers are used to re-amplify telecommunication signals in the C- and L-band, and are therefore included in repeater units every tens of kilometers over long-haul fiber links. These fibers are optically pumped, generally at 980 nm, which corresponds to a transition from the ground state to the $^4I_{11/2}$ level. The ion energy then quickly decays to the $^4I_{13/2}$ level. This decay is non-radiative for high phonon energy hosts like silica, whereas it emits a photon in glasses based on heavy elements [2.29]. The transition $^4I_{13/2}$-$^4I_{15/2}$ then entails emission of a photon at about 1.55 µm.

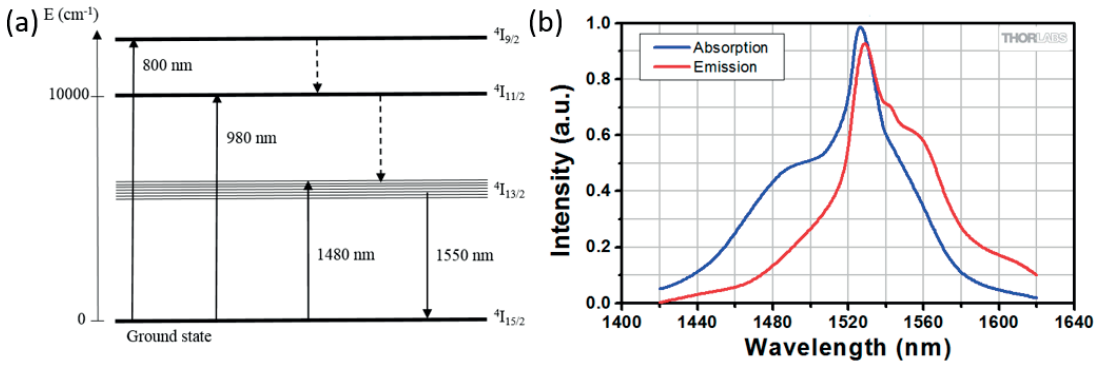

Figure 2.7: (a) Energy levels of Er^{3+} ions in silica, where the $^4I_{13/2}$ manifold is expanded. Solid arrows represent transitions involving a photon, while dashed arrows represent non-radiative de-excitations. Data taken from [2.30]. (b) Normalized emission and absorption cross section of standard erbium-doped silica fibers, from [2.31].

As such, it corresponds to a three-level system where the level $^4I_{13/2}$ has the longest lifetime, of the order of 10 ms [2.32]. However, it is also possible to pump the fiber around 1.48 µm, exciting ions from the ground state to the upper part of the $^4I_{13/2}$ manifold. This scheme is called in-band pumping, and is permitted by the Stark broadening of the ion energy levels in a solid-state host. After photon absorption, the energy states are quickly distributed over the lower manifold levels via the thermalization (on the ps time scale at room temperature). The 1.48 µm pump is therefore too energetic to stimulate emission, contrarily to an eventual longer wavelength signal (for instance at 1.55 µm). A seemingly two-level system can therefore achieve signal light amplification, and is called quasi three-level system. The absorption and emission cross sections for this system vary slightly in terms of amplitude and spectral distribution, and are shown in Fig. 2.7(b). Since they strongly overlap, the fiber amplifier gain profile strongly depends on the fiber length, its doping concentration, and the pump power. In this dissertation, we are mainly interested by thulium-doped fiber amplifiers. And since TDFAs pumped near 1.55 µm also follow such quasi three-level system [2.33], chapter 4 details how critical a proper adjustment of these parameters is to obtain the desired amplification.

A detrimental consequence of the thermalization process and of the resulting ion energy distribution is the presence of amplified spontaneous emission (ASE) at the fiber output. Even in the presence of an input signal, ions in energy states that do not match the signal wavelength will emit spontaneous photons. These photons have a random wave vector, but some of them are guided in the fiber and cause stimulated de-excitations further on their path. This process results in a broad fluorescence spectrum at the fiber output. This emission has noise properties and degrades the amplifier performances [2.34]. But more importantly, it can cause parasitic lasing in case of unwanted feedback in the optical setup, as seen in chapter 4. This represents a further source of noise and of gain limitation [2.35].

2.4. References

[2.1] J. Hecht, *City of Light*. Oxford University Press, New York, 1999.

[2.2] P. St.J. Russell, "Photonic-Crystal Fibers," J. Lightwave Technol. 24, 4729-4749 (2006).

[2.3] M. E. Marhic, *Fiber optical parametric amplifiers, oscillators and related devices*. Cambridge University Press, 2008.

[2.4] F. G. Omenetto et al., "Simultaneous generation of spectrally distinct third harmonics in a photonic crystal fiber," Opt. Lett. 26, 1158-1160 (2001).

[2.5] Y. Xiao et al., "Theory of intermodal four-wave mixing with random linear mode coupling in few-mode fibers," Opt. Express 22, 32039-32059 (2014).

[2.6] G. P. Agrawal, *Nonlinear Fiber Optics, 3rd edition*. Academic Press, 2001.

[2.7] D. C. Hutchings et al., "Kramers–Kronig relations in nonlinear optics," Opt. Quantum Electron. 24, 1 (1992).

[2.8] D. R. Goff, *Fiber Optic Video Transmission, 1st ed.* Focal Press: Woburn, Massachusetts, 2003.

[2.9] I. P. Nikolakakos et al., "Broadband characterization of the nonlinear optical properties of common reference materials," IEEE J. Sel. Top. Quantum Electron. 10, 1164–1170 (2004).

[2.10] M. Hirano et al., "Silica-based highly nonlinear fibers and their application," IEEE J. Sel. Top. Quantum Electron. 15, 103–113 (2009).

[2.11] R. H. Stolen et al., "Self-phase-modulation in silica optical fibers," Phys. Rev. A 17, 1448–1453 (1978).

[2.12] F. Parmigiani et al., "Ultra-flat SPM-broadened spectra in a highly nonlinear fiber using parabolic pulses formed in a fiber Bragg grating," Opt. Express 14, 7617-7622 (2006)

[2.13] J. M. Dudley et al., "Supercontinuum generation in photonic crystal fiber," Rev. Mod. Phys. 78, 1135–1184 (2006).

scgbook.info (consulted in July 2016).

[2.14] J.D. Harvey et al., "Scalar modulation instability in the normal dispersion regime by use of a photonic crystal fiber," Opt. Lett. 28, 2225–2227 (2003).

[2.15] http://fiber-optic-catalog.ofsoptics.com/item/optical--fibers/highly-nonlinear-fiber-optical-fibers1/hnlf-standard-highly-non-linear-fiber-modules (consulted in July 2016).

[2.16] M. Jamshidifar et al., "Continuous-wave parametric amplification in bismuth-oxide fibers," Opt. Fiber Technol. 16, 458–466 (2010).

[2.17] M. E. Marhic et al., "Broadband fiber-optical parametric amplifiers and wavelength converters with low-ripple Chebyshev gain spectra," Opt. Lett. 21, 1354-1356 (1996)

[2.18] M. Furdek et al., "Gain competition in optical amplifiers: A case study," *MIPRO, 2010 Proceedings of the 33rd International Convention*, Opatija, Croatia, 467-472 (2010).

[2.19] D. Alasia. *Advanced trends in nonlinear optics applied to distributed optical-fibre sensors*. PhD dissertation, EPFL (2006). doi:10.5075/epfl-thesis-3648

[2.20] D. A. Fishman et al., "Degradations due to stimulated Brillouin scattering in multigigabit intensity-modulated fiber-optic systems," J. Lightwave Technol. 11(11), 1721–1728 (1993).

[2.21] H. Li et al., "Dynamic behavior of stimulated Brillouin scattering in a single-mode optical fiber," Jpn. J. Appl. Phys. Part 1, 38, 6309–6315 (1999).

[2.22] D. Cotter, "Suppression of stimulated Brillouin scattering during transmission of high-power narrowband laser light in monomode fibre," Electron. Lett. 18, 638–640 (1982).

[2.23] J. B. Coles et al., "Bandwidth-efficient phase modulation techniques for Stimulated Brillouin Scattering suppression in fiber optic parametric amplifiers," Opt. Express **18**, 18138-18150 (2010)

[2.24] K. K. Y. Wong et al., "Phase-conjugate pump dithering for high-quality idler generation in a fiber optical parametric amplifier," IEEE Photon. Technol. Lett. 15, 33–35 (2003).

[2.25] L. Grüner-Nielsen *et al*., "Brillouin suppressed highly nonlinear fibers," *2012 38th European Conference and Exhibition on Optical Communications*, Amsterdam, 1-3 (2012).

[2.26] L Thevenaz, "Brillouin distributed time-domain sensing in optical fibers: state of the art and perspectives," Front. Optoelectron. China, 3(1): 13–21 (2010).

[2.27] B. P.-P. Kuo et al., "Continuous-wave, short-wavelength infrared mixer using dispersion-stabilized highly-nonlinear fiber," Opt. Express 20, 18422-18431 (2012).

[2.28] A. Kobyakov et al., "Stimulated Brillouin scattering in optical fibers," Adv. Opt. Photon. **2**, 1-59 (2010).

[2.29] V. Fortin et al, "Towards the development of fiber lasers for the 2 to 4 μm spectral region," Optical Engineering 52, 54202 (2013).

[2.30] A. Ghatak, K. Thyagarajan. *An Introduction to Fiber Optics*, Cambridge University Press, 1998.

[2.31] https://www.thorlabs.com/NewGroupPage9.cfm?ObjectGroup_ID=1504 (consulted in October 2016).

[2.32] R. Wu, et al., "Fluorescence lifetime and 980-nm pump energy transfer dynamics in erbium and ytterbium co-doped phosphate laser glasses," Proc. SPIE 4968, 4968-1 (2003).

[2.33] J. M. O. Daniel et al., "Ultra-short wavelength operation of a thulium fibre laser in the 1660–1750 nm wavelength band," Opt. Express **23**, 18269-18276 (2015)

[2.34] K. Bertilsson et al., "Noise figure of erbium doped fiber amplifiers in the saturated regime," IEEE Photon. Technol. Lett. 6, 199-201, (1994).

[2.35] J. Nilsson et al., "High-power fiber lasers: new developments," proc. SPIE, 4975-11, San Jose (2003).

Chapter 3 Wideband parametric conversion

This chapter is a transition between the basic concepts of light propagation in fibers presented in the previous one and the presentation of experimental results obtained with broadband FOPAs. It extends the theory of chapter 2 to focus on problematics arising when using real-world HNLFs and signal-pump detuning of the order of tens of THz, such as from C-band to SWIR. This configuration results in a significant deviation from the simple model presented before, which assumes achromatic parameters. The first section will describe the waveguide requirements in the broadband case and fiber designs to fulfill them. A model is then presented that takes fiber dispersion fluctuations into account, to introduce numerical results relevant to our experimental configurations. The last section describes several linear and nonlinear optical methods to measure fibers dispersion, which is critical to link our computational design guidelines to benchtop prototype realizations.

3.1. Requirements on fiber geometry and dispersion

We have seen previously that the parametric gain profile obtained from FWM depends strongly on fiber dispersion, and can be approximated thanks to a Taylor expansion of the fiber dispersion around the pump frequency. As mentioned earlier, we can limit the Taylor expansion described by Eq. 2.18 to the fourth-order and express the phase mismatch as follow:

$$\Delta\beta = \beta_2(\omega_p)\Omega^2 + \frac{\beta_4(\omega_p)}{12}\Omega^4 \tag{3.1}$$

Ω designates once again the signal-pump (or pump-idler) angular frequency detuning. In the broadband case, the distant CE peaks position is mostly driven by the fiber dispersion, while SPM plays little role. This is illustrated in the computed CE spectra presented in Fig. 3.1, for which the pump power is swept from 0.5 W to 2 W. Such levels of average power are commensurate with what can be injected into HNLFs, as seen in the next chapter. The presence of parametric conversion peaks far from the pump - the idler is 330 nm (or 34 THz) away on the Stokes side - typically results from an interplay between a positive β_2 and a negative β_4 that requires Ω to be large to obtain $\Delta\beta \approx 0$. Moreover, it results in a very steep zero-crossing for the function $\kappa = 2\gamma P + \Delta\beta$. The SPM term adds only a slight offset, unable to influence significantly the position of the CE peak. It must be noted that this offset could become non-negligible with waveguides nonlinearities several orders of magnitude larger than that of silica highly nonlinear fibers.

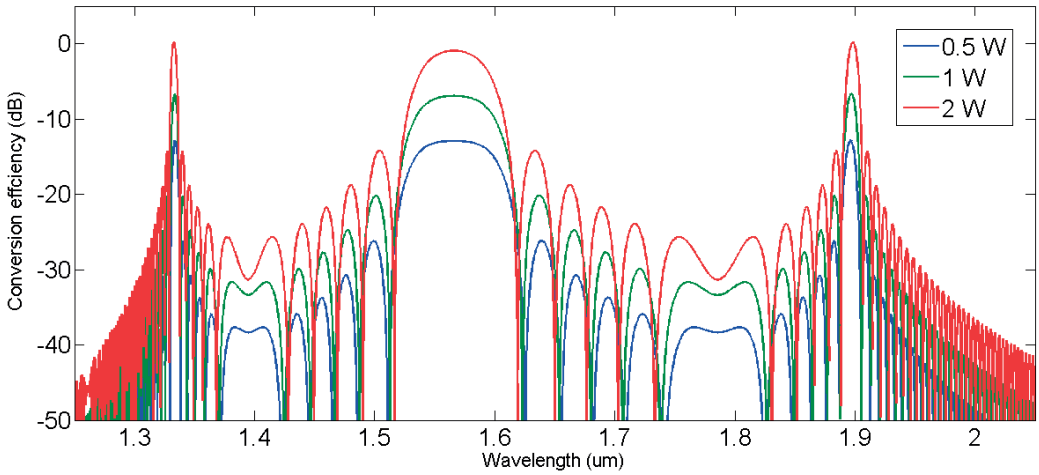

Figure 3.1: Simulated conversion efficiency spectrum in a 30 m long HNLF pumped at 1566 nm and featuring the following properties: $\gamma = 15\ W^{-1}km^{-1}$, ZDW at 1569 nm, $\beta_3 = 4.6 \times 10^{-41}\ s^3m^{-1}$ and $\beta_4 = -2.9 \times 10^{-56}\ s^4m^{-1}$. The pump power is varied from 0.5 W to 2 W and the Stokes peak shifts by less than 1 nm.

It can be observed that the CE lobes shift more with pump power when they are located close to the pump compared to when they are far-detuned. This is once again because the derivative of κ with respect to Ω is smaller for small detunings. Consequently, in the broadband case it becomes possible to plot the CE spectrum as a function of the pump wavelength for a given fiber, independently of the pumping power. This kind of mapping, shown in Fig. 3.2, provides a convenient overview of the possible phase matching schemes to convert light towards SWIR.

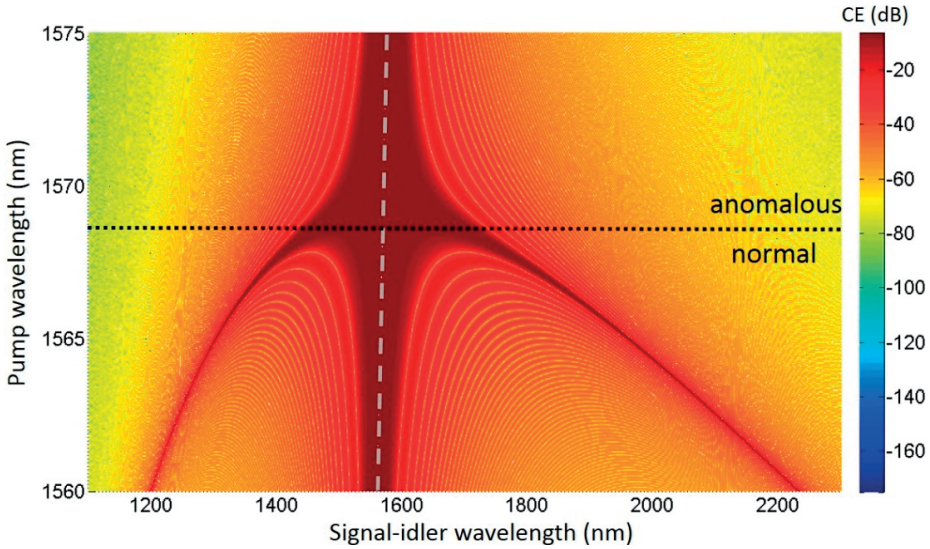

Figure 3.2: Conversion efficiency map when the pump wavelength is swept from the anomalous to the normal dispersion region. The pump wavelength is underlined by the grey dashed line, while the dispersion regime boundary is indicated by the black dotted line. The fiber characteristics are identical to those of Fig. 3.1, and the pump power is 1 W.

This phase matching diagram, clearly showing the shift from the anomalous to the normal regime is typical of a fiber that exhibits a positive β_3 and a negative β_4. According to this theoretical model, the CE peak becomes narrower as the detuning increases, which means that the conversion bandwidth can be limited to a couple of nanometers in the case of broadband FOPAs. However, this model considers a perfectly uniform fiber, something that can never occur in practice. The CE spectrum becomes very sensitive to dispersion fluctuations in the broadband case, it is therefore necessary to take these fluctuations into account, as analyzed in the next section, in order to gain a more realistic insight.

Before going into the modeling of a non-uniform fiber, we will first briefly devise some particular properties of HNLFs. The fictitious fiber considered to plot Fig. 3.1 and 3.2 falls into this fiber category owing to its large nonlinear coefficient ($\gamma = 15\ \mathrm{W^{-1}km^{-1}}$). HNLFs are precisely designed to strengthen the nonlinear coefficient parameter compared to standard single mode fiber (SMF-28) and to match the dispersion requirements of nonlinear optic applications in the telecommunication band, while keeping the attenuation close to that of tSMF-28[3.1]. Such fibers use a preform with an index depression area (obtained through fluorine doping) around a highly germanium oxide-doped core. This geometry yields two benefits. Firstly, the confinement is enhanced by the large index difference between the core and the depressed layer, which allows for a core radius reduction and therefore a small mode effective area. Secondly, the germanium oxide doping increases n_2 in the fiber core [3.2]. The combination of these two effects raises the nonlinear coefficient, from about 1.5 $\mathrm{W^{-1}km^{-1}}$ for standard SMFs [3.3], to one order of magnitude more for HNLFs [3.1]. Additionally, more confinement means less leakage loss and a better robustness to bend loss in the SWIR, as proven recently with HNLFs spooled around 8 mm coils [3.4]. From a dispersion point of view, the fiber structure being more complex, there are more free adjustable parameters to obtain the profile desired for a given application. They generally require a ZDW close to 1.55 µm, or a very low dispersion around this wavelength [3.1]. As mentioned in chapter 2, this is achieved by engineering the waveguide dispersion term D_{wg}, of which analytical formula for step index fibers can be found in [3.5].

It is of interest to study the confinement in such a fiber in a quantitative way. From our project point of view, we would like to compare the fundamental mode, in spectral regions such as the O-band, C-band, and SWIR. We use a finite element solver (COMSOL Multiphysics) to compute the fundamental mode profile at 1300, 1566 and 2000 nm in a fictitious HNLF, with the aim to assess the evolution of the effective area. We have to consider an arbitrary HNLF design since it is generally impossible to know the exact properties of a given commercial fiber in terms of doping profile. We thus use an index profile inspired from [3.1] [3.6], shown on Fig. 3.3(a). A parabolic index raise is assumed in the 4 µm large core. It peaks 3% higher than the cladding index, while the depressed region index is 0.35% lower than that of

the cladding. These doping-related index differences are assumed achromatic, while the reference glass index is computed from Sellmeier equations [3.7]. Shown in Fig. 3(b)-(d) are the mode profiles obtained at the three wavelengths mentioned earlier.

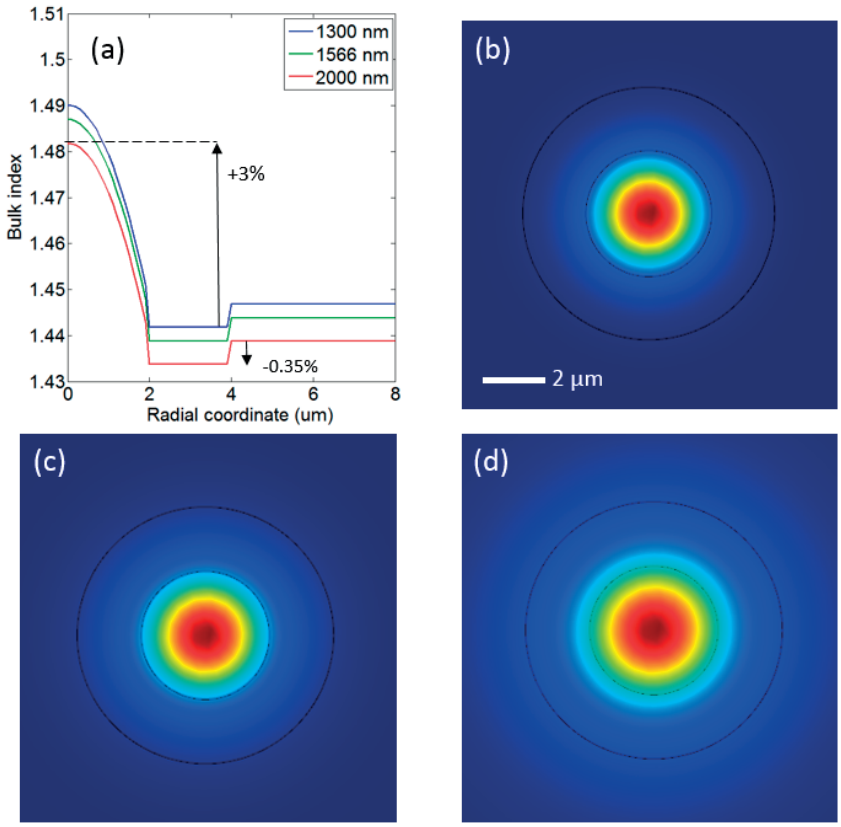

Figure 3.3: (a) Index profile of the fictitious HNLF at 1300, 1566 and 2000 nm. The index for fused silica is computed from Sellmeier equations but the positive and negative deltas are supposed achromatic. (b)-(d) Electric field fundamental mode profile in this HNLF, at 1300, 1566 and 2000 nm, respectively.

The basic model for FWM assumes that all the waves are closely spaced in frequency and have similar effective mode area. Yet the mode spread is visible on Fig. 3.3(b)-(d) as the wavelength increases. The parameter S_{idler} is defined to take the overlap integral between the pump, signal and idler into account [3.8], and to quantify the drop that such a spread entails on the idler growth rate along z. For the idler, the inverse of this parameter is defined by Eq. 3.2. In this equation, the angle brackets denote the integral over the whole cross section, while $F_{i,s,p}$ are the mode distributions of the idler, signal and pump, respectively.

$$\frac{1}{S_{idler}} = \frac{\langle F_i \cdot F_s \cdot {F_p}^2 \rangle}{\sqrt{\langle {F_s}^2 \rangle \langle {F_s}^2 \rangle \langle {F_p}^2 \rangle^2}} \tag{3.2}$$

For the HNLF simulated above, $S_{idler} = 11.2\ \mu m^2$ and should be compared to the pump effective area, namely 10.3 μm^2. As a side remark, this area entails a nonlinear coefficient $\gamma = 10.3\ W^{-1}km^{-1}$ and confirms that the fiber behaves like a HNLF. Besides, the values computed above are close to each other, denoting that the SWIR mode expansion has a limited impact on the idler generation, owing to the large confinement capability of HNLFs. On the other hand, n_2 is rather constant over the spectral range of interest, but γ scales linearly with the frequency. As such it is reduced in the SWIR compared to C-band, even though the mode effective area does not vary significantly. Nonetheless, taking this decrease into account with the coupled equation model is challenging, and we conserve the constant value approximation to study dispersion fluctuations in a simple way, as detailed in the next section. It should still be kept in mind that such an approximation leads to a slight overestimation of the theoretical CE. Besides, the good confinement capabilities of HNLF at 2 µm are beneficial to reduce bend losses in this region.

3.2. Modelling and impact of dispersion fluctuations

As seen in the previous section, phase matching is of primary importance for FWM efficiency. In the broadband case, the scale factor entailed by large Ω in Eq. 3.1 leads to high sensitivity upon the value of dispersion parameters. Any dispersion change undergone by the pump causes a significant shift of the CE peak, and such change takes place along propagation in a non-uniform fiber. Preform fabrication and fiber drawing always lead to doping inhomogeneity or geometrical variations, even though mature technics from the communication industry are used to draw HNLFs [3.1]. Unfortunately, the downside of high doping level and small core designs is a higher sensitivity to variations of these parameters, as illustrated in Fig. 3.4(a). A common and practical way to quantify fluctuations consists in translating them to a ZDW shift. The ZDW of a HNLF can shift by more than 10 nm for a 0.5% change in the core size, whereas a SMF-28 would only undergo a 5 nm change under similar conditions.

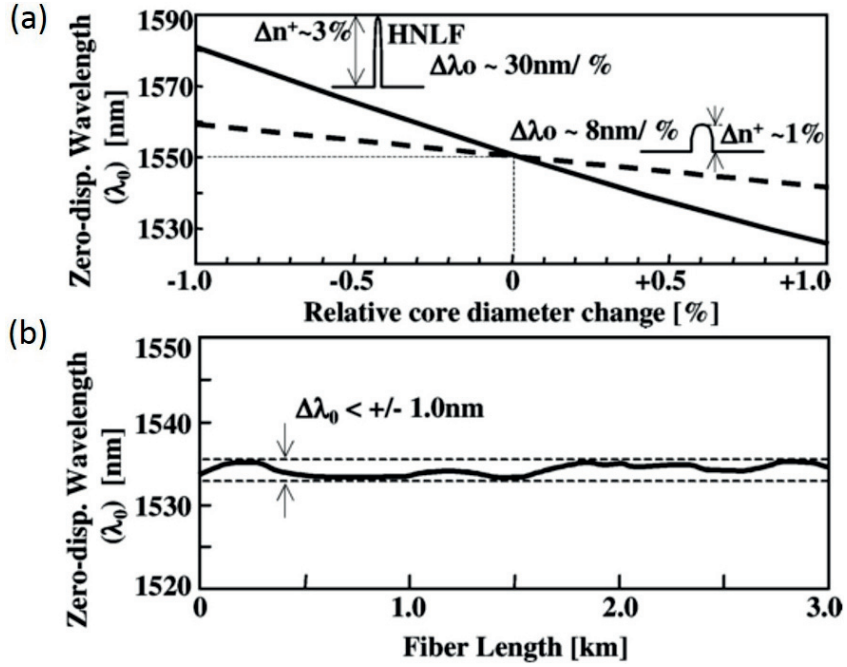

Figure 3.4: ZDW shift as a function of the relative core diameter change for a HNLF (solid line) and for a larger core SMF (dashed line), showing the former's increased sensitivity to drawing imperfections. (b) ZDW mapping of a 3 km long HNLF acquired with a nonlinear optical reflectometry method [3.9]. Adapted from [3.1].

ZDW fluctuations within plus or minus 1 nm are common in HNLFs for it is very hard to reach a core relative uniformity below 0.3%, as illustrated in Fig. 3.4(b). From the typical CE mapping shown in Fig. 3.2, one notices that it corresponds to a tens of nm shift for the CE peak. Even though this seems to be a major hurdle towards the realization of efficient broadband FOPAs, we will present in chapter 4 how these shifts can be leveraged to design straightforwardly wavelength-tunable converters. Thus a modelling of the effect is of interest, and is mostly based on the work presented in [3.10]. It relies on the derivation of a matrix relation for FWM, given by Eq. 3.3.

$$\frac{d\boldsymbol{A}}{dz} = \begin{bmatrix} i\frac{\kappa}{2} & i\gamma P_p \\ -i\gamma P_p & -i\frac{\kappa}{2} \end{bmatrix} \boldsymbol{A} \tag{3.3}$$

In this equation $\boldsymbol{A} = \begin{bmatrix} A_s \\ A_i{}^* \end{bmatrix}$, is the vector encapsulating the complex signal (A_s) and idler (A_i) envelope, P_p is the pump power (assumed constant as we lie in the lossless case), while κ and γ were defined previously. From this equation, two approaches can be chosen to model the fluctuations: the continuous solving of Eq. 3.3 or its lumped approximation. The continuous model assumes continuous ZDW variations along the fiber and directly solves Eq. 3.3 to calculate the CE at the fiber output. It requires an ordinary differential equation solver, for instance implementing the Runge-Kutta-Fehlberg method, and to

run it for many pump-signal detunings in order to reconstruct a CE spectrum. This is rather heavy in terms of computation time and the lumped model appears more suitable to perform intensive simulations. This model is a piecewise approximation of the fibers, which chops it into multiple segments, each featuring a random length and a random ZDW. It is thus possible to integrate Eq. 3.3 over the k[th] segment of length L_k to compute analytically $\boldsymbol{A}$ at its output, as a function of the same vector input value.

$$\boldsymbol{A_{out}} = \begin{bmatrix} \cos(gL_k) + \frac{i2\kappa}{g}\sinh(gL_k) & \frac{i\gamma P_p}{g}\sinh(gL_k) \\ -\frac{i\gamma P_p}{g}\sinh(gL_k) & \cos(gL_k) - \frac{i2\kappa}{g}\sinh(gL_k) \end{bmatrix} \boldsymbol{A_{in}} \tag{3.4}$$

In this representation, $\Delta\beta$ varies in each segment, and follows a probabilistic law detailed below. Finally, naming $\boldsymbol{M}_k$ the matrix in Eq. 3.4, the value of $\boldsymbol{A}$ at the fiber output is given by Eq. 3.5. The CE for one detuning point is obtained by dividing the idler final power by the signal initial power, after simple analytical calculations.

$$\boldsymbol{A_L} = \prod \boldsymbol{M}_k \, \boldsymbol{A_0} \tag{3.5}$$

Adapting the work from Farahmand et al., we chose to describe the fluctuation of the ZDW in the following way: $\lambda_{0,k} = \lambda_{0,mean} + \sigma n_k$, where $\lambda_{0,k}$ is the ZDW for the k[th] segment, $\lambda_{0,mean}$ is the mean fiber ZDW and σ is the ZDW standard deviation. The random variable n_k follows a normal law centered on 0 and of unitary standard deviation. The shift in ZDW translates into a shift in β_2 via the following relation: $\beta_2(\omega_p) \approx \beta_3 \cdot (\omega_p - \omega_{ZDW})$. Then remains the problematics of defining the segments length. Both the continuous and lumped models include one more parameter, namely the fluctuation correlation length L_c. It is the typical length over which fluctuations occur, and its rigorous definition can be found in [3.11]. Still in the piecewise approximation, each segment length is defined as $L_k = -L_c \cdot \ln(m_k)$, where m_k follows a uniform law over [0, 1]. Since the computation relies on random variables, the result should be averaged over a large number of realizations to obtain a relevant output. We use 100 runs in this work. From empirical tests, larger averaging ensembles do not bring any non-negligible modification to the simulated CE spectra.

Another constraint relates to the correlation length over fiber length ratio ($^{L_c}/_{L}$), which should remain much smaller than one. This is essential to ensure that the segment assembly is a fair approximation of a real fiber, by nature continuous. This also leads to a large number of segments in each fiber occurrence, and renders the notion of mean and standard deviation valid for the ZDW. Fig. 3.5 presents the CE spectra in a given HNLF, in a case where the abovementioned condition is fulfilled, computed with both the continuous and the lumped models. The fiber is 30 m long and its mean parameters are the same as for Fig. 3.1. Fluctuations featuring a 1 m correlation length and a 0.2 nm standard deviation are added on top.

The almost perfect similarity between both spectra indicates that the lumped model is a fair approximation for such a fiber. In terms of computational benefits, obtaining the spectrum with the lumped model took less than a minute, and several hours for the continuous one.

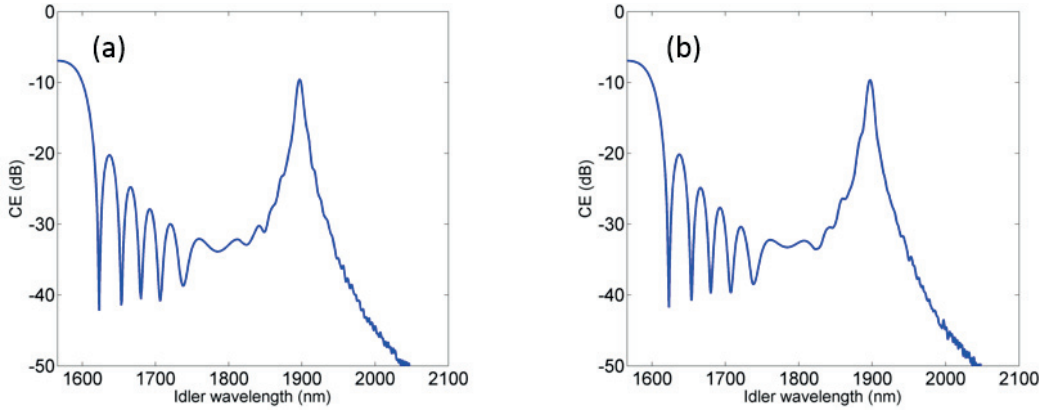

Figure 3.5: Simulated CE spectra (figured only on the Stokes side for symmetry reasons) with (a) the continuous model (solved with a Runge-Kutta-Fehlberg method) and (b) the lumped model.

Another few examples of CE spectra computed with this model are presented on Fig. 3.6, still for the same mean HNLF parameters. Here the ZDW standard deviation is swept from 0 to 0.8 nm to study this parameters's impact, while L_c is fixed at 1 m. A clear spread of the distant CE peak is observed when σ is increased, while its maximum amplitude is reduced by up to 10 dB. The CE for small pump-idler detunings is almost unaffected by fluctuations, as the phase-matching is mostly driven by the pump SPM for a small second-order dispersion.

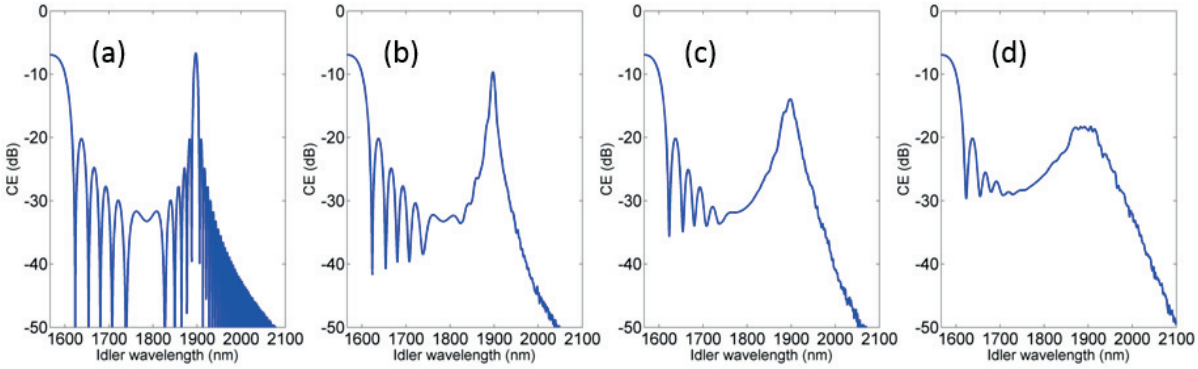

Figure 3.6: Simulated CE spectra when the correlation length is 1 m and the ZDW standard deviation is (a) 0 nm, (b) 0.2 nm, (c) 0.4 nm, and (d) 0.8 nm.

It is also of interest to check the impact of the correlation length with respect to the fiber length, for a fixed ZDW standard deviation. Some results are plotted in Fig. 3.7 and indicate that, for a given L_c, using a longer fiber does not significantly impact the CE bandwidth but raise its value, as for a uniform

waveguide. When the correlation length increases, the bandwidth grows and the peak is reduced, as for the standard deviation.

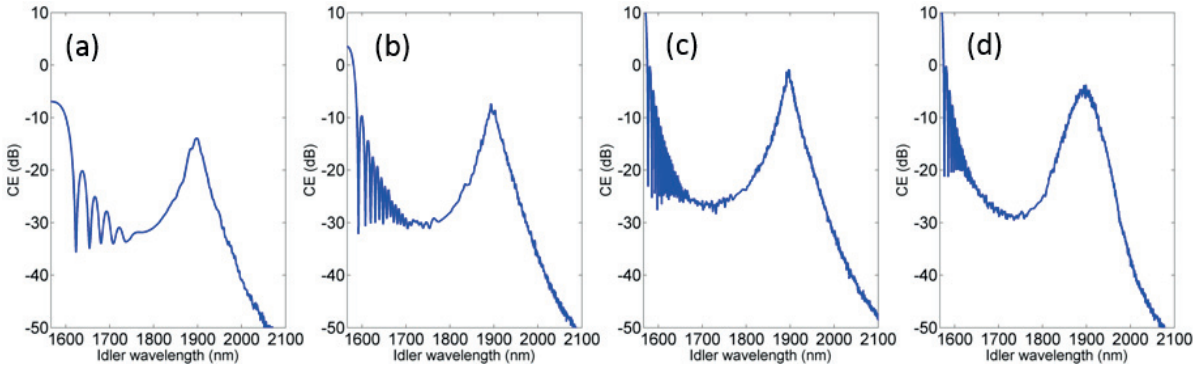

Figure 3.7: Simulated CE spectra with a ZDW standard deviation of 0.4 nm. (a)-(c) The correlation length is 1 m and the fiber length is (a) 30 m, (b) 100 m, and (c) 300 m. (d) The fiber is 300 m long and the correlation length is 5 m.

These results underline how important fiber parameters fluctuations become in wideband FOPAs. Interestingly, if the loss in CE amplitude can be compensated, fluctuations represent a natural way to expand the idler generation spectral range, for a fixed pump wavelength. Since it is impossible to decouple the impact of L_c and σ in the fitting of a given CE spectrum, their independent experimental estimation via FWM is difficult. Nonetheless there exist methods to map the dispersion of a fiber in a spatially resolved way, which are presented in the next section.

3.3. Dispersion measurement methods

Related to our concerns, the first quantities to retrieve in a HNLF are the mean β_2 and β_4 values in the targeted pumping band, i.e. around 1.55 µm in our case. As stated previously the reconstruction of $\beta(\omega)$ thanks to simulation is crippled by uncertainties about the fiber doping and geometry. To overcome this problem, we present three classes of methods to record the mean dispersion parameters: phase shift methods, white-light interferometric measurements and technics based on modulation instability. Moreover, protocols to map the fluctuations are quickly described, as they can provide an order of magnitude for the fluctuation parameters described in the previous section.

3.3.1. Phase-shifting method

This method is described exhaustively in [3.12]. It basically consists in intensity-modulating a coherent tunable laser (linewidth ~100 kHz) with a radio-frequency harmonic signal (at frequency f_m) before sending it into the fiber under test (FUT). The power level should be low enough to avoid any nonlinear optical signal distortion. It is recorded after propagation by a fast photodetector at the FUT output. One

port of a vector network analyzer is then connected to the RF oscillator used to drive the modulator, while the other port is connected to the photodetector. As such, a precise measurement of the phase between both harmonic waves is obtained. In frequency space, the signal dephasing means that the modulation sidebands and the carrier have experienced dissimilar phase velocities. The differential phase accumulated is proportional, in first approximation, to the first order dispersion. This is described by Eq. 3.6.

$$\Delta\Phi = \big(\beta(\omega_{side}) - \beta(\omega_{car})\big)L \approx \beta_1(\omega_{car})2\pi f_m L \tag{3.6}$$

Here $\omega_{side/car}$ is the optical frequency of the sideband/carrier, and L is the FUT length. By sweeping the laser wavelength, it is possible to reconstruct β_1 as a function of the carrier frequency over the range of interest. However, since the network analyzer phase reference is not absolute, this function is known up to constant only. Consequently, it is not possible to integrate it and compute exactly $\Delta\beta$ (assuming that the laser could span the whole 1.3 – 2 µm range), and only its derivation to compute β_2 and β_4 is relevant. Unfortunately, phase measurements for short FUTs featuring a low chromatic dispersion are crippled by a large signal-to-noise ratio and measurement imprecisions. HNLFs are precisely designed to have a ZDW near 1.55 µm, leading to very poor results after derivation. Following inconclusive experimental tests, the method was not retained to find suitable HNLFs for our project, although it can be of interest to characterize other highly dispersive systems [3.13].

3.3.2. White light interferometry

The first versions of this method, using a Mach-Zehnder interferometer, have been devised at the beginning of the fiber optics era [3.14]. It leverages the wavelength-dependent optical path difference in the interferometer arms, which entail fringes in the spectrum of a broadband source. In its modern form, it is convenient to use a high-brightness supercontinuum source as it can cover an extremely broad spectral range, and allow for a relatively fast dispersion evaluation from communication bands to the SWIR [3.15]. The white light source is equally split and sent over the two arms of the interferometer. The FUT (of length L_f) is inserted in one of them, and a tunable optical delay line (ODL, inducing a time delay τ) is placed in the other. A balancing fiber (often a SMF-28, of length L_b) is also inserted in the latter to ensure that the optical path is almost equal on both arms, for instance in case a low-coherence source is used. The light from both arm is then coupled back again, with aligned polarizations, and the resulting interference entails a ripple in the spectrum. The central lobe position (denoted ω_0 or λ_0) and the frequency of this ripple depend on the dispersion orders difference between both arms. The phase difference is given by Eq. 3.7. In this equation, the β_n terms refer to the dispersion orders taken in ω_0, either for the FUT (subscript f) or for the balancing fiber (subscript b).

$$\Delta\Phi(\omega) = \left(\beta_{0_f} L_f - \beta_{0_b} L_b - \tau\omega_0\right) + (\omega - \omega_0)\left(\beta_{1_f} L_f - \beta_{1_b} L_b - \tau\right) + \frac{1}{2}(\omega - \omega_0)^2\left(\beta_{2_f} L_f - \beta_{2_b} L_b\right) + \frac{1}{6}(\omega - \omega_0)^3\left(\beta_{3_f} L_f - \beta_{3_b} L_b\right) + \cdots \quad (3.7)$$

The first term (zero-th order) does not depend on the frequency and can be ignored in the analysis of the interference ripple. The second term (first order) is null for a given position of the ODL, which dictates the value of ω_0. Then only the higher order terms contribute to the ripple. An example of spectral fringes produced by this method is illustrated on Fig. 3.8.

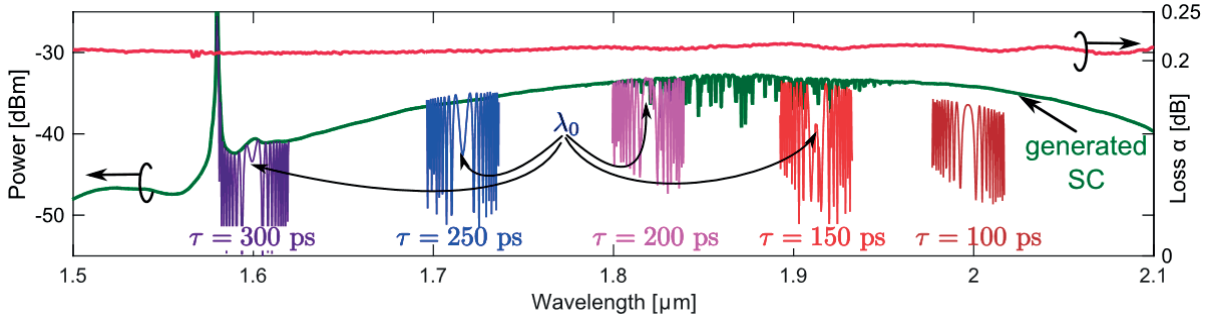

Figure 3.8: Superimposed spectra of the input supercontinuum (green line) and of several interferograms recorded for several positions of the ODL, with a clear shift of λ_0. The FUT is made of fluoride glass, transparent in the SWIR, and its attenuation (dark red curve) is also plotted. Adapted from [3.15].

Via an interferogram fitting for many ODL positions, this method enables the reconstruction of dispersion functions of higher order. Nonetheless this fitting requires the perfect knowledge of the balancing fiber dispersion. In practice, it has been shown that the reconstruction is reasonably accurate up to the third order [3.14]. Uncertainties in the balancing fiber's fourth-order dispersion render irrelevant the evaluation of higher order functions. A way to overcome this limitation is to use an entirely free-space interferometer, but for optical path balancing reasons, the measurement is limited to short FUTs. As far as HNLFs are concerned, this interferometric method provides valuable β_2 and β_3 measurements, but nonlinear measurements are required for evaluating β_4.

3.3.3. Modulation instability fitting

This method was first introduced by Mazzali et al. [3.16], and later refined specifically to characterize HNLFs in both normal and anomalous regime [3.17]. In CW or quasi-CW pumping, if the parametric gain in a waveguide is large enough (i.e. for a CE higher than 0 dB), MI appears. In the spectral domain, it manifests itself by the parametric amplification of quantum noise at frequency detunings for which the phase-matching condition with the pump is fulfilled, and spectral lobes rise around the pump. This is why MI is also called parametric fluorescence in third-order nonlinear waveguides. In the time domain, it corresponds to the breakup of the continuous wave into a modulated one. This modulation frequency is

given by the detuning between the pump and the parametric sidebands [3.18]. The effect is illustrated schematically in Fig. 3.9(a).

We have seen previously that in ideal fibers and for a given pump power, the position of the CE peaks is driven by the dispersion at the pump wavelength. When the pump wavelength is swept, the dispersion is modified and so is the detuning Ω between the pump and the maximum of the MI lobes. Therefore, if the power is known, it is possible to estimate the dispersion parameters from Ω. In order to restrict the number of parameters sought after in the fitting, some assumptions are necessary. We first consider β_4 as constant over the pump sweep range. Secondly, we still evaluate the second-order dispersion at the pump frequency as follow: $\beta_2(\omega_p) \approx \beta_3(\omega_{ZDW})(\omega_p - \omega_{ZDW})$. As such, the fitting parameters are $\beta_3(\omega_{ZDW})$, $\beta_4(\omega_{ZDW})$ and ω_{ZDW}. They are probably the most relevant in the field of FOPAs as they allow for the computation of CE spectra. Moreover, since β_4 is often negative in HNLFs [3.17], assessing its influence on Ω requires to pump in the normal regime, similarly to broadband parametric conversion. Two experimental MI spectra are shown in Fig. 3.9(b), where the detuning is underlined. It illustrates the MI evolution when the pump is swept from the anomalous to the normal dispersion regime. The MI lobe is clearly more distant in the second case. Besides, it is beneficial to consider the anti-Stokes part of the spectrum, as the Stokes lobe can be distorted by Raman scattering in case it is redshifted by 13 THz from the pump, as in the blue curve case. The HNLF used to record these two spectra is described in the next chapter (called HNLF (a) in Table 4.4), and has an average ZDW at 1551 nm. The excitation source is a 1.6 W amplified tunable laser, in CW regime.

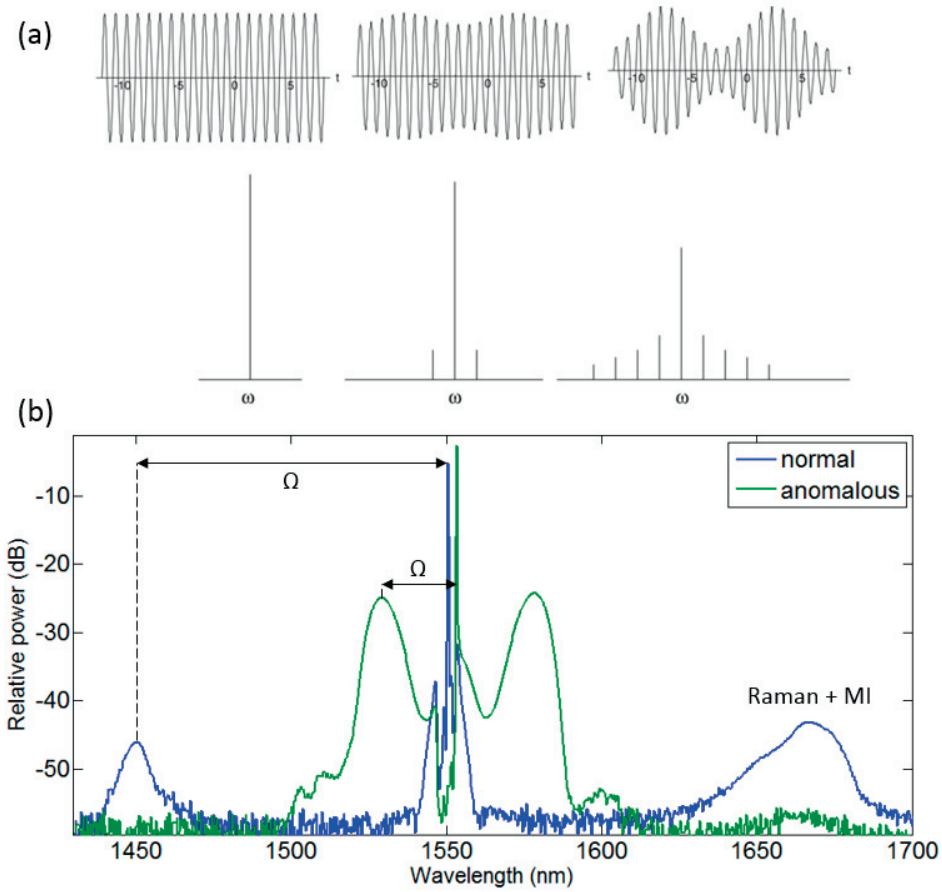

Figure 3.9: (a) Schematic evolution of a wave undergoing MI (top), and corresponding evolution of its spectrum (bottom). Adapted from [3.18]. In nonlinear fiber optics, the sidebands are broadened into spectral lobes, as shown by (b): experimental examples of MI spectra in a HNLF pumped by a CW pump in the anomalous (green curve) and normal (blue curve) dispersion regime. Some Raman fluorescence is visible on the red-side of the spectrum.

A drawback of this method comes from the uncertainty in the actual MI peak frequency. If fluctuations are significant; the lobes are flattened and the estimation of Ω becomes inaccurate. However, contrarily to the interferometric evaluation, this method is calibration-free. It also allows for an estimation of γ, if the latter is included in the fitting parameters. We validated the MI measurement by reproducing results from [3.17] with the same HNLF, and further used the method to characterize the HNLF used in our FOPA. The results are presented in the next chapter.

3.3.4. ZDW spatial mapping

After retrieval of the mean dispersion, it is of interest to map the ZDW as a function of the position z along the fiber, in order to estimate its spread and correlation length. Most local measurements in fiber rely on derivations of optical time-domain reflectometry (OTDR). The OTDR consists in sending a pulse into the FUT and measuring the reflected power as a function of time. In its simplest configuration, a

uniform distributed reflection takes place due to Rayleigh scattering. Thus, the backscattered light a time t is proportional to the pulse power at the coordinate $z(t)$. Its primary use is in measuring attenuation and failures in passive fibers. Similarly, it is possible to measure the local gain in an active fiber, including the parametric gain that depends upon dispersion at point z. Such idea was first introduced by Mollenauer et al. [3.9]. By recording the power backscattered at the idler wavelength in a dual-pump FOPA, they can infer a mapping of the phase-matching condition and extract β_2 at a given wavelength between the pumps. However, the spatial resolution for this early measurement was of the km order, and improvements are necessary to make it relevant for HNLFs.

An efficient way to increase the localization power is to mix the effects of stimulated Brillouin scattering and FWM [3.19] [3.20]. In all these schemes, SBS is used to reinforce the backscattering efficiency. Schematically, an SBS pump is launched at one end of the fiber while the parametric pump and probe are launched at the other end. All waves are pulsed. When the SBS pump overlaps with the parametric one, the latter is amplified (the relative frequencies are set to permit this interaction), to a level sufficient to generate and amplify an idler by mixing with the probe. The idler power is measured and the overlap point is then shifted for a new iteration. By applying an inverse problem solving algorithm, the ZDW map is extracted with a with a meter-scale resolution in a 200 m HNLF. An alternative configuration consists in co-propagating the SBS and parametric pump [3.21]. The former is amplified by the latter and the local process efficiency is probed with a Brillouin OTDR scheme. Our HNLF was probed with this last method, in order to cross-check estimates of the ZDW fluctuations obtained by fitting the CE obtained with it. Results are once again discussed in the next chapter.

3.4. References

[3.1] M. Hirano et al., "Silica-based highly nonlinear fibers and their application," IEEE J. Sel. Top. Quantum Electron. 15, 103–113 (2009).

[3.2] T. Kato et al., "Estimation of nonlinear refractive index in various silica-based glasses for optical fibers," Opt. Lett. 20, 2279-2281 (1995).

[3.3] T. Kato et al., "Measurement of the nonlinear refractive index in optical fiber by the cross-phase-modulation method with depolarized pump light," Opt. Lett. 20, 988-990 (1995).

[3.4] J. M. Chavez Boggio at al., "Short wavelength infrared frequency conversion in ultra-compact fiber device," Opt. Express 18, 439-445 (2010).

[3.5] B. P.-P. Kuo et al., "Highly nonlinear fiber with dispersive characteristic invariant to fabrication fluctuations," Opt. Express 20, 7716-7725 (2012).

[3.6] T. Okuno et al., "Silica-based functional fibers with enhanced nonlinearity and their applications," IEEE J. Sel. Top. Quant. Electron. 5, 1385–1391 (1999).

[3.7] http://refractiveindex.info/?shelf=main&book=SiO2&page=Malitson (consulted in August 2016).

[3.8] G. P. Agrawal, *Nonlinear Fiber Optics, 3rd edition*. Academic Press, 2001. Specifically equations 10.2.2 to 10.2.7.

[3.9] L. F. Mollenauer et al., "Method for facile and accurate measurement of optical fiber dispersion maps," Opt. Lett. 21, 1724-1726 (1996).

[3.10] M. Farahmand et al., "Parametric amplification in presence of dispersion fluctuations," Opt. Express 12, 136-142 (2004).

[3.11] M. Karlsson, "Four-wave mixing in fibers with randomly varying zero-dispersion wavelength," J. Opt. Soc. Am. B 15, 2269-2275 (1998).

[3.12] S. E. Mechels et al., "Accurate Measurements of the Zero-Dispersion Wavelength in Optical Fibers," J. Res. Natl. Inst. Stand. Technol. 102, 333 (1997).

[3.13] T. Niemi et al., "Limitations of phase-shift method in measuring dense group delay ripple of fiber Bragg gratings," IEEE Photon. Technol. Lett. 13(12), 1334–1336 (2001).

[3.14] L. G. Cohen, "Comparison of single-mode fiber dispersion measurement techniques," J. Lightwave Technol. 3, 958–966 (1985).

[3.15] S. Kharitonov et al., "Broadband Characterization of ZBLAN Fiber for Short-Wave Infrared Applications Using All-Fiber Interferometer," in *Conference on Lasers and Electro-Optics*, OSA Technical Digest (2016) (Optical Society of America, 2016), paper SM3P.1.

[3.16] C. Mazzali et al., "Simple method for measuring dispersion and nonlinear coefficient near the zero-dispersion wavelength of optical fibers," IEEE Photonics Technol. Lett. 11, 251-253 (1999).

[3.17] B. Auguié et al., "Ultra low chromatic dispersion measurement of optical fibers with a tunable fiber laser," IEEE Photon. Technol. Lett. 18, 1825-1827 (2006).

[3.18] V. E. Zakharov et al., "Modulation instability: the beginning," Physica D 238(5), 540–548 (2009).

[3.19] E. Myslivets et al., "A new class of high-resolution measurements of arbitrary-dispersion fibers: localization of four-photon mixing process," J. Lightwave Technol. 27(3), 364–375 (2009).

[3.20] E. Myslivets et al., "High resolution measurement of arbitrary-dispersion fibers: dispersion reconstruction techniques," J. Lightwave Technol. 28, 3478–3487 (2010).

[3.21] F. Alishahi et al., "Mapping dispersion fluctuations along optical fibers using brillouin probing and a fast analytic calculation," *CLEO: 2013*, San Jose, CA, 1-2 (2013).

Chapter 4 Rare earth-enhanced parametric conversion

This section introduces the experimental results obtained with wideband FOPAs in the CW case, which corresponds to the simplest configuration. Moreover, details on their enhancement with the addition of a TDFA are also presented. In the first section we present HNLF characterization results obtained with the methods explored at the end of the previous chapter. It then deals with the background physics of thulium-doped fibers from an energy level point of view, with the addition of results related to their optical dispersion and nonlinearity characterization. The second section shows the emission properties of various FOPA-TDFA cascaded architectures, and underlines how it improves the energy efficiency of conventional SWIR transmitters. The last section demonstrates SWIR parametric conversion of higher complexity that embeds an additional holmium-doped stage, in order to further redshift the accessible range of our source.

4.1. HNLF and TDF characterization

4.1.1. HNLF characterization

We stated in the previous chapter that characterization with the phase-shift method were unsuccessful, since the HNLFs commonly used are relatively short (hundreds of meters) and feature a low dispersion in C-band. We therefore describe here results obtained with interferometric and MI-detuning methods, starting with the latter. To obtain parametric conversion from the telecom bands towards SWIR the main criteria are, on the one hand, that the ZDW is located somewhere between the C- and L-band, and on the other hand that the fiber features a negative fourth-order dispersion. We also desire limited ZDW fluctuations as they undermine both the MI-based characterization and the parametric conversion efficiency. Especially, strong fluctuations will prohibit recording clear and unique MI peaks in the normal dispersion regime, from which most of the useful fiber information is extracted. Experimentally, in order to generate the MI lobes, a CW pump is injected into HNLFs at power levels between 31 dBm and 32 dBm (1.26 to 1.6 W), requiring the use of phase dithering to suppress SBS. A phase-modulator, driven by a pseudo-random bit sequence (PRBS) at 7 Gbits/s, is inserted between the tunable, telecom-grade semiconductor laser (featuring a 100 kHz linewidth) and the erbium-doped fiber optical amplifier. The PRBS is 2^{31}-1 bits long. This type of laser and PRBS configuration reduce the back-scattered power down to the milliwatt level and are used throughout all the experiments described in this chapter. We chose to work with a CW laser since it entails a much better knowledge of the actual injected power, contrarily to

pulses, of which peak power estimation after amplification can be problematic. The corresponding setup is sketched in Fig. 4.1(a).

Fig. 4.1(b) and (c) present fittings of the MI detuning obtained in two HNLFs fabricated by Sumitomo Electric Industries, which appear to perform well in terms of dispersion fluctuations compared to the fibers from OFS. The detuning curve fitting is obtained by solving Eq. 4.1. In this equation, Ω is the detuning between the pump and the top of the MI lobes, and is P_p the pump power. The other factors are fitting parameters, of which retrieved values are given by Table 4.1 for both fibers. It should be noted that the fiber length has in theory no influence on this measurement. In practice a tradeoff should be found between the nonlinear interaction length, in order to generate a bright enough MI, and the cumulated dispersion fluctuations.

$$\beta_3 \cdot (\omega_p - \omega_{ZDW})\Omega^2 + \frac{\beta_4}{12}\Omega^4 + 2\gamma P_p = 0 \tag{4.1}$$

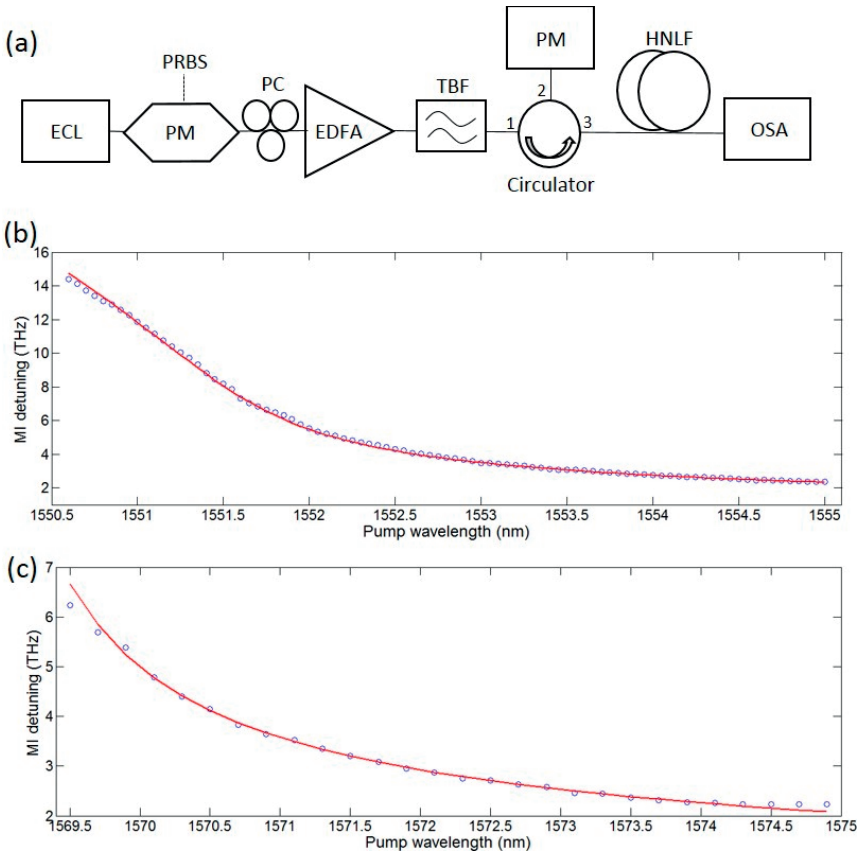

Figure 4.1: (a) Experimental setup for MI generation in a HNLF with ECL: external cavity laser, PM: phase modulator, PC: polarization controller, EDFA: erbium-doped fiber amplifier, TBF: tunable bandpass filter, PM: power meter and OSA: optical spectrum analyzer. (b)-(c) Detuning between the pump laser and the MI peaks in two different HNLFs as a function of the pump wavelength. Upper curve: HNLF (a), lower curve: HNLF (b). The blue circles are experimental data points while the red line represents their optimal fitting with Eq. 4.1.

	HNLF (a)	HNLF (b)
ZDW (nm)	1551.5	1569.05
β_3 (s^3m^{-1})	$6 \cdot 10^{-41}$	$4.6 \cdot 10^{-41}$
β_4 (s^4m^{-1})	$-6.5 \cdot 10^{-56}$	$-2.9 \cdot 10^{-56}$
γ ($W^{-1}km^{-1}$)	11.2	14

Table 4.1: Parameters used in Eq. 4.1 to obtain the experimental data fittings shown in Fig. 4.1(b)-(c).

HNLF (a) had been probed by Auguié et al. previously [4.1], and we retrieved parameters very close to theirs. However, we did not observe any dispersive wave that would have given us additional dispersion information. This stems from the pump CW nature, which prevents it from reaching a sufficient instantaneous power to generate dispersive waves (see chapter 6 for more details about this phenomenon). Both fibers feature a negative fourth order dispersion around the ZDW, which means they should be pumped in the normal regime to permit distant parametric conversion. Given the sign of β_3, it means pumping at a wavelength shorter than the ZDW. Therefore, HNLF (b) appears more suitable to generate long SWIR idlers (e.g. beyond 2 µm) for energy conservation reasons. Keeping in mind that the signal laser has to lie in the O-band given our available lab sources, a longer ZDW implies a longer pumping wavelength, and mechanically a longer-wave idler generation. Assuming a 1250 nm signal, located at the shorter edge of O-band lasers and amplifiers, pumping at 1551 nm enables the generation of a 2043 nm idler at most, while pumping at 1569 nm allows for an idler at 2106 nm.

In terms of fiber characterization, the use of a second method to cross-check the results is highly desirable. For this reason, we measured the dispersion of HNLF (b) with the interferometric technic, which allowed for the reconstruction of the second-order dispersion on a very large span, from 1450 nm to 2050 nm. These dispersion curves, coming from two runs of the same experiment, are shown in Fig. 4.2. Every data points corresponds to a given value of the optical delay line, placing the central fringe at the corresponding wavelength. We wish to extract the ZDW from this curve, as well as the third and fourth-order dispersion at the ZDW. For this purpose, the experimental curve is fitted with a quadratic polynomial, of which derivatives are computed near the ZDW. The fitting span can be restricted around the ZDW (e.g from 1.45 to 1.7 µm), in order to neglect the inflexion of β_2 on the experimental domain boundaries. Empirically, this approximation is required to be consistent with the MI measurements.

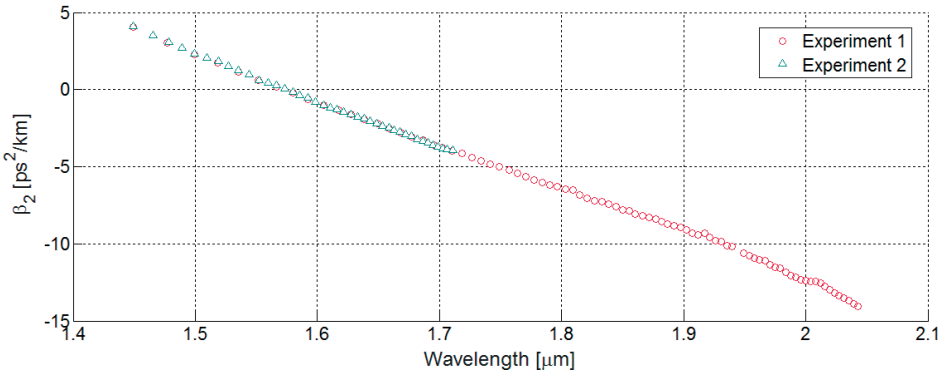

Figure 4.2: Second order dispersion curve for HNLF (b), measured with the interferometric method. This experiment has been performed twice, and the experimental data from each run are pictured with green triangles or red circles.

	Experiment 1	Experiment 2
ZDW (nm)	1572	1574
β_3 (s^3m^{-1})	$4.03 \cdot 10^{-41}$	$4.07 \cdot 10^{-41}$
β_4 (s^4m^{-1})	$-2.1 \cdot 10^{-56}$	$-1.4 \cdot 10^{-56}$

Table 4.2: Dispersion parameters extracted from a quadratic fitting of both curves featured in Fig. 4.2.

The parameters sought after are shown in Table 4.2 for both curves. A very good agreement is found between both measurement methods, as far as β_3 is concerned. The order of magnitude and sign of β_4 is also consistent, even though some bias is expected on this parameter for it is very complex to know the fourth order dispersion of the balancing fiber (SMF-28). Then remains the case of ZDW, which differs significantly from one interferometric measurement to the other. It should be noted that the manufacturer specifies a ZDW at 1569 nm for this fiber. The parameters in Table 4.2 do not yield a proper fitting of the MI detuning presented in Fig. 4.2(b), when combined with reasonable values for γ. A possible explanation is the fact that the HNLF used for the MI measurement was 350 m long, while a 3 m sample only was cut to perform the interferometric one for balancing reasons. The fluctuating ZDW in HNLFs can therefore explain the discrepancy, even though a 3 nm variations seems large. Nonetheless these results provide valuable landmarks in order to test empirically the capabilities of HNLF (b) for broadband FWM, described in the second section of this chapter.

4.1.2. Thulium-doped fiber characterization

The underlying project idea - utilizing optical fibers and components available in the telecom band to create a versatile SWIR parametric converter - benefits from the absorption cross section of Tm^{3+} ions in silica near 1.6 µm [4.2]. It corresponds to exciting electrons from the $^3H_6$ to the $^3F_4$ manifolds, before they de-excite in a non-radiative way within this same manifold and emit a SWIR photon to return to the ground state (see Fig. 4.3(a)) [4.3]. Usually, high power emission from this transition is achieved by

pumping doped fibers with high-power diode lasers near 790 nm. That way the $^3H_6$-$^3H_4$ transition is stimulated instead, which leads to the emission of two signal photons through a cross-relaxation of neighboring ions [4.4]. However lasers and amplifiers of lower output power generally use the abovementioned C- or L-band pumping scheme. These realizations leverage the extremely broad emission cross-section of thulium in silica, as illustrated by Fig. 4.3(b), and encompass small signal amplifiers [4.5] or high optical signal-to-noise ratio (OSNR) lasers [4.6] between 1.85 and 2.05 µm. The amplification of short-wave signals near 1.7 µm has also been demonstrated [4.7], thanks to the quenching of the emission beyond 1.9 µm with a holmium-doped fiber piece. In this case, Tm:silica behaves like a quasi-three level system, and it is possible to shift the fluorescence spectral peak (closely linked to the gain peak) by acting on the pumping power, the pumping direction with respect to the signal direction, or the fiber length. These schemes will be detailed later on, but the regions of the fiber where the population inversion is not reached essentially behave like absorbers for wavelength shorter than 1.9 µm. The absorption progressively vanishes for lower energy photons, as can be deduced from Fig. 4.3(b).

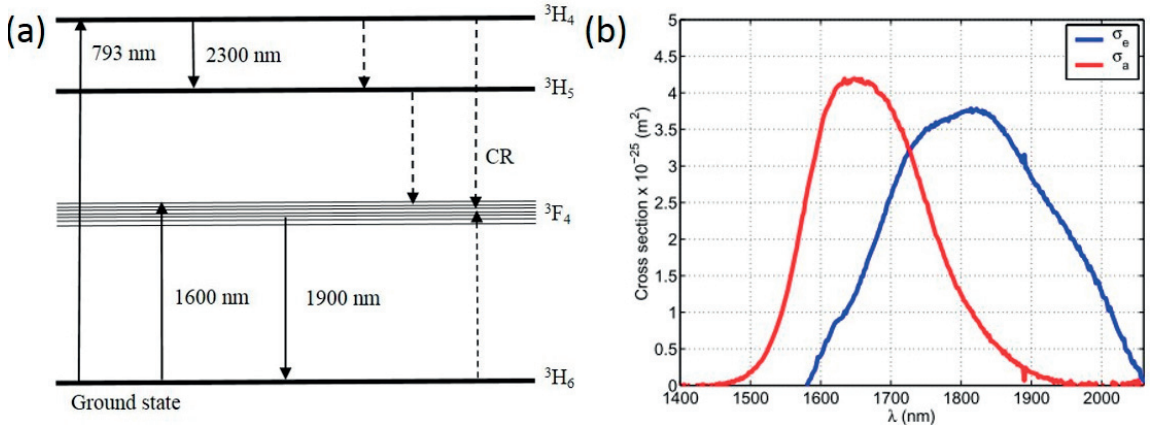

Figure 4.3: (a) Partial energy level diagram of Tm3+ ions. Data are from [4.8], with a correction brought on the $^3H_4$ and 3F4 manifolds, which were mistaken until recently [4.4]. Solid arrows indicate radiative transitions, while the dashed arrows indicate non-radiative ones. CR indicates a cross relaxation, where an ion's non-radiative decay causes the excitation of another neighboring ion to the $^3F_4$ level. (b) Experimental absorption (red curve) and emission (blue curve) cross section of Tm:silica. Adapted from [4.2].

These various realizations underline the range of operation of such amplifiers, and how they can advantageously be coupled with a SWIR converter stage pumped in C- or L-band. Since we work in the non-depletion regime, a large fraction of pump power can be re-used to amplify the idler. For the sake of simplicity, we opted for a commercial, core-pumped TDF, namely the OFS TmDF200 [4.9]. This fiber is single mode at 2 µm, and its mode-field diameter is specified by the manufacturer to be 5 µm at a wavelength of 1700 nm. Having a core size commensurate with that of a HNLF facilitates fibers splicing, in order to make the HNLF-TDF assembly robust. Splicing to SMF-28 pigtails can also be realized with

losses below 0.5 dB per splice. Even though no significant Kerr-related effect is expected to take place in the TDFA stage, we have submitted our TDF to an extensive characterization of its dispersive and nonlinear properties [4.10].

The MI generation method is not expected to be fruitful at 2 μm since the fiber dispersion is not engineered for nonlinear applications in this band. However, if FWM can be performed in CW regime in this band, precious information about the nonlinear coefficient, the attenuation and the dispersion can be extracted from the CE spectrum. Experimentally generating the CE spectra is nonetheless much more time consuming and equipment intensive, especially at 2 μm, than the MI detuning method. For this reason, we probed FWM in the TDF at three pump wavelengths only. The setup for FWM characterization is shown in Fig. 4.4(a). Two custom-made, polarized, CW, thulium-doped fiber lasers (TDFL) are used to generate the pump and the signal (with a degree of polarization better than 18 dB). Both consist of a unidirectional ring cavity, in which the wavelength-selective element is either a fiber Bragg grating in conjunction with a circulator (for the pump) or a tunable bandpass filter (for the signal). The pump laser is first amplified in a commercial TDFA before being combined with the signal laser via a 50/50 coupler. Both waves are then directed toward the 25 m long FUT, where FWM along the propagation gives rise to an idler wave. The filter in the signal laser cavity allows for its wavelength to be tuned from 1920 nm to 2020 nm, and to reconstruct the CE spectrum as a function of the pump-signal detuning. Typical FWM spectra are displayed in Fig. 4.4(b)-(c), for parametric pump wavelengths of 1980 and 2000 nm, respectively. On the long wavelength side of the pump, we observed strong spontaneous emission from the booster as well as from the FUT. The latter is due to absorption around 2 μm originating from the $^3F_4 \rightarrow {}^3H_6$ transition. The signal was therefore deliberately positioned on the Stokes side of the pump such that idlers are created on the anti-Stokes side, where the reduced ASE enables the detection of low amplitude waves. This enables a precise measurement of the idlers intensity, and the observation of a clear CE ripple due to large fiber dispersion. Moreover, some attenuation at 2 μm is caused by intraband absorption in the $^3F_4$ manifold and must be taken into account in the CE modelling. In the presence of propagation losses, the signal-to-idler parametric conversion in the degenerate FWM case is described by an analytical function significantly more complex than Eq. 2.16, which involves Bessel functions of complex order [4.10]. However, a fitting toolbox allowed us to obtain fitted CE curves such as the one shown in Fig. 4.4(d) for a 2000 nm pump. The parameters retrieved from these three fittings are given in Table 4.3.

Pump wavelength (nm)	β_2 $(\mathrm{ps}^2/\mathrm{km})$	$\gamma(\mathrm{W}^{-1}\mathrm{km}^{-1})$	$\alpha(\mathrm{dB/m})$
1980	-18.7	4.1	0.12
2000	-19.8	3.8	0.07
2008	-20.5	3.57	0.06

Table 4.3: Extracted TDF parameters in the 2 μm band.

One readily sees that the attenuation decreases for longer wavelengths, as expected from the measured Tm^{3+} absorption cross section. The dispersion values were once again cross-checked with an interferometric method and confirmed. The fiber is strongly anomalous, which may give rise to solitonic propagation in pulsed sources. But more importantly, the nonlinear coefficient is fairly high, 4 to 5 times more than that of an SMF-28 at these wavelengths. This feature probably comes from the aluminum oxide and lanthanum oxide doping of the core, which is known to raise the glass Kerr coefficient [4.11]. Dispersion changes under population inversion were also probed, but not detected, contrarily to observations in erbium [4.12].

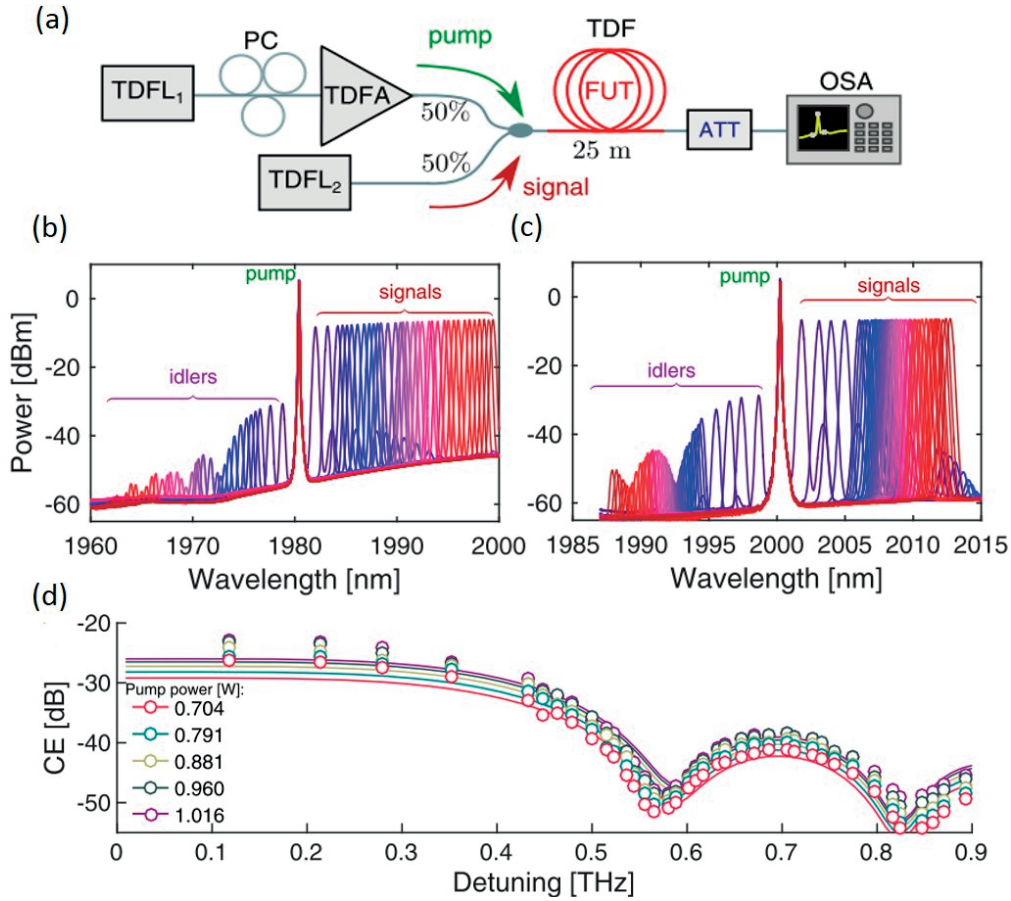

Figure 4.4: Experimental setup for the FWM characterization of the FUT: TDFL, thulium-doped fiber lasers; TDFA, thulium-doped fiber amplifier; PC, polarization controller; OSA, optical spectrum analyzer; ATT, attenuator. (b)-(c) Superimposed spectra at the FUT output for a range of pump-signal detuning, and pumping wavelengths of 1980.4 nm (b) and 2000.2 nm (c). (d) CE spectrum for a pump wavelength of 2000 nm, and for five pump powers between 0.7 and 1 W. Circles represent experimental data points while the solid are optimal fits using an analytical model taking loss into account.

4.2. Continuous-wave thulium enhanced parametric converter

4.2.1. Wavelength conversion in the HNLF

According to the parameters obtained with the MI method for HNLF (b) (from now on just called HNLF), pumping this 350 m long fiber near 1566 nm should entail narrow-band CE peaks centered at 1318 nm and 1927 nm, as seen on Fig. 4.5 (a). The theoretical peak value is extremely high, namely more than 130 dB with a 34.5 dBm (2.8 W) CW pump. Nevertheless this value is calculated using the non-depleted pump approximation, and any signal injected in the fiber would undergo such a large amplification that it would ultimately deplete the pump and drastically reduce the actual CE. [4.13]. Moreover, it does not take the impact of dispersion fluctuations into account. From the previous chapter, we know that they are likely to severely lower and broaden the parametric gain. The experimental setup for broadband parametric conversion is described by Fig 4.5(b). Two tunable semiconductor lasers generate the pump and the signal, in the C-band and O-band, respectively. They are standard external-cavity CW diode lasers, with a linewidth in the order of 100 kHz and an output power in the milliwatt range. The pump is set at 1565.6 nm and amplified in an EDFA while the latter is tunable in the O-band and amplified in a suitable semiconductor optical amplifier (SOA). The polarization of both lasers is adjusted independently to inject them in the same polarization state into the HNLF, in order to maximize FWM. Phase-modulation is applied to the pump laser to broaden its spectrum and prevent SBS. Both lasers are coupled in a near-lossless fashion through a wavelength multiplexer (WDM) and are then directed to the HNLF. The output of the HNLF is then connected to an OSA for analysis. For all FWM experiments, given the high pump powers used, an optical attenuator is inserted before the OSA to prevent damage. Unfortunately, such attenuator always features some chromaticity (wavelength dependent loss) over the range of interest. The power levels extracted from the spectra are therefore corrected by the attenuator transmission spectrum. The spectra obtained when the signal is swept over the O-band are shown in Fig. 4.5(c), and the corresponding CE on Fig. 4.5(d). The spectra are uncorrected and only feature relative powers, while the CE takes the chromatic attenuation into account.

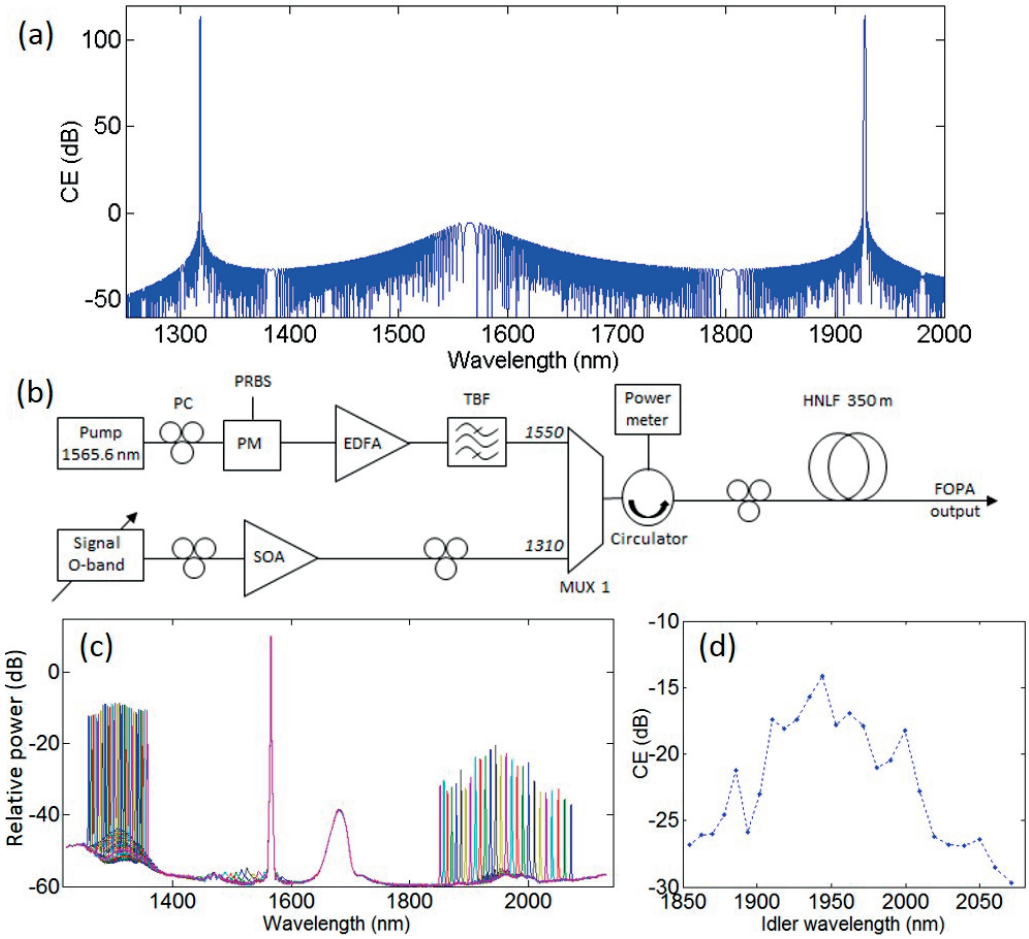

Figure 4.5: (a) CE computed for our HNLF with a 34.5 dBm CW pump set a 1565.6 nm. (b) Experimental setup built to experimentally measure this CE, with PC: polarization controller, PM: phase modulator, PRBS: pseudo-random bit sequence, EDFA: erbium-doped fiber amplifier, TBF: tunable bandpass filter, SOA: semiconductor optical amplifier, MUX 1: 1310/1550 nm multiplexer. A circulator is used to monitor the pump power backscattered due to SBS. (c) Superimposed experimental FWM spectra obtained at the HNLF output when the signal is swept over the O-band. Some Raman scattering is visible near 1650 nm. (d) Corresponding CE around the SWIR peak.

The experimental CE lobe peaks at -14 dB near 1950 nm, is approximately 100 nm wide at -10 dB and features a value higher than -25 dB from 1900 nm to 2000 nm. This is obviously much broader and lower in practice than the calculation right above. This was expected from the basic ZDW fluctuation model described in chapter 3. The signal-pump detuning is very large (36 THz), making the FOPA dramatically sensitive to dispersion fluctuations. The HNLF length (350 m) also entails a large cumulated fluctuation value. It is possible to fit the CE spectrum with the lumped fluctuations model described previously [4.14]. A set of realistic parameters that yields an acceptable fit in terms of CE width is the following: a ZDW standard deviation of 0.6 nm and a correlation length of 6 m. Additionally, this ZDW map of this HNLF had been established previously, and is reported in Fig. 2(b) in [4.15]. From this curve, our correlation length choice appears consistent, but the standard deviation used in our model is larger than the

measurement. It also confirms that the mean ZDW is very close to 1569 nm. It is hard to ascertain these parameters values, especially since this reference mapping cannot retrieve the ZDW in the first and last meters of the fiber. Anyways knowing the exact value has limited practical importance since we can experimentally measure the CE flattening. Moreover, this effect has two major benefits. Firstly, it broadens the CE bandwidth and permit a large tuning span for the idler wavelength without having to change the pump wavelength in order to phase-match FWM [4.16]. Some CE is lost when the idler is detuned from 1950 nm, but the -10 dB bandwidth still amounts to more than 100 nm. Secondly, given the low CE value and the input signal power (here close to 100 mW), the converter operates in the small signal regime. As a consequence, it is possible to project several O-band signals simultaneously toward SWIR without reducing the CE compared to the single-signal case, as will be discussed later in this dissertation. Finally, considering that the O-band SOA can boost the signal up to 100 mW, the mean CE value around 1950 nm is sufficient to generate an appropriate SWIR seed for the TDFA stage downstream.

4.2.2. FOPA-TDFA assembly

Two types of amplification stages are considered after the FOPA. The first is designed to amplify optimally shorter-wave SWIR idlers, roughly below 2 μm. It simply consists of a 4.5 m piece of TDF (TmDF200) directly spliced at the HNLF output. The large C-band power transmitted through the FOPA presented above (32 dBm, 1.58 W) efficiently pumps this amplifier. Using a relatively long TDF completely depletes the C-band wave and transfers its power to the idler. Moreover, thulium also absorbs at the longer edge of the O-band. This greatly simplifies the filtering at the source output, as no long-pass filtering is necessary to discard the excess of pump power. The second amplifier configuration aims at boosting longer-wave idlers (above 2 μm) and is described later.

The spectra obtained at the output of the FOPA-TDFA for various idler wavelength are shown in Fig. 4.6(a) in the shorter-wave configuration. Thanks to the efficient re-use of the pump energy, an amplified idler power exceeding 700 mW can be obtained from 1867 nm to 1958 nm, with a 4 dB ripple only [4.14]. This level of output power corresponds to an optical power efficiency of 25% considering an initial pump power of 2.8 W, a record for SWIR FOPAs operating in CW, especially considering the TDFA relative quantum defect (roughly 20% when pumped in the L-band). As a matter of fact, a low power ripple is an important feature for applications requiring wavelength tuning. Comparing to the output of the HNLF, the tuning range is reduced from more than 200 nm to approximately 90 nm. This is due to parasitic lasing out of the idler band, as seen in Fig. 4.6(b). Parasitic lasing occurs when the CE in the HNLF is too low, which results in an idler power that cannot properly seed the TDFA. Since the ion pumping level is kept constant no matter how much idler comes in, some unwanted reflections in the setup cause an unstable

lasing near the peak of the thulium SWIR gain, located near 1850 nm. This mainly happens for idler wavelengths longer than 1960 nm, due to a combination of reduced CE and reduced SOA saturated power for shorter-wave signals. Fig. 4.6(b) shows a static image of several parasitic lasing modes, but the process is very unstable and random, and the modes switch from an OSA sweep to the other.

Results for the simultaneous injection of two and three O-band signals are shown in Fig. 4.6(c) and (d), respectively. In the two-signal case, the 1310 nm and 1303 nm waves are transparently converted to the SWIR at 1947 nm and 1962 nm, respectively. Even though the two idlers suffer from gain competition in the TDFA, a power of approximately 150 mW is obtained for both. In the three-signal case, the idlers are generated at 1886 nm, 1926 nm and 1947 nm and their power range between 14 mW and 150 mW. It can also be seen that some FWM takes place between the amplified idlers, as underlined by the red circles in Fig. 4.6(c) and (d). This interaction is likely to take place in our small core TDF due to its relatively high nonlinearity (as characterized in the previous section) and the relatively high idler powers at play.

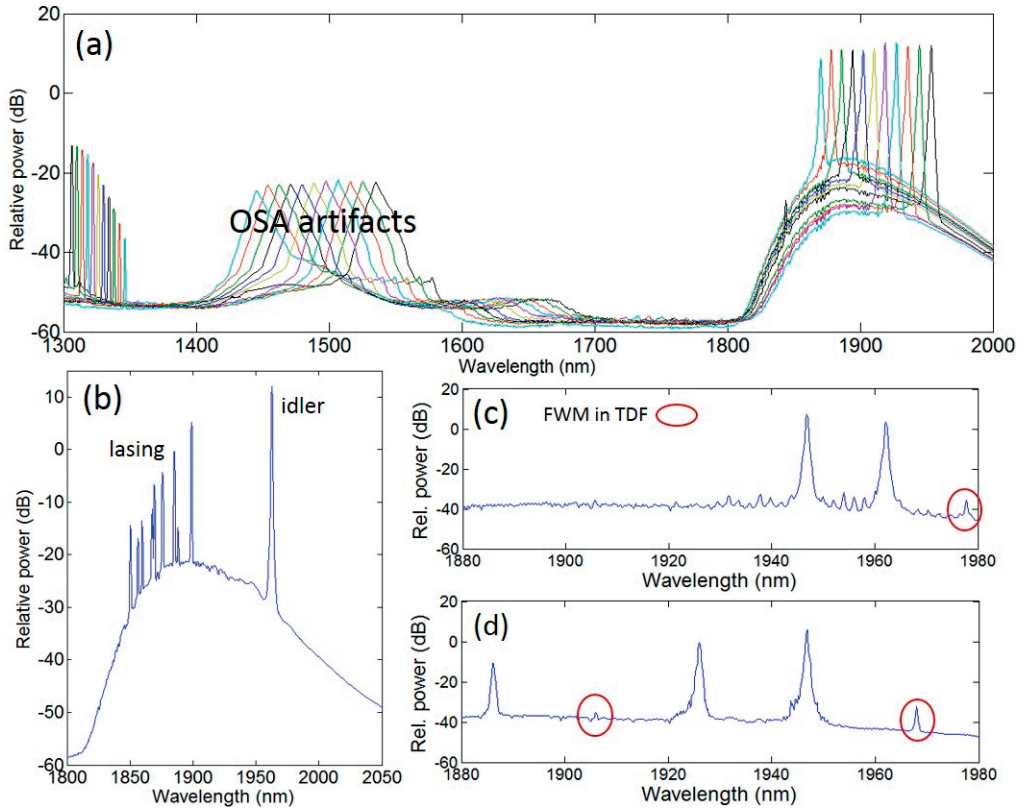

Figure 4.6: (a) Superimposed spectra at the output of the 4.5 m TDF, spliced to the FOPA, when the idler wavelength is swept over part of the O-band. The peaks near 1500 nm are measurement artifacts due to second-order diffraction lobes in the grating-based OSA, and are ghost images of the SWIR lines. (b) For idler wavelengths longer than 1960 nm, parasitic lasing takes place at the peak of thulium-gain and degrades the source performances. (c)-(d) Spectrum after the TDF when 2 (c) and 3 (d) signals are Injected along with the pump in the HNLF.

In order to extend the SWIR reach while avoiding parasitic lasing in the TDFA, it is possible to engineer the thulium amplifier as a multi-stage architecture. Multi-stage setups have been demonstrated for EDFAs [4.17] or TDFAs [4.5] to obtain long-band amplification. In our case such solution can also be implemented, where the L-band wave only pumps the second fiber, thanks to wavelength multiplexers. The ion population from the first TDF piece is inverted by the backward propagating ASE from the second fiber piece, as depicted in Fig. 4.7(a). This long-wave in-band pumping favors the amplification of signals of which wavelength is redshifted compared to the natural thulium fluorescence. The FOPA-TDFA output spectra are shown in Fig. 4.7 (b), and are lasing-free. The source in this configuration is tunable from 1935 nm to 1980 nm with a CW power of about 21 dBm showing a ripple below 0.5 dB. As expected the gain in the dual stage TDFA is slightly red-shifted. The C-band pump is still totally absorbed while the O-band signals are also strongly attenuated. The maximum output power is unfortunately decreased due to the loss undergone by the pump in the various splices and WDMs, but the tuning range is effectively extended by about 30 nm. In summary, these two realizations demonstrate how we leveraged the massive cumulated ZDW fluctuations in long HNLFs to demonstrate in a mode-hop free tunable SWIR parametric source. Compared with previously demonstrated SWIR transmitters [4.18] [4.16], the flat tuning range, power levels and CW operation are major additions.

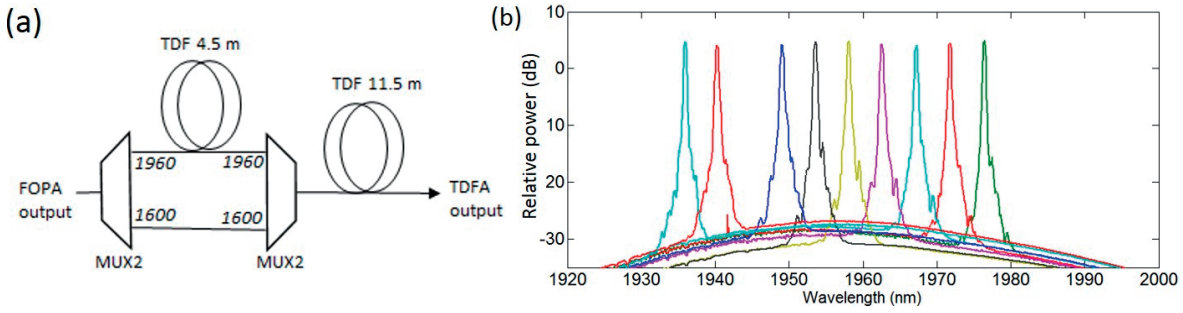

Figure 4.7: (a) Experimental setup of the long-wave TDFA with MUX2: 1600/1960 nm wavelength multiplexer. (b) Superimposed spectra at the output of the composite amplifier, when the idler wavelength is swept over part of the O-band.

4.2.3. FOPA-TDFA-HDFA assembly

In order to obtain an even longer output wavelength without parasitic lasing near the spectral band of interest, it is necessary to resort to another rare-earth dopant for silica, namely holmium (Ho). This element is already used to make long-band amplifiers beyond 2 µm, pumped by TDF lasers [4.19]. One of its transitions ($^5I_8$ – $^5I_7$) can be excited by a pump laser at 1950 nm, which then emits around 2050 nm, after a small non-radiative decay in the $^5I_7$ manifold. The lasing scheme is again a quasi-three level system, and therefore the absorption and emission cross sections of Ho overlap significantly, as shown in Fig. 4.8(a) [4.20]. It is therefore necessary to adjust correctly the doped fiber length with respect to the

available pumping power, to prevent the un-pumped segment of the fiber to re-absorb the idler. The way to include a holmium-doped fiber amplifier (HDFA) stage in our setup is depicted in Fig 4.8(b). Since we do not wish to use an external 1.95 µm pump, it is necessary to generate this pump parametrically in the HNLF. Two O-band signals are therefore simultaneously injected in the FOPA, in such a way that one fixed idler be generated at 1950 nm and another be tunable idler between 2000 nm and 2100 nm. The output is then directed to the TDFA stage as previously, where the 1950 nm idler located at the peak of the thulium gain undergoes a significant amplification while the tunable idler is transparently transmitted. Finally, the holmium-doped fiber (HDF) is directly spliced at the output of the TDF, where the power can be transferred from the shorter-wave idler to the longer-wave one [4.21].

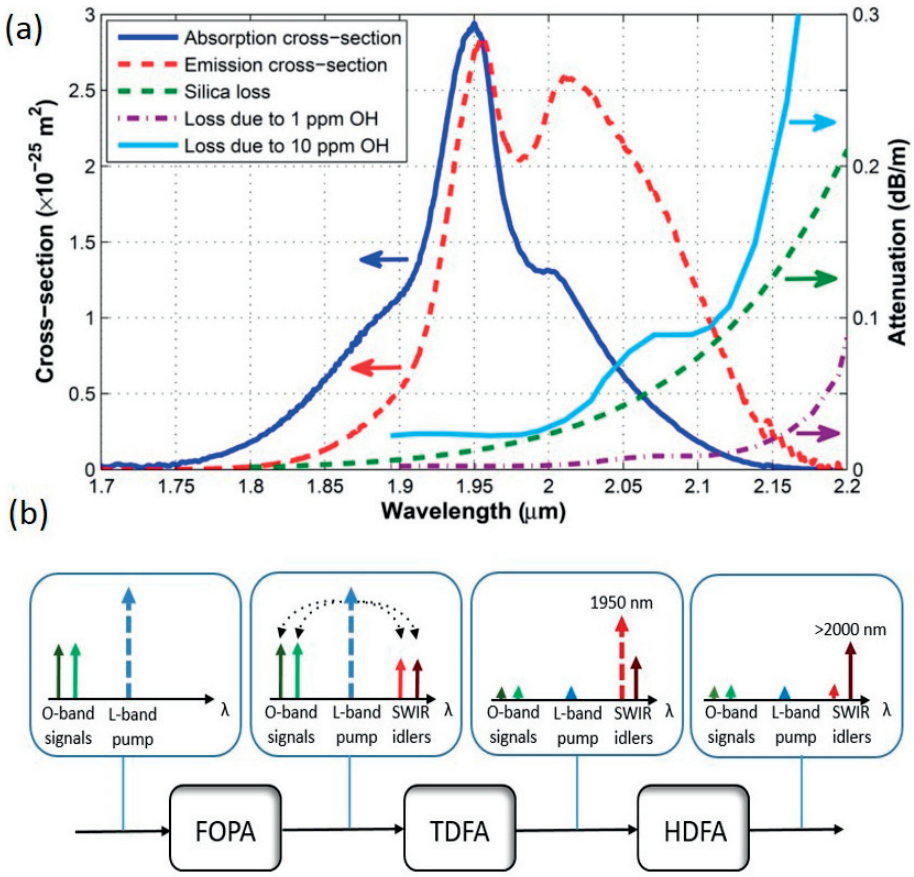

Figure 4.8: (a) Emission and absorption cross section of Ho:silica. The loss due to the silica host and OH inclusions are also shown. Adapted from [4.20]. (b) Schematic of the idlers generation and amplification in each stage. The dashed arrows correspond to the pump before each stage: the blue arrow is the pump for both the parametric process and the TDFA, the light red arrow is the pump for the HDFA while the dark red arrow is the tunable output.

The experimental setup built to realize the experiment is described in Fig. 4.9(a). In this study, the HDF used is a dual-clad fiber made by Nufern (SM-HDF-10/130 [4.22]), of which 10 µm wide core enables single mode propagation of the idler. However, the dual-clad architecture can be a problem for splicing to

single-clad fibers such as our TDF or SMF-28. We were able to maintain a splicing loss below 0.5 dB. On the FOPA side, it is necessary to slightly adjust the pump wavelength to reach a proper balance in terms of the CE experienced by the two idlers in the 350 m long HNLF. The pump was therefore positioned at 1567.5 nm. Moreover, red-shifting the pump permits the generation of idlers beyond 2100 nm, where holmium still amplifies efficiently. Considering the seeding of the TDFA stage (made of a 4.5 m long TDF), two constraints must again be taken into account. On the one hand, it is necessary to maximize the 1.95 μm idler power before the TDFA to limit parasitic lasing. On the other hand, it is desirable to have the highest tunable idler power after the FOPA. As the HDFA gain is not saturated in our setup, the whole source output power around 2050 nm scales linearly with the longer-wave idler power after the FOPA. Some results obtained after the FOPA and TDFA are described in Fig. 4.9(b)-(d), where the fixed O-band signal is positioned at 1311 nm resulting in a 1947 nm idler. The pump power for this experiment is 2.63 W. Unfortunately, one notices significant parasitic lasing after the TDFA, near 1850 nm. This was unavoidable given the loss in the fiber coupler used to combine the O-band signals. Both signals are amplified in independent SOAs up to 100 mW, but their power drops to 50 mW after the 50/50 fiber coupler. Placing the SOA downstream did not help since gain competition, as well as nonlinear interaction between both signals, also reduces the output power while increasing the polarization management complexity. The best option would be to use a lossless WDM designed specifically for O-band, but such element was not available at the time of the experiment. Another option is to use more powerful O-band amplifiers. Nevertheless, parasitic lasing takes place spectrally far from the targeted band, and will be partially absorbed in the HDF.

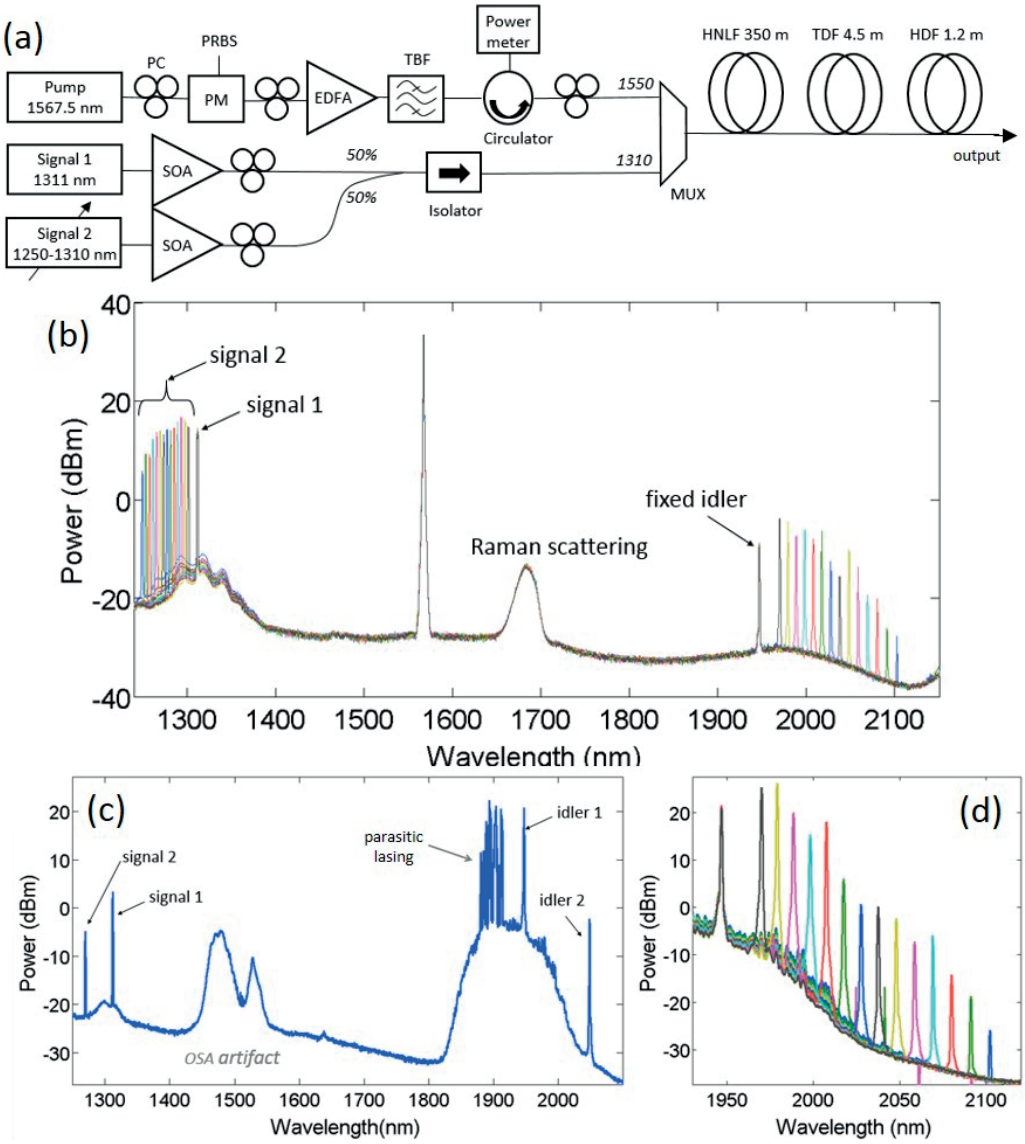

Figure 4.9: (a) Experimental setup with the dual-signal injection is the HNLF. A circulator is used to monitor the backscattered pump power due to SBS. (b) Superimposed FWM spectra after the 350 m HNLF. (c) Large span spectrum after the 4.5 m TDF, showing parasitic lasing near 1850 nm and some signal absorption. (d) Superimposed spectra after the TDFA when the longer-wave idler wavelength is swept. Very little amplification takes place in this stage beyond 2020 nm.

The longer-wave idlers amplified by the HDFA stage are shown in Fig. 4.10(a), with a zoom in Fig. 4.10(b) to better appreciate the linewidth and OSNR. Fig. 4.10(c) gives an evidence of how beneficial it is to use a HDFA stage to increase the long-wave gain. It plots the idlers power after each amplification stage, divided by the corresponding input signal power. As the parametric CE and the thulium gain dramatically drop beyond 2000 nm, the holmium gain catches it up and enables a clear red-shift of the conversion band compared to a simple FOPA-TDFA. The CW source is capable of delivering up to

15 dBm in the 2010 – 2070 nm range with a power ripple lower than 3 dB. This level of CW power is higher than what is generally achieved by semiconductor diode lasers, and comes in addition to a much wider a tuning range. Overall, the entire 1965 – 2100 nm spectral range is accessible. It is worth mentioning that compared to the previous stage output, the output power is well equalized beyond 2 µm with the help of the HDF. The L-band pump is totally absorbed and only a slight fraction of the 1947 nm idler flows through the HDF. As a matter of fact, after the HDFA, we reach parametric transparency (CE>0 dB from the O-band to long SWIR) and we achieve an OSNR larger than 25 dB. Once again, a more efficient coupling and amplification scheme in the O-band, upstream of the HNLF, would unlock larger output power near 2100 nm. However, there is a hard limit on the short side of the O-band for the signal, dictated by the tunable laser and the SOA. On the close-up view on the idler spectra, one also notices the broadening due to the 7 GHz pump phase dithering, which strongly reduces the pump coherence. This feature of CW FOPAs can be prejudicial for some applications, such as precision spectroscopy. Consequently, it is desirable to quench SBS with a more effective bandwidth use. Pulsed pumping is a viable option, as analyzed in the next chapter.

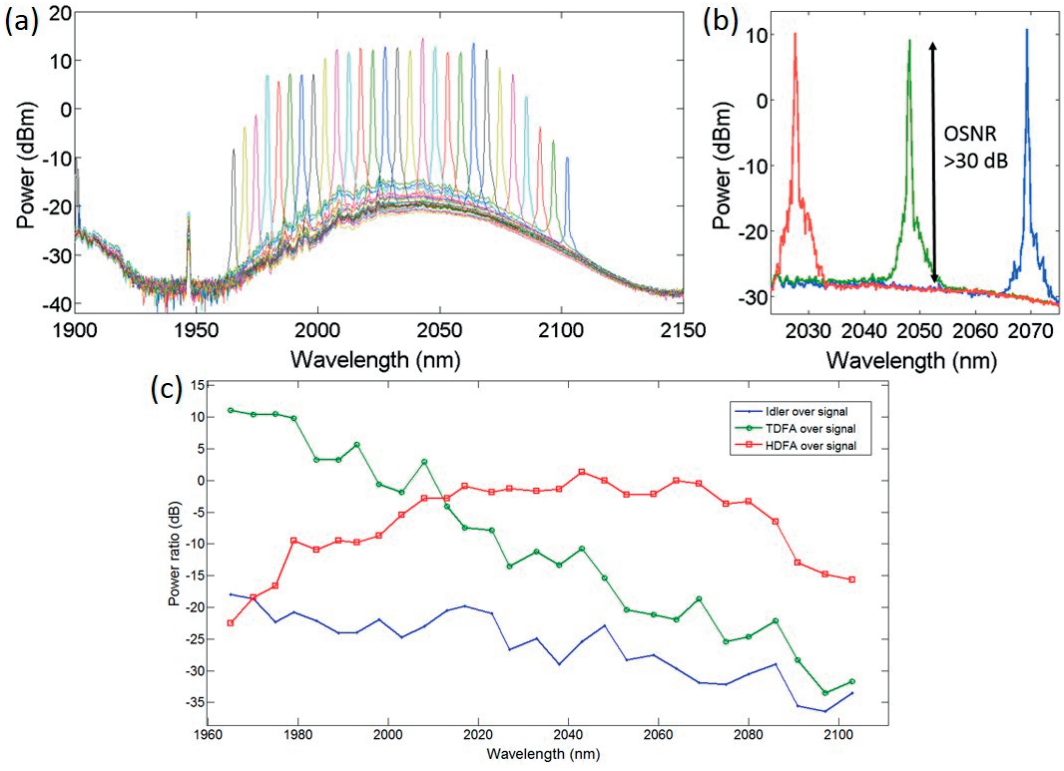

Figure 4.10: (a) Fig. 6. (a) Superimposed spectra of the amplified idlers after the HDFA, when the signal is shifted from 1250 to 1300 nm. The absorption of Ho at 1950 nm is clearly visible. (b) Spectral zoom on three amplified idlers at 2028 nm, 2048 nm and 2069 nm, with OSNR: optical signal-to-noise ratio. (c) Ratio of the idler power over its corresponding signal power (measured before the HNLF) after the conversion in the FOPA (blue), the amplification in the TDFA (green) and the amplification in the HDFA (red).

4.3. References

[4.1] B. Auguié et al., "Ultra low chromatic dispersion measurement of optical fibers with a tunable fiber laser," IEEE Photon. Technol. Lett. 18, 1825-1827 (2006).

[4.2] S. D. Agger et al., "Emission and absorption cross section of thulium doped silica fibers," Opt. Express 14, 50-57 (2006).

[4.3] S. D. Jackson, "The spectroscopic and energy transfer characteristics of the rare earth ions used for silicate glass fibre lasers operating in the shortwave infrared," Laser & Photon. Rev. 3(5), 466–482 (2009).

[4.4] S. D. Jackson, "Towards high-power mid-infrared emission from a fibre laser," Nat. Photonics 6(7), 423–431 (2012).

[4.5] Z. Li et al., "Thulium-doped fiber amplifier for optical communications at 2 μm," Opt. Express 21, 9289-9297 (2013).

[4.6] Z. Li et al., "All-fiber, ultra-wideband tunable laser at 2 μm," Opt. Lett. 38, 4739-4742 (2013).

[4.7] Z. Li et al., "Exploiting the short wavelength gain of silica-based thulium-doped fiber amplifiers," Opt. Lett. 41, 2197-2200 (2016).

[4.8] A. Godard, "Infrared (2–12 μm) solid-state laser sources: a review," C. R. Phys. 8(10), 1100–1128 (2007).

[4.9] http://fiber-optic-catalog.ofsoptics.com/item/rare-earth-doped-optical-fibers/ytterbium-and-thulium-doped-optical-fiber/tmdf200-2 (consulted in August 2016).

[4.10] S. Kharitonov et al., "Kerr nonlinearity and dispersion characterization of core-pumped thulium-doped fiber at 2 μm," Opt. Lett. 41, 3173-3176 (2016).

[4.11] C. Karras et al., "Nonlinear refractive index study on SiO_2-Al_2O_3-La_2O_3 glasses," Opt. Mater. Express 4, 2066-2077 (2014)

[4.12] S. Fleming et al., "Measurement and analysis of pump dependent refractive index and dispersion effects in erbium-doped fiber amplifiers," IEEE J. Quantum Electron.32, 1113–1121 (1996).

[4.13] M. E. Marhic et al., "92% pump depletion in a continuous-wave one-pump fiber optical parametric amplifier," Opt. Lett. 26, 620-622 (2001).

[4.14] A. Billat et al., "High-power parametric conversion from near-infrared to short-wave infrared," Opt. Express 22, 14341-14347 (2014).

[4.15] F. Alishahi *et al.*, "Mapping dispersion fluctuations along optical fibers using brillouin probing and a fast analytic calculation," *CLEO: 2013*, San Jose, CA, 1-2 (2013).

[4.16] B. P.-P. Kuo et al., "Continuous-wave, short-wavelength infrared mixer using dispersion-stabilized highly-nonlinear fiber," Opt. Express 20, 18422-18431 (2012).

[4.17] J. Lee et al., "Enhancement of power conversion efficiency for an L-band EDFA with a secondary pumping effect in the unpumped EDF section," IEEE Photon. Technol. Lett. 11(1), 42–44 (1999).

[4.18] J. M. Chavez Boggio et al., "Tunable Parametric All-Fiber Short-Wavelength IR Transmitter," J. Lightwave Technol. 28, 443-447 (2010).

[4.19] N. Simakov et al., "High gain holmium-doped fibre amplifiers," Opt. Express 24, 13946-13956 (2016).

[4.20] N. Simakov et al., "A cladding-pumped, tunable holmium doped fiber laser," Opt. Express 21, 28415-28422 (2013).

[4.21] A. Billat et al., "Broadly tunable source around 2050 nm based on wideband parametric conversion and thulium–holmium amplification cascade," Opt. Express 22, 26635-26641 (2014).

[4.22] http://www.nufern.com/pam/optical_fibers/1173/SM-HDF-10_130/ (consulted in November 2016).

Chapter 5 Parametric conversion in modulated and pulsed regime

After the presentation of the CW operation of the FOPA-TDFA in the previous chapter, this one deals with the intensity modulated regime. That regime provides our source with a competitive advantage over conventional approach, often unable to output an arbitrary modulated waveform. As reviewed in the introductory chapter, the ability to generate a large number of SWIR data channels in a single source could become of interest for communication in hollow-core fibers. Alternatively, pulsed lasers are the emitters of choice in time-domain reflectometry CO_2 LIDARs. Besides, keeping in mind that the SWIR output we generate in this stage is intended to pump the MIR parametric converter, flexibility is required. In the first section, we experimentally study the conversion of a Gbit/s non-return-to-zero on-off-keyed (NRZ-OOK) data train from O-band to SWIR. The next section presents some theory and experimental results concerning the pulsed pump operation of the FOPA-TDFA, which implies a significant increase of the pump instantaneous power. It is also possible to imprint data modulation on the pump pulse train, and the next section reports architectures able to transmit return-to-zero on-off keying (RZ-OOK) data sequences. Finally, a parenthesis is opened in the last section to rapidly present a side project, aimed at creating a tunable SWIR pulse source based on cascaded Raman scattering.

5.1. Signal modulation and tunable OOK generation

SWIR parametric transmitters able to encode data on the idler intensity [5.1] or phase [5.2] have been reported recently. Both setups rely on the injection into the HNLF of a CW pump, along with an amplitude or phase modulated signal. Such system is modelled as a CW FOPA, obeying the equations described in chapter 2. The idler is just an instantaneous linear replica of the signal. In the first demonstration, the authors could bring the bit rate of an intensity modulated signal up to 10 Gbit/s, quenching SBS in the 100 m long HNLF with a phase modulation driven by a 0.4 GHz broad RF noise source. However pump phase dithering is forbidden when the signal is modulated in phase, since the phase noise will be transmitted towards the idler and jam the phase-shift keying modulation. They used a piecewise strained HNLF, of which dispersion is insensitive to longitudinal elongation. In both of these experiments, the CE was however very low. Since we could not obtain a dispersion-stabilized HNLF, we opted for an OOK transmitter solution. The experimental setup is shown in Fig. 5.1(a). It is a straightforward derivation of the FOPA-TDFA presented previously, with an intensity modulator placed on the signal path before the HNLF. Idler filtering is performed after the TDF to suppress the ASE noise. A short length of TDF was used (1.4 m) given that the amplified idler power is not a primary concern for

this demonstration, and that powers compatible with telecom standards (of the milliwatt order) are still obtained. Moreover the reduced gain prevents any parasitic lasing to occur, which improves the OSNR after filtering. The O-band signal was intensity modulated at two rates: 7 Gbit/s and 10 Gbit/s, limited by the available equipment. The PRBS used to encode data on the signal was identical to that used for pump phase-dithering up to now, and is described in the previous chapter. Fig. 5.1(b) displays the back-to-back eye patterns, recorded on a fast photodetector before injection into the HNLF. The O-band signal was positioned at different wavelength to test the tunability of the OOK transmitter, while the pump was fixed at 1565.6 nm. Idler spectra at various wavelengths between 1900 nm and 2000 nm are shown in Fig. 5.1(c)-(d), after the FOPA and after the TDFA, respectively.

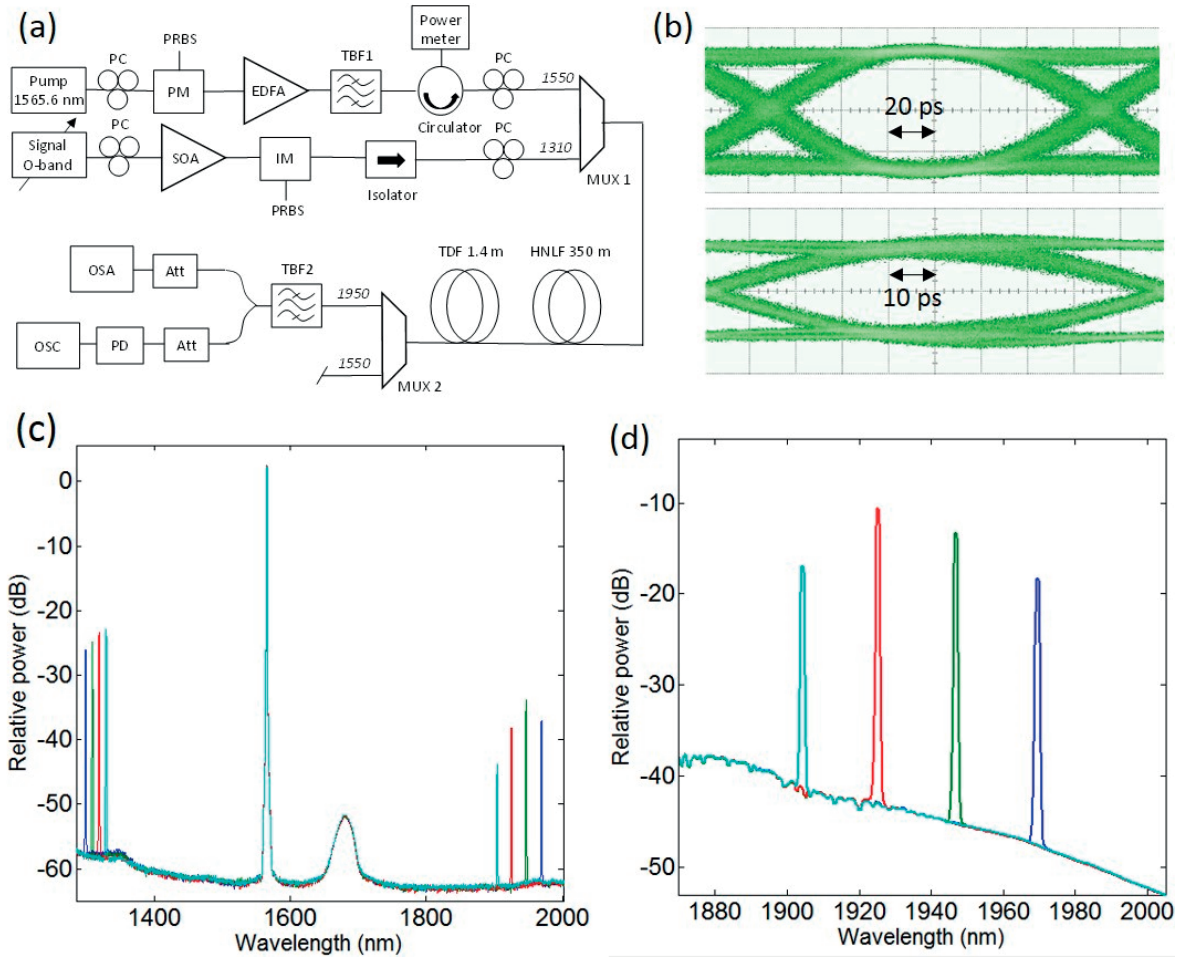

Figure 5.1: (a) Experimental setup, with TBF1: C-band tunable band pass filter, TBF2: SWIR tunable filter, Att: attenuator, PD: extended InGaAs 9 GHz bandwidth photodetector and OSC: digital sampling oscilloscope. (b) Signal back-to-back eye-patterns at a rate of 7 Gbit/s (up) and 10 Gbit/s (down). (c)-(d) Superimposed spectra for various idler wavelengths, recorded after the HNLF (c) and after the TDF (d).

We obtained an idler power after the TDFA between 2 and 9 dBm [5.3], which is generally sufficient for communication purposes. A 1.48 W CW pump was used, and yielded a conversion efficiency peaking at -15 dB for an idler at 1947 nm. This prevents any parasitic lasing to take place in the TDFA, and results in an OSNR larger than 25 dB for all the conversion band. After filtering, the SWIR eye patterns are recorded on a 9 GHz extended InGaAs photodetector, for each idler wavelength and each data rate. They are shown in Fig. 5.2. The eyes are wide open over the entire 60 nm tuning range for both bit rates. The observed noise is partly due to the ASE is the TDFA, and probably to the C-band laser fast frequency noise, which translate into idler intensity fluctuations after the FOPA [5.4]. The delayed Raman response of silica, which is visible in Fig. 5.1(c), can also play a role in FOPAs noise [5.5]. However the eye pattern is not sufficient to characterize the penalty in data transmission. The reference measurement is the bit-error ratio (BER), characterized with the help of an error detector connected to the photodetector at the end of the link. The error detector is synchronized with the input pattern generator, and can thus spot and count discrepancies between the input and output binary sequences. The maximum error rate tolerated for an OOK transmission is 10^{-9}. Yet when measuring the BER after our FOPA-TDFA, it was impossible to overcome a lower threshold of 10^{-7}. Nonetheless this value turned out to be repeatable and constant for all idlers, independently on the optical and electrical signal-to-noise ratio measured on the OSA, or on the oscilloscope. The same PRBS pattern generator was used to drive the pump phase dithering and the signal intensity modulator, for we lacked a bandwidth-efficient RF noise source similar to that used in [5.1]. We ascribed the constant BER to the pump phase dithering. The periodic frequency shift undergone by a phase-modulated pump translates into idler intensity modulation as the phase matching condition is periodically impacted [5.6]. These shifts probably happen at decision points during the BER sequence testing and result in this sub-optimal BER. In theory, the problem could be solved with a lower bandwidth RF noise generator. In spite of this limitation, the benefit of adding a TDFA stage in terms of wavelength tuning and power efficiency is underlined once again.

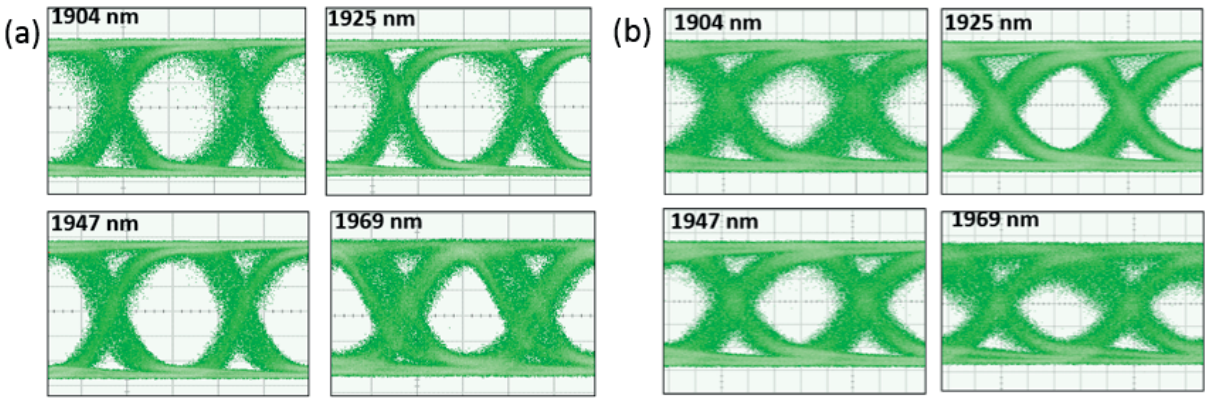

Figure 5.2: Idler eye patterns at various wavelengths, for a data rate of 7 Gbit/s (a) and 10 Gbit/s (b). The time per division is 50 ps for (a) and 20 ps for (b).

5.2. Pulsed pump parametric conversion

5.2.1. Theoretical considerations

In the following sections, we now consider the case of a degenerate pulsed-pump FOPA. We also keep assuming that the CE is significantly lower than 0 dB, which is experimentally confirmed. It means that FWM has almost no impact on the CW signal injected in the HNLF. Its time envelope is left unaffected, contrarily to the large parametric gain case. However, in the quasi-CW approximation, the generated idler is pulsed and its envelope features a quadratic dependence on the pump envelope function. The quasi-CW regime is a generally a fair approximation for nanosecond pulses [5.7], but the results we present here use much shorter pulses (<100 ps) in order to match the telecom data rates (of the GHz order at least). The modelling of short-pulse FWM should be performed with the help of the NLSE. Nevertheless the large detuning in our FOPAs renders the NLSE solving heavy and slow. Moreover, simulating CE spectra requires a large number of iterations to span the desired pump-signal detuning range. It is therefore interesting to adopt a hybrid approach where the pump evolution alone is modelled with the NLSE, while the CE is still calculated with the analytical formula given for the CW regime. The pump peak power is the quantity taken into account in this case. It also means that the idler power remains small enough to neglect SPM at 2 μm, and that the pump frequency excursion (due to its pulsed nature and to SPM) has a negligible impact on the phase-matching condition.

We target to use pulses that are of the order of 50 ps. Assuming a similar duration for the generated idler pulses, the first thing to assess is the walk-off distance in the HNLF. A walk-off between the pump and idler pulses larger than about 50 ps leads to the latter's stretching in time, and to a peak power reduction. From that respect, the large span interferometric dispersion measurement presented in Fig. 4.2 is of

primary interest. The time shift $\Delta\tau$ between two pulses (centered at frequencies ω_1 and ω_2), after propagation in a fiber length L, is given by the group velocity mismatch, as described in Eq. 5.1. Therefore integrating the measured second-order dispersion function allows the calculation of the curve presented in Fig. 5.3(a). From this curve we estimate that the HNLF should be no more than 45 m long to prevent 50 ps long pulses, centered at 1566 nm and 1950 nm, to walk-off completely in a linear propagation situation. The corresponding shift per unit length is 1.14 ps/m.

$$\Delta\tau = L|\beta_1(\omega_1) - \beta_1(\omega_2)| = L\left|\int_{\omega_2}^{\omega_1} \beta_2(\omega)\mathrm{d}\omega\right| \tag{5.1}$$

Additionally to avoiding walk-off, we wish to circumvent the pump spectral broadening. As seen previously the pump linewidth is necessarily transposed to the idler by energy conservation. Yet for application requiring a narrow SWIR or MIR linewidth, we want to keep the 2 μm output as narrow as possible. Assuming once again that we can decouple the pump propagation from FWM related effects, we simulate numerically the propagation of a pump pulse to assess its spectral broadening. A telecom band, sinc-shaped pulse (50 ps long at FWHM) with a peak power of 10 W is considered. Solving the NLSE then yields the result described in Fig. 5.3(b). The rectangular Nyquist pulse spectrum [5.8] is clearly distinguishable in the beginning, but it broadens after 100 m of propagation to an unacceptable width of more than 1 nm.

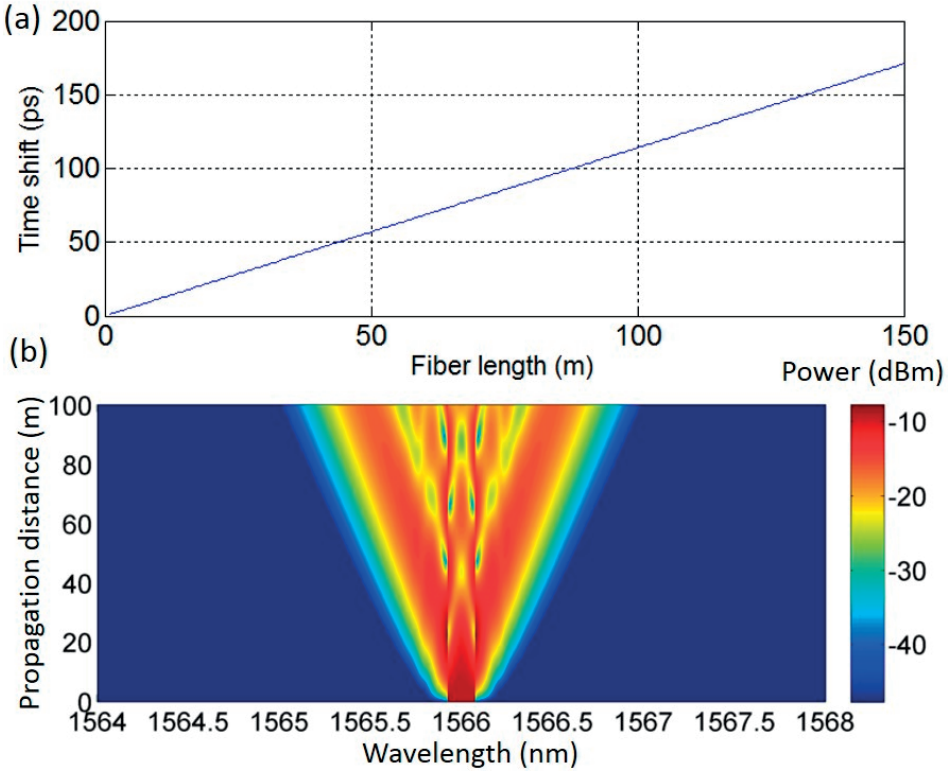

Figure 5.3: (a) Time shift between two pulses (centered at 1566 nm and 1950 nm) due to group velocity mismatch in our HNLF, as a function of fiber length. (b) Spectral evolution of a 1566 nm sinc-shaped pulse of 50 ps duration at FWHM, and 10 W peak power, in the same fiber.

For the sake of comparison between experiments and simulations, the spectrum of a 50 ps long sinc-shaped pulse (7 W peak) is plotted for both cases in Fig. 5.4, before and after propagation in the 350 m long HNLF. In the experimental case (left plot), the initial pulse is slightly distorted by the amplifier used, which may justify why some energy is still located around the carrier frequency after propagation. Nonetheless we find a very good agreement concerning the extent of the spectral broadening. Such a multiple lobe ejection is a signature of SPM in presence of a very low dispersion [5.9], which turns out to be the case in HNLF at 1566 nm. It shows again that a reduction of the HNLF length compared to the CW case is mandatory, at the expense of a reduced parametric gain. However keeping Eq. 2.16 in mind, a reduction of L can eventually be compensated by a pump power increase.

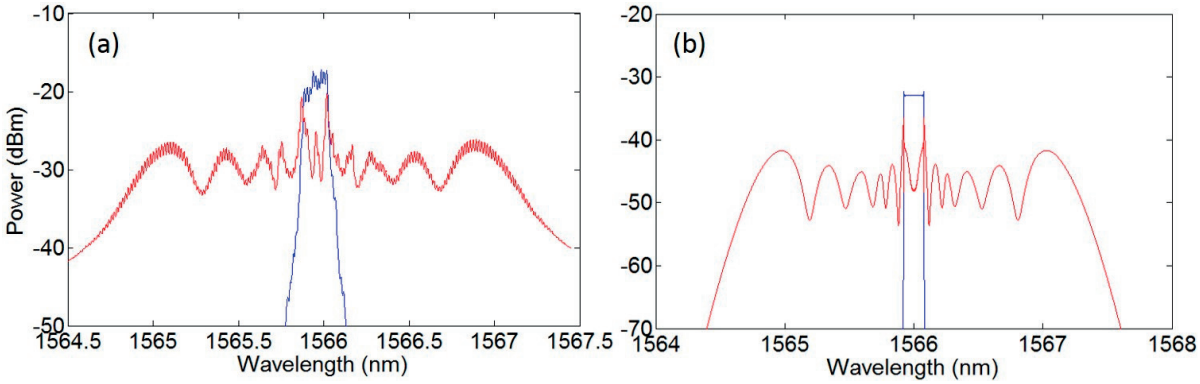

Figure 5.4: Spectrum of a 50 ps long pulse before (blue) and after (red) propagation in our 350 m long HNLF, recorded experimentally (a), and computed with an NLSE solver (b). The difference in power level is caused by the OSA power integration algorithm. The grooves in the experimental spectrum originate from the high rep-rate pulse sequence while the numerical spectrum considers a single pulse event.

5.2.2. Experimental results

From an experimental point of view, the pump pulse shaping relies on a dual-modulator scheme initially aimed at the generation of Nyquist pulses for time- and frequency-division multiplexed communications [5.10]. The basic version consists in processing a CW laser through two successive Mach–Zehnder modulators, one being driven at a frequency ν and the second one at a frequency 3ν. When a proper bias and RF power are applied to the modulators, a rectangular frequency comb of nine lines spanning 9ν is synthesized. Provided that the two RF sources are locked in phase, this rectangular spectrum corresponds in the time domain to a train of sinc-shaped pulses at a repetition rate of ν and peak-to-zero crossing time of $1/9\nu$. Such simple method allows for great flexibility: the repetition rate and the duty cycle can be modified easily by controlling the RF driving signals or by adding a third modulation stage. Moreover the laser wavelength can be adjusted to any value within the modulators operating range. Finally the whole setup solely relies on standard RF and fiber components, and is pictured in Fig 5.5(a). Following the numerical and experimental tests performed about pulse propagation in our HNLF, we used a 30 m segment from the previous fiber. Empirical FWM tests yield the CE curves shown in Fig. 5.5(b), for $\nu =$ 2 GHz and 1.7 W of average pump power (7 W peak) [5.11]. The CE is computed as the ratio between the idler "effective power" (pulse energy over pulse duration) and the signal CW power, both at the output of the HNLF. Counter-intuitively, it appears necessary to bring the pump closer to the ZDW (located at 1569 nm in average) to blue-shift the maximum CE. Dispersion fluctuations probably still play a role in this result, in contradiction with the theory from chapter 3. The CE peak at -15 dB) demonstrates that the increase in peak power compensates for the decrease in fiber length, compared to the CW case. Nonetheless and expectedly, we do observe a reduction of the tuning range at a given pump wavelength due to the shorter length of fiber and to the smaller amount of cumulated ZDW fluctuations.

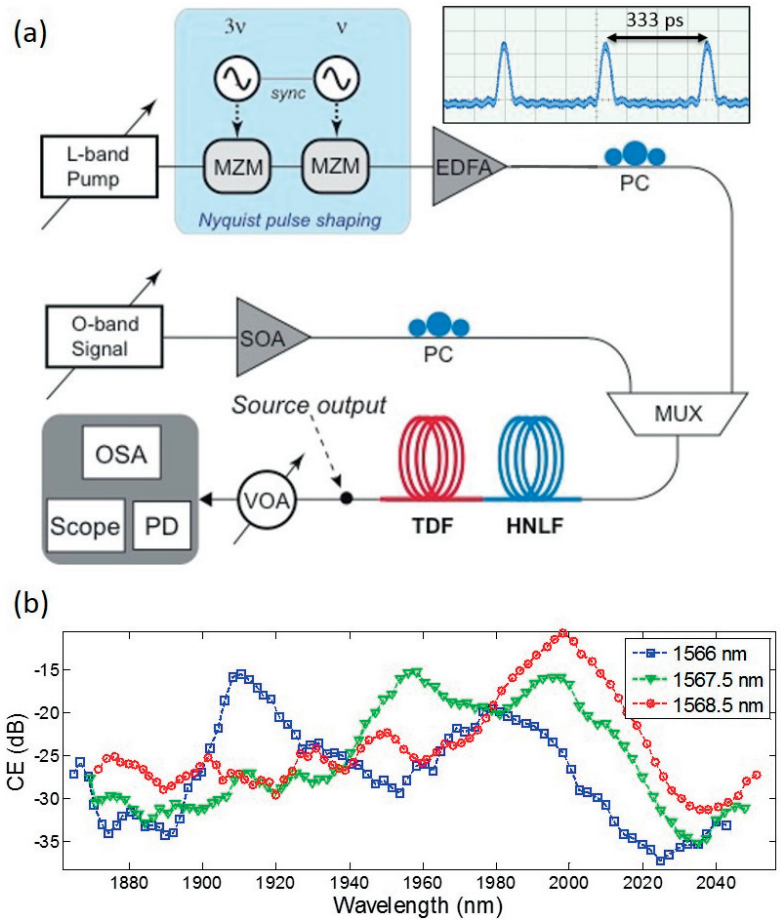

Figure 5.5: (a) Experimental setup for the pulsed pump FOPA-TDFA, with MZM: Mach-Zehnder modulator, VOA: variable optical attenuator. The HNLF is 30 m long and the TDF is either 11.5 m or 17.5 m long. (b) CE spectra as a function of the idler wavelength for various pump wavelengths, at a pump peak power of 7 W.

The FOPA-TDFA assembly was then characterized for two different output wavelengths: 1958 nm and 2001 nm. It can be seen from Fig. 5.5(b) that a pump set at 1567.5 nm is optimal in the first case, while 1568.5 nm is optimal in the second case. For an idler positioned at 1958 nm, an 11.5 m long TDF is appended at the HNLF output. The use of a relatively long doped fiber is necessary to red-shift the thulium gain peak toward 1958 nm and avoid detrimental effects such as parasitic lasing or OSNR degradation due to ASE. Nonetheless we have seen in the previous chapter that the pump was already depleted after 4.5 m of TDF, at an even higher average power. It means that part of the TDF will be pumped by the forward travelling ASE. This represents a good alternative to the dual-stage TDFA presented for the long-band SWIR amplification, since it avoids any insertion loss in fiber splices and WDMs.

Spectra and pulse waveforms recorded right after the TDF are shown in Fig. 5.6. The spectra before and after the TDF are plotted in Fig. 5.6(a). The repetition rate is 2 GHz and the pump peak power at the

HNLF input 1.7 W. The 1958 nm idler undergoes an amplification of 30 dB through the TDF while the L-band pump is entirely absorbed and the signal at 1310 nm strongly attenuated (-20 dB). No filter is used after the TDF to remove the ASE or select the wavelength. The adjustment of the thulium emission peak and a proper idler seed power are sufficient to guarantee a good OSNR (33 dB considering the peak to pedestal amplitude) at the desired wavelength after the amplifier. The noise visible on top of the peaks on the oscilloscope could be partly eliminated by using a bandpass filter after the TDF to remove the ASE. However, some noise originating from the FOPA is still present, and can be due to the C-band diode laser frequency jitter. It should be noted that the SWIR pulses are not sinc-shaped, primarily because there is a no linear dependence between the pump and idler waveforms.

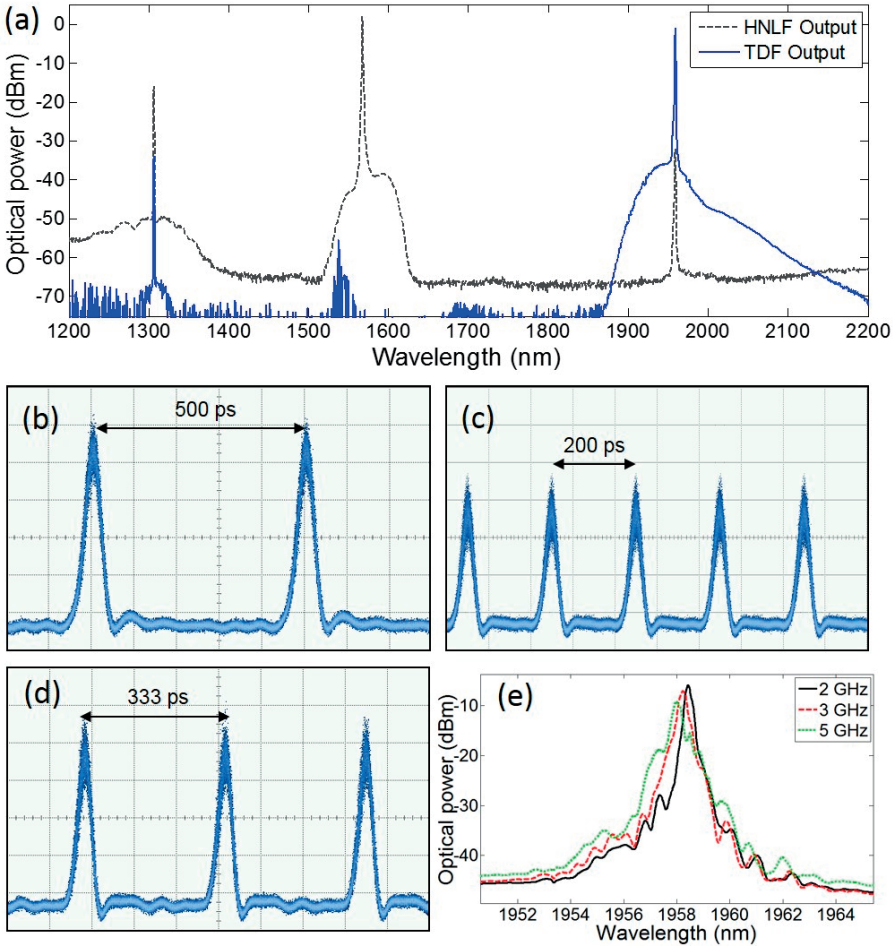

Figure 5.6: (a) Spectra at the output of the HNLF (black dotted line) and TDF (blue line) for the 1958 nm idler configuration. (b)-(d) Pulse train recorded at the TDF output for a repetition rate of (b) 2 GHz, (c) 3 GHz and (d) 5 GHz. (e) Idler spectra for various pump repetition rates, given in the legend.

The average SWIR output power in this configuration is measured to be 160 mW, independently of the repetition rate. From the oscilloscope traces, the pulse duration at half maximum for a repetition rate of 2,

3 and 5 GHz, is 45, 36 and 33 ps, respectively. However, except for the 2 GHz case, the pulse bandwidth exceeds that of the extended InGaAs fast photodiode (22 GHz). Consequently the pulse duration measurement for repetition rates higher than 2 GHz is likely to be limited by the photodiode impulse response. In the 2 GHz case, a pulse peak power of approximately 620 mW is retrieved. This value is expected to be of the same order of magnitude for all cases since the initial duty cycles are identical. Finally the idler spectra at the three rates are shown in Fig. 5.6(e) with, as expected, a slight broadening when ν is increased and consequently when the pump pulses are shortened. The amplified idler width is of the order of 1 nm at half maximum, which corresponds to 5 ps long pulses in the transform limited case. Since they are significantly longer, the idler broadening with the modulation speed is rather ascribed to the SPM undergone by the pump, which becomes more pronounced as the pulse rise and fall time are reduced. The spectral broadening is then transferred to the idler during its generation.

A similar characterization was performed for the generation of the 2001 nm idler. In this configuration, the pump was positioned at 1568.5 nm and a longer piece of TDF was used to further redshift the thulium gain peak. Nonetheless as the pumping power is limited and since the Tm^{3+} ions entail some absorption at 2 µm when they are not excited, a tradeoff must be found. A length of 17.5 m was selected as the best compromise in spite of the slight parasitic lasing around 1919 nm (see Fig. 5.7(a)). It should be noted that even if the CE peaks at −11 dB in this configuration, the O-band SOA is quite weak at the corresponding signal wavelength (1290 nm), and the subsequent idler power drop leads to a suboptimal TDFA seeding. We measure a 9 dB difference between the idler generated at 1958 nm and the 2001 nm one. Despite the 30 dB amplification in the TDFA, the OSNR is slightly degraded and a significant noise is added to the SWIR pulses, as can been seen in Fig. 5.7(b)-(d). When the repetition rate is increased to 5 GHz, bandpass filtering appears unavoidable to clean up the pulses from noise. Finally, in such configuration the output average power is 37 mW, for a pulse peak power of approximately 142 mW at 2 GHz, while the idler spectra features a similar broadening as in the 1958 nm case (see Fig. 5.7(e)).

In both cases presented, the CE curves shown in Fig. 5.5(b) demonstrate that the pulse central wavelength can be tuned over several nanometers around the peak values located at 1960 and 2000 nm, only by sweeping the O-band laser wavelength. For a larger output wavelength change, the pump and the TDF amplifier have to be reconfigured as well. Overall, the CE curves suggest that the source could operate between 1900 and 2000 nm seamlessly. Moreover, some Nyquist pulse shaping enhancements can be easily implemented and theoretically allow for a decoupled control of the pulse duration and repetition rate. On the one hand, it has been shown that seeding one of the modulators with two or more properly selected RF tones densifies the rectangular frequency comb while preserving its linewidth [5.10]. This translates into reducing the pump repetition rate while keeping the same pulse duration. On the other hand,

it is possible to keep the same line spacing and broaden the comb with a third modulator or via FWM in a HNLF [5.12]. This means that the pulse duration would be decreased at constant repetition rate. In both cases the pump peak power would increase after the EDFA, due to the reduced duty cycle. As a result the FWM efficiency would increase as well, enabling the use of a shorter HNLF. The main advantage of reducing the interaction length without sacrificing CE lies in the possibility to speed up the repetition rate (over 5 GHz) and/or reduce the pulse duration (below 30 ps). The adverse effects due to SPM and walk-off are circumvented when the fiber is kept short. From the applications side, reaching a repetition rate of 10 GHz or more would be attractive for 2 μm communication.

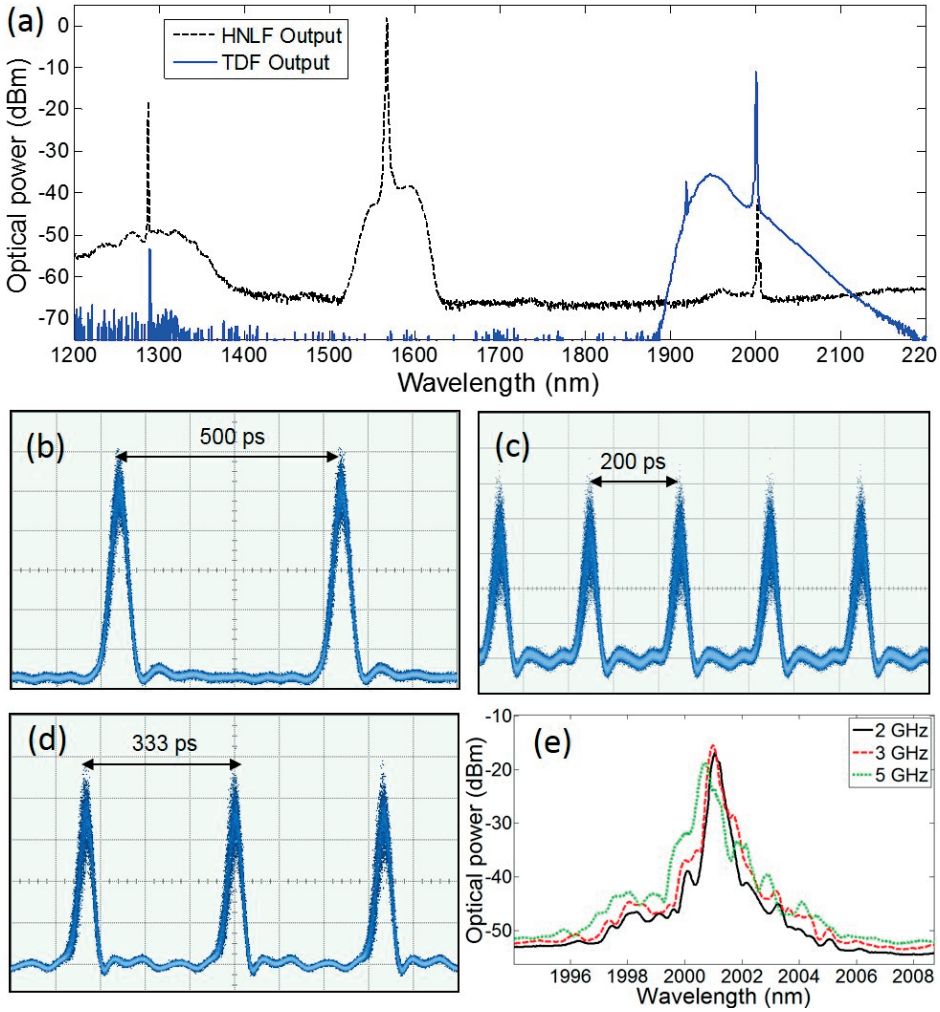

Figure 5.7: (a) Spectra at the output of the HNLF (black dotted line) and TDF (blue line) for the 2001 nm idler configuration. (b)-(d) Pulse train recorded at the TDF output for a repetition rate of (b) 2 GHz, (c) 3 GHz and (d) 5 GHz. (e) Idler spectra for various pump repetition rates, given in the legend.

5.3. Return-to-zero data transmission and wavelength multicast

As stated above, the ability to encode data on the pulse sequence generated in the FOPA-TDFA is of interest. Moreover the pulsed operation should address the shortcomings of the NRZ-OOK source presented above in terms of SBS suppression. For a single channel, it can be done straightforwardly by adding another intensity modulator on the pump path, which encodes data by gating the pulse sequence. We conducted an experiment to generate a wavelength tunable, high speed, RZ-OOK data stream at the source output. The data modulator is driven by a 2^{31}–1 PRBS and the experiment was conducted for a 3 Gbit/s bit rate, and a pump set at 1967.5 nm. Compared to pulse generation at the same repetition rate, the average duty cycle is reduced by a factor of two, given that half the bits are zeros. As the average pump power is kept identical to that of the previous experiment, the peak power is raised to approximately 14 W, which gives access to a slightly better CE in the FOPA stage. A significant fraction of the CE spectrum displayed in Fig. 5.5(b) for the 1567.5 nm case is therefore accessible, free of parasitic lasing in the TDFA stage. Thus the source is once again widely wavelength tunable, all the more since no filter is needed after the TDFA to obtain an error-free data projection thanks to an OSNR exceeding 25 dB. It is even necessary to attenuate its output power down to -7 dBm to make it compatible with telecom standards and prevent saturation or damaging the 2 μm photodetector. Fig 5.8(a) and (b) present eye patterns of the generated data train at two wavelengths far apart, namely 1940 nm and 1979 nm. Once again the eyes are wide open, and no phase-dithering periodically disturbs phase matching and scrambles bit replication. As a result, we achieve an error-free data projection all over the tested band, from 1930 nm to 1980 nm, as demonstrated in Fig. 5.8(c).

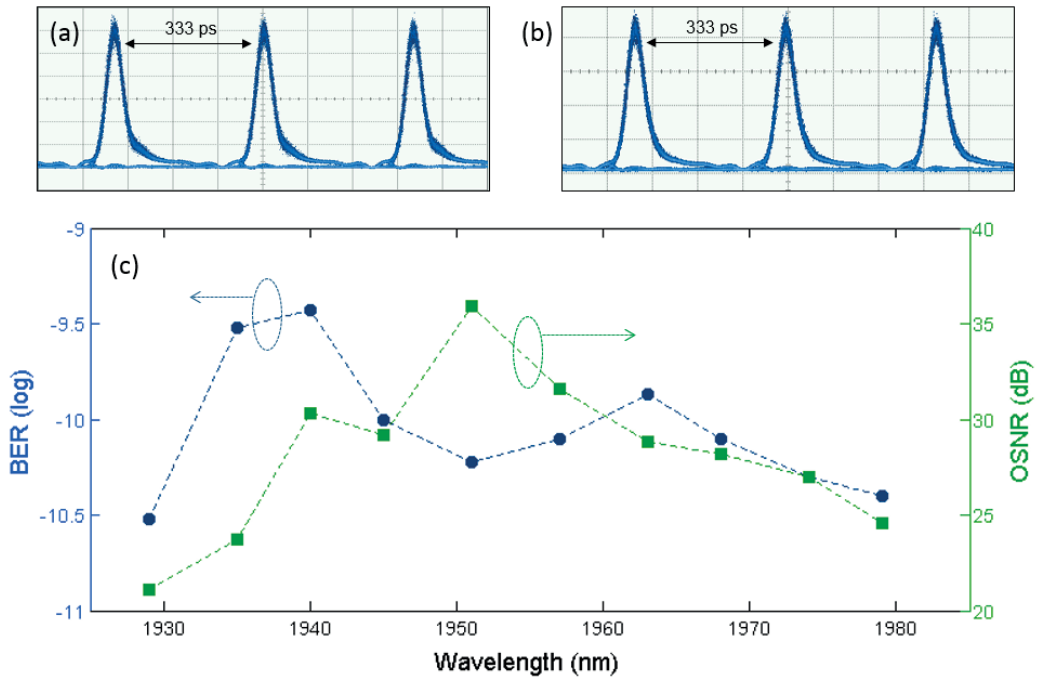

Figure 5.8: (a)-(b) Eye patterns of the RZ-OOK modulated idlers after the TDFA at (a) 1940 nm and (b) 1979 nm. (c) BER (circles, left axis) and OSNR (squares, right axis) recorded as a function of the idler wavelength at a bit rate of 3 Gbit/s.

On top of a tunable single channel data generator, the broad spectral slice available encouraged the simultaneous conversion of multiple channels. We already demonstrated the possibility to convert several signals in parallel in the CW regime without affecting the FOPA behavior, as a result of the low CE. It is therefore natural to think of wavelength multicasting over several channels, by injecting several CW O-band signals along with a RZ-OOK modulated pump. The data are consequently imprinted on several idlers in parallel, as described in Fig. 5.9(a). The experimental setup is described in Fig. 5.9(b), and features three O-band distributed feedback lasers that act as signal seeds. Unfortunately the lack of O-band sources and low-loss wavelength multiplexers renders the experiment difficult to scale with a larger number of channels. We especially had to use a single SOA for all channels in order to minimize the impact of coupling losses in the 50/50 power couplers upstream. The three idlers power after the FOPA-TDFA converter could be equalized by adjusting each channel's polarization with respect to the pump polarization in the HNLF. For this test, the pump bit rate was raised up to 5 Gbit/s.

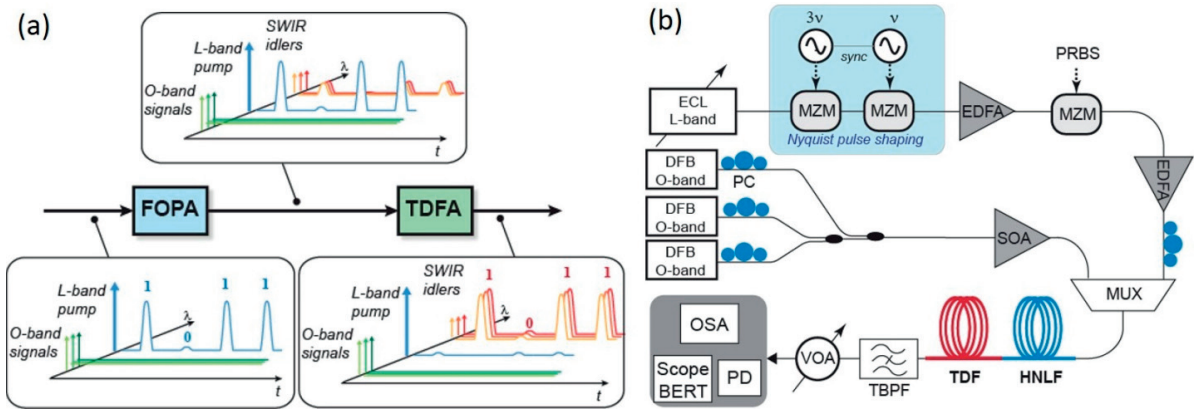

Figure 5.9: (a) Schematic principle of the multicasting operation. (b) Experimental setup with ECL: external cavity laser, DFB: distributed feedback semiconductor laser, PC: polarization controller, MUX: 1310/1550 nm wavelength multiplexer, TBPF: tunable band pass filter, VOA: variable optical attenuator, OSA: optical spectrum analyzer, PD: 2 µm, 22 GHz photodetector.

This simple setup enables the generation of three idlers with tens of milliwatts of power and all embedding error-free data and with an OSNR of 25 dB each [5.13]. A bandpass filter is inserted after the TDFA to select and analyze each channel. An error-free data projection is once again demonstrated for all of three channels. In this proof-of-concept experiment, idlers are located at 1947 nm, 1955 nm and 1968 nm, while the HNLF is once again pumped at 1567.5 nm. Since two of the O-band lasers out of three are fixed in wavelength, we could not test a configuration with denser channels, but the channel density should only be limited by the pump broadening processes described above, and the 2 µm filter bandwidth and rejection. Results obtained at the output of this source are shown in Fig. 5.10. It includes the output spectrum after the FOPA and after the TDFA, the eye pattern of each idler and their BER characterization. Wide open eyes are obtained, even though the pump ASE is not filtered after the EDFA, thanks to the large CE of -15 dB. The back-to-back measurement was performed on the pump before the HNLF, while the idlers BERs are recorded after the bandpass filter and an optical attenuator. Almost identical BERs are measured for the three multicast signals with an error free performance. The steep BER slope for all channels, including the back-to-back measurement, is ascribed to the low voltage at the output of the photodetector with respect to the error detector specifications. However, this fully demonstrates that an error-free wavelength multicasting is possible with this scheme, with very little penalty compared to the back-to-back case (only 1 dB at a BER of 10^{-9}).

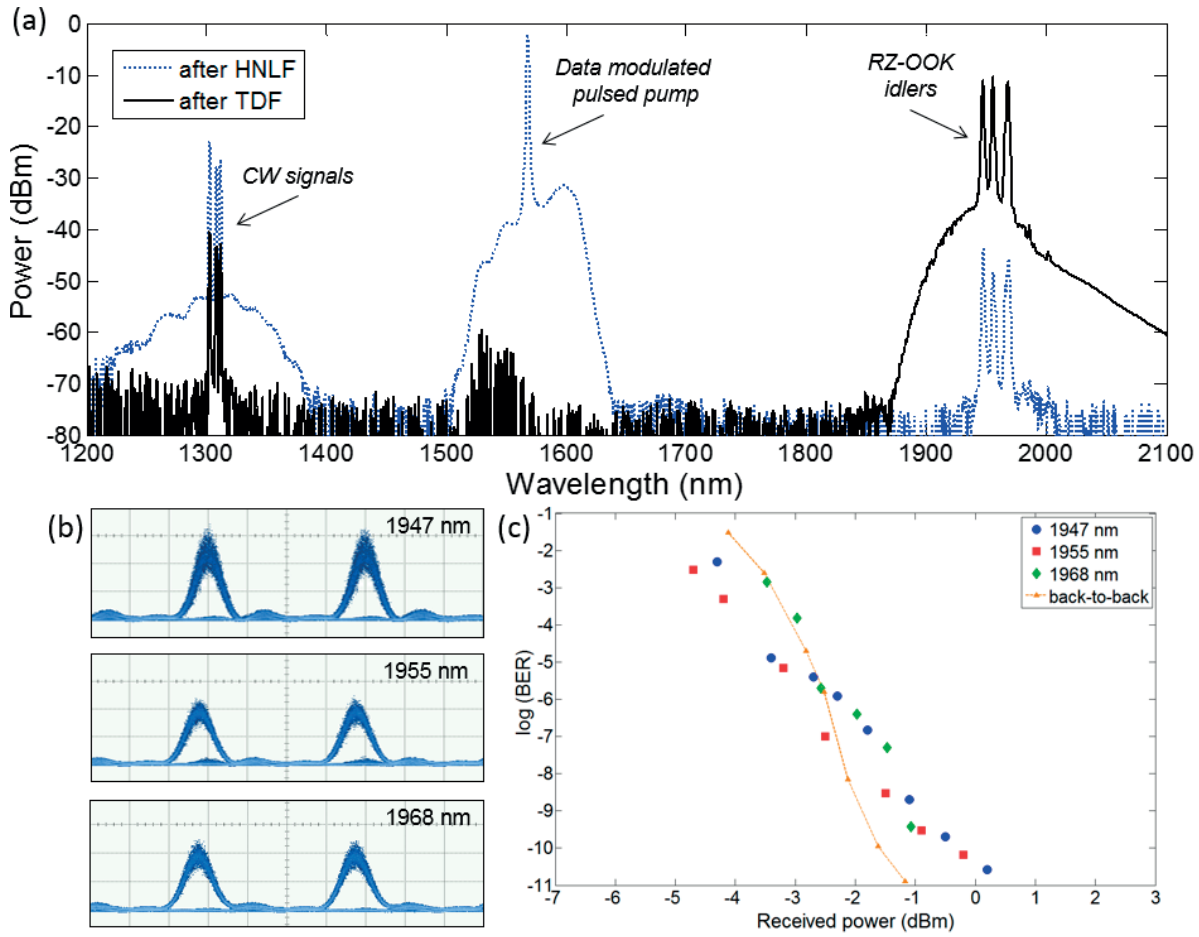

Figure 5.10: (a) Spectrum at the output of the HNLF (blue dashed line) and at the output of the TDF (black solid line). (b) Eye patternss (recorded on a 22 GHz detector) of the multicast channels at 1947 nm, 1955 nm and 1968 nm for an input power of 5 dBm. Time scale: 50 ps/div. (c) BER curves as a function of total integrated power of each channel at 5 Gbit/s.

As a possible improvement in order to embed different data sequences on each idler, we envision a combination of both setups presented in this chapter. Namely, a configuration that combines a pulsed pump that quenches Brillouin scattering, coupled with several independently NRZ-OOK modulated signals. With a proper synchronization of the pump and signals modulation, which must occur at the same fundamental frequency, it is conceivable to create a wavelength division multiplexed super-channel around 2 μm.

5.4. Pulsed source based on Raman cascade

This section is a parenthesis to briefly introduce a technology developed in parallel to the FOPA-TDFA during the MATISSE project. It is included here since it features many experimental similarities with the pulsed pump sources presented in section 5.2. First of all, it relies on the injection of Watt-level, pulsed

C-band pump into HNLF tens of meter long. The pulses are in the picosecond range, and the output consists of a wavelength tunable, SWIR pulse train. From a physics point of view, this design relies on cascaded Raman scattering. We have already seen that Raman scattering in silica generates a peak of fluorescence, detuned from the pump by approximately 13 THz in the near-infrared. Yet, this process can cascade to generate multiple peaks of emission, readily usable to make Raman amplifiers [5.14] and lasers [5.15]. The presented source uses the single pass Raman gain in HNLFs to generate three consecutive Stokes emission peaks, the last one being located near 2 µm. Two different experiments have been conducted and are described below. We focus on experimental results for the interplay between dispersion and Raman scattering in the picosecond regime has not been fully understood so far. Contrarily to the experiments described up to now, the pump is always located far from the ZDW in the normal dispersion regime. In doing so, parametric effects that require phase matching, namely FWM and MI, are significantly quenched. On the contrary, Raman scattering takes place whatever the dispersion, and is only limited by walk-off in pulsed regime. Finally, the peak power used for these experiments are 5 to 10 times higher than in the FOPAs, which explains why stimulated Raman scattering becomes so preponderant.

In the first setup [5.16], a pulse train is shaped with intensity modulators out of a 1566 nm CW diode laser. It features 43 ps long pulses at a 200 MHz repetition rate (visible in Fig. 5.11), which are then boosted into an EDFA at a power level between 0.5 and 5 W in average (50 to 500 W peak). They are then fed to a 500 m long segment of HNLF with the following properties: a ZDW at 1610 nm, a third order dispersion of $1.5 \cdot 10^{-2}$ ps^3/km and a nonlinear coefficient of 10 $W^{-1}km^{-1}$. Some spectra at the HNLF output, for 27 dBm (0.5 W) and 35 dBm (3.16 W) of booster power, are shown in Fig. 5.11(b). The average power at the top of each Stokes peak has also been measured for a range of pump average powers, and the results are presented in Fig. 5.11(c). The Stokes lobes power progressively grow and they finally merge into a supercontinuum. In Fig. 5.11(b), for 27 dBm of pump power the first two Stokes and the onset of the third Stoke lobe are clearly visible. The individual peaks are not distinguishable anymore at 35 dBm of pump power. It qualitatively shows how the power transfers from one peak to the next one, until they all reach saturation. No fourth Stokes peak was observed during the experiment, probably because of the SWIR attenuation is silica.

By inserting a tunable bandpass filter directly at the output of the HNLF, it is then possible to spectrally slice the third SWIR peak to obtain a wavelength tunable source of picosecond pulses, as shown in Fig. 5.11(d). It pictures the narrow-band filtered spectra, which span a range from 1820 nm to 2050 nm, and their equivalent in a time domain (recorded with a 9 GHz SWIR photodetector). The relatively low level of noise observed on top of the pulse envelope tends to indicate a relatively coherent conversion process, with low pulse-to-pulse intensity variations or time jitter [5.17].

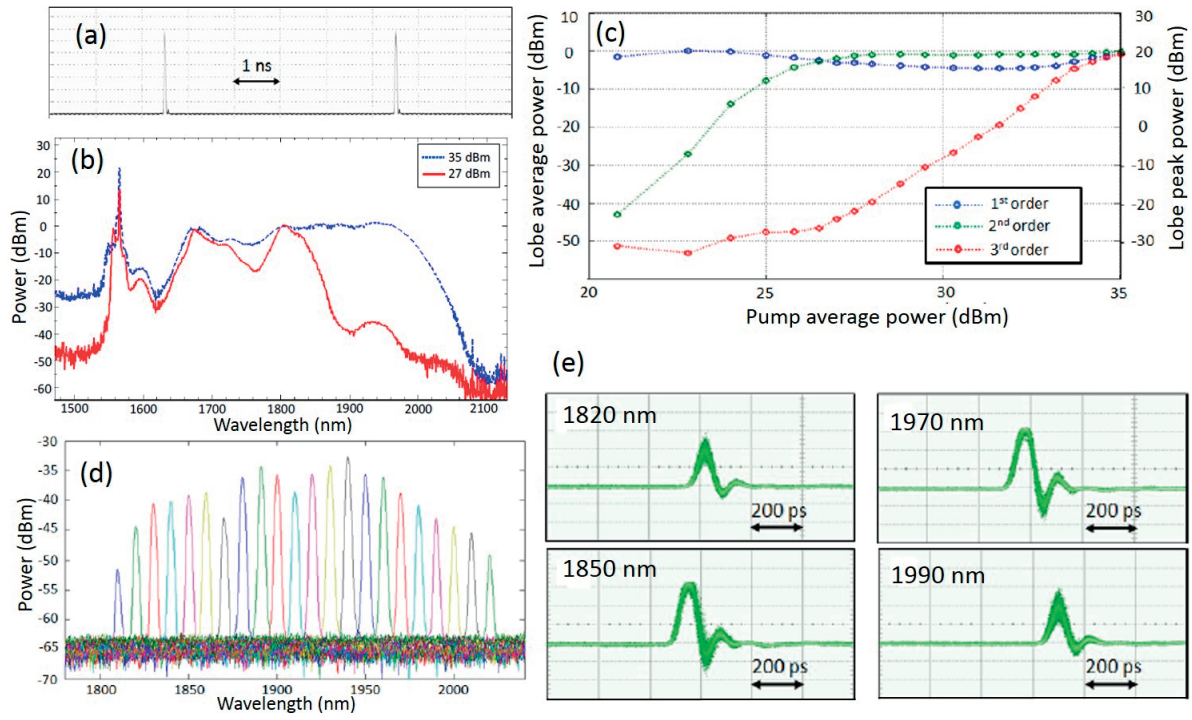

Figure 5.11: (a) Input pulse pump train at 1566 nm observed on a 500 GHz optical sampling oscilloscope. (b) Spectrum at the output of the HNLF for an average pumping power of 27 dBm (solid red line) and of 35 dBm (blue dashed line). (c) Average power (left axis) and estimated peak power (right vertical axis) at the maximum of each Stokes lobe as a function of the average pump power. (d) Superimposed spectra of the filtered 3rd Stokes lobe and (d) some corresponding waveforms detected on a 9 GHz photodiode, of which impulse response function is clearly visible.

The second setup [5.18] involves another pulse train, centered at 1570 nm. This time, 9.8 ps long, sinc-shaped pulses are injected in the HNLF at a repetition rate of 500 MHz. Beforehand, the pulses are amplified directly up to 3.5 W average. The fiber is only 50 m long and features the following properties: a ZDW at 1605 nm, a third-order dispersion of $1.5 \cdot 10^{-2}$ ps^3/km and a nonlinear coefficient of 14 $W^{-1}km^{-1}$. In this experiment, the SPM undergone by the Raman lobes make them merge into a supercontinuum, and the threefold cascade is less observable than in the previous experiment. As a side effect, FWM broadens the continuum on the short-wavelength side by replicating the Stokes components. The spectrum at the HNLF output can be seen in Fig. 5.12(a). Similarly to FOPA-TDFAs, we used a 4.5 m piece of TDF after the HNLF to recycle the remaining pump power and transfer it to the third Stokes peak. The spectrum after the TDF is also shown in Fig. 5.12(a) and proves the entire pump depletion. Some power subsists around the O-band and is originally due to parametric replication of the Raman fluorescence. The broad emission peak obtained after the TDF contains a power of 1.5 W average, and can again be spectrally sliced to obtain a tunable pulsed source. The results are plotted in Fig. 5.12(b)-(c). Once again, little noise is observed on top of the pulses. We performed preliminary studies of the broad TDF output, spanning

from 1850 nm to 1950 nm, and the latter seems to be coherent. A second-order autocorrelation measurement yields traces within the femtosecond regime, but the subject is still under investigation. Nonetheless, since this kind of source requires high peak powers in the picosecond regime, they are necessarily limited in terms of repetition rate. Pumping the fibers in the femtosecond regime would entail a totally different kind of broadening, where parametric effects overwhelm the contribution of Raman scattering [5.19].

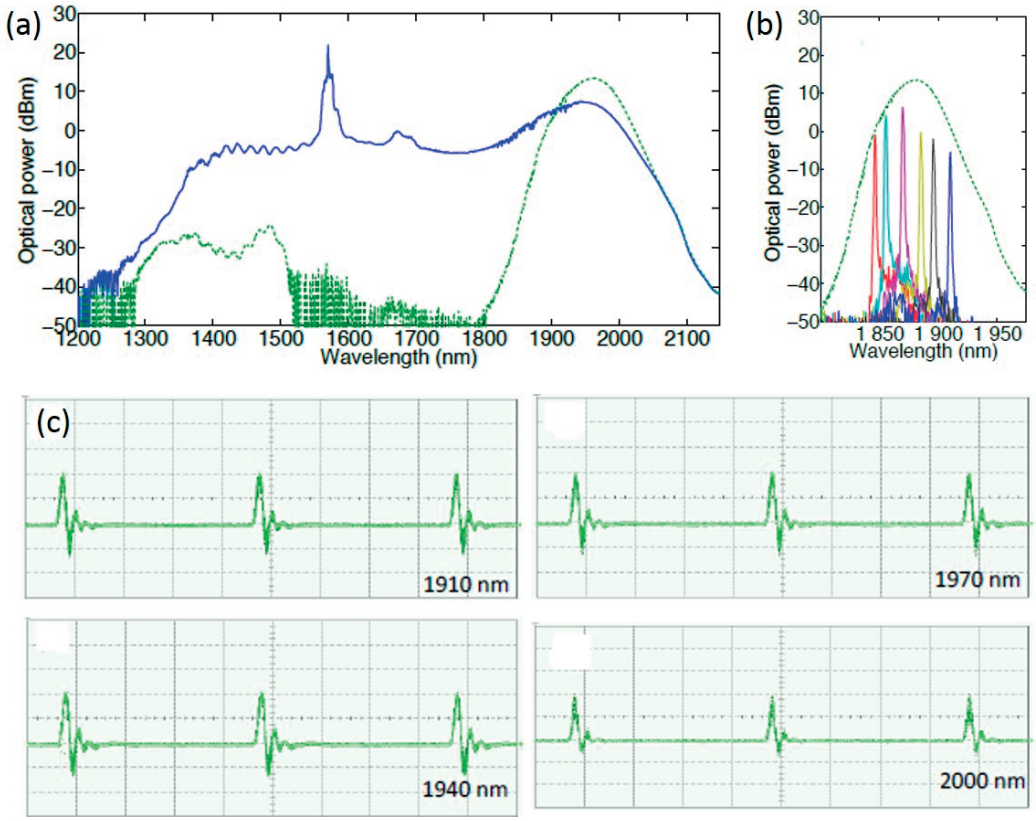

Figure 5.12: (a) Spectrum at the output of the HNLF (blue line) and of the TDFA (green dashed line) for an average pumping power of 35 dBm. (b) Superimposed spectra of the entire SWIR source output (green dashed line) and of filtered slices (plain lines). (c) Waveforms of the filtered output at several wavelengths, as recorded on a 9 GHz SWIR photodetector.

5.5. References

[5.1] F. Gholami et al., "10Gbps Parametric Short-Wave Infrared Transmitter," Proc. OFC, OthC6, Los Angeles (2011).

[5.2] F. Gholami et al., "Phase-preserving parametric wavelength conversion to SWIR band in highly nonlinear dispersion stabilized fiber," Opt. Express 21, 11415-11424 (2013).

[5.3] S. Cordette et al., "Tunable Thulium-Assisted Parametric Generation of 10 Gb/s Intensity Modulated Signals Near 2 μm," in Optical Communication (ECOC 2014), 40th European Conference and Exhibition on (Cannes, 2014), paper P.1.12.

[5.4] S. Moro et al., "Phase noise in fiber-optic parametric amplifiers and converters and its impact on sensing and communication systems," Opt. Express 18, 21449-21460 (2010).

[5.5] P. L. Voss et al., "Raman-noise-induced noise-figure limit for $\chi^{(3)}$ parametric amplifiers," Opt. Lett. 29, 445-447 (2004).

[5.6] A. Mussot et al., "Impact of pump phase modulation on the gain of fiber optical parametric amplifier," IEEE Photon. Technol. Lett. 16, 1289–1291 (2004).

[5.7] M. E. Marhic, *Fiber optical parametric amplifiers, oscillators and related devices*. Cambridge University Press, 2008.

[5.8] T. Hirooka et al., "Linear and nonlinear propagation of optical Nyquist pulses in fibers," Opt. Express 20, 19836-19849 (2012)

[5.9] R. H. Stolen et al., "Self-phase-modulation in silica optical fibers," Phys. Rev. A 17, 1448–1453 (1978).

[5.10] M. A. Soto et al., "Optical sinc-shaped Nyquist pulses of exceptional quality," Nat. Commun. 4, 2898 (2013).

[5.11] A. Billat et al., "Versatile High Repetition Rate 2-μm Pulsed Source Based on Wideband Parametric Conversion," J. Lightwave Technol. 34, 879-884 (2016).

[5.12] S. Cordette et al., "Bandwidth and repetition rate programmable Nyquist sinc-shaped pulse train source based on intensity modulators and four-wave mixing," Opt. Lett. 39, 6668-6671 (2014).

[5.13] A. Billat et al., "Wavelength Multicasting and Amplification of 5 Gb/s Data in the 2 Micron Band," in *Optical Fiber Communication Conference*, OSA Technical Digest (online) (Optical Society of America, 2016), paper Th2A.4

[5.14] V. R. Supradeepa et al., "A high efficiency architecture for cascaded Raman fiber lasers," Opt. Express 21, 7148-7155 (2013).

[5.15] E. M. Dianov et al., "Raman fibre lasers emitting at a wavelength above 2 μm," Quantum Electron. 34(8), 695–697 (2004).

[5.16] S. Cordette et al., "Widely tunable picosecond-pulsed source near 2 μm based on cascaded Raman wavelength shifting," 2014 The European Conference on Optical Communication (ECOC), Cannes, 2014, pp. 1-3.

[5.17] M. Nakazawa et al., "Coherence degradation in the process of supercontinuum generation in an optical fiber," Opt. Fiber Technol. 4, 215-223 (1998).

[5.18] S. Cordette et al., "High Power Sub-Picosecond Pulsed SWIR Source Based on Thulium Assisted Raman Wavelength Shifting," in Optical Fiber Communication Conference, OSA Technical Digest (online) (Optical Society of America, 2015), paper Tu2C.4.

[5.19] J. M. Dudley et al., "Supercontinuum generation in photonic crystal fiber," Rev. Mod. Phys. 78, 1135–1184 (2006).

Chapter 6 Platforms for conversion towards the mid-infrared

This chapter presents preliminary results obtained in waveguides targeted towards the MIR conversion stage, pumped by the previously described FOPA-TDFA. We identified the most promising platforms for this purpose to be silicon-on-insulator (SOI) waveguides, buried silicon nitride (SiN) waveguides and microstructured chalcogenide fibers. The primary reason for this choice is because all of them are made of materials transparent in MIR. Moreover, they all feature a high nonlinear index, and their fabrication is very versatile, such that the final waveguide dispersion can be tailored. The first section describes the work performed towards the fabrication of SOI waveguides, as well as their shortcomings and the reasons why they have not been retained for the project. Afterward we present some SiN waveguide characterization results, which show interesting abilities for dispersive wave generation bur are not yetoptimal for FWM in MIR. The third part introduces chalcogenide fibers and their preliminary characterizations, obtained with a SWIR parametric pump. The results obtained with these fibers are very promising and encouraged us to pursue our work in this direction.

6.1. Silicon-on-insulator ridge waveguides

Due to its very broad transmission window, extremely large nonlinear refractive index ($n_2 \sim 10^{-17}$ m^2W^{-1}, a thousand times more than silica) [6.1][6.2] and the availably and precision of CMOS fabrication methods in standard cleanrooms, silicon has long been seen as a promising platform for nonlinear integrated optics [6.3]. Moreover, crystalline silicon is a very well characterized and documented material, of which properties vary little from sample to sample. This fact does help in the waveguide design procedure. Focusing specifically on parametric conversion from telecom bands to MIR, the most recent and convincing results were obtained with silicon ridge waveguides (also called nanowires) on an insulator substrate made of silica or sapphire [6.4] [6.5]. The former tends to strongly absorb at wavelengths longer than 4 µm, while the latter exhibits very low infrared absorption. Nonetheless thin film silicon-on-sapphire wafers are uneasy to find off-the-shelf [6.6]. We opted for standard SOI wafers (silicon-on-thermal silicon oxide) due to their availability, and planned to fabricate the waveguides at the EPFL Center of Micronanotechnology. The goal was to fabricate these unclad ridge waveguides, of which typical dimensions are the following: some hundreds of nanometers in height and about a micron in width. It is interesting to terminate the waveguide by inverse tapers that act as spot size converters on both ends, in order to ease light coupling with a lensed fiber or a microscope objective [6.7]. A schematic representation of such a chip and of the end-fire coupling with a fiber is shown in Fig. 6.1(a).

With the help of a finite-element solver, we computed the group velocity dispersion (GVD) of a 340 nm x 1400 nm waveguide using standard Sellmeier coefficients for Si [6.8] (see Fig. 6.1(d)). These dimensions appear suitable for parametric conversion in the SWIR, as the ZDW lies near 2.16 µm. Some CE spectra computed with the analytical model from chapter 2 are shown in Fig. 6.1(c), for a waveguide length of 1 cm. They are calculated in case a 1 W CW pump is swept over the 2000 – 2120 nm range. Both the dispersion and CE values hold for the fundamental transverse electric (TE, the electric field is parallel to the substrate plane) mode, as this structure is multimode in SWIR and highly birefringent. Very importantly, the large refractive index of silicon in MIR ($n > 3.4$) entails a strong MIR light confinement, as demonstrated by the simulated mode profile at 2050 and 4000 nm (see Fig. 6.1(b)). This is at the same time advantageous to increase γ, to reduce the cladding absorption and to prevent excessive bend losses in case the waveguide is folded on the chip.

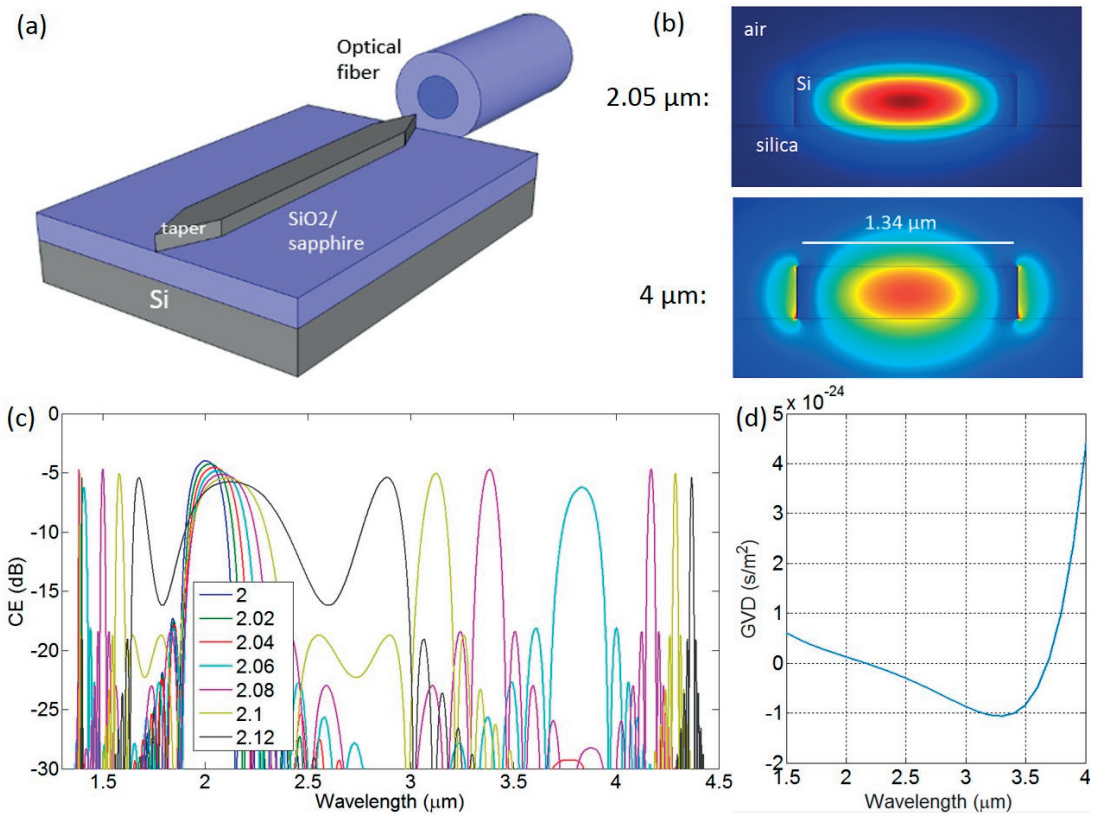

Figure 6.1: (a) Schematic view of the SOI ridge waveguide, with the optical fiber used for end-fire coupling figured in the back. (b) Fundamental TE mode profile at a wavelength of 2050 and 4000 nm in a waveguide featuring a thickness of 340 nm and a width of 1400 nm. (c) Simulated CE spectra in the 1 cm long waveguide described before, when pumped in SWIR by a 1 W laser in the TE fundamental mode. The pump wavelengths are given in µm in the legend. (d) Simulated near-infrared and MIR group velocity dispersion curve. The ZDW is located near 2160 nm

To fabricate such an SOI nanowire, we had to design and implement a process flow consisting of the steps described in Fig. 6.2. The process is only subtractive and does not involve any material deposition, since SOI wafers with very thin top Si layers are commercially available. The wafers we used are made of a 340 nm silicon film on top of a 2 µm buried oxide layer, while the silicon substrate is about 700 micron thick. To transfer the waveguide layout onto the wafer, electron beam lithography had to be used in order to reach the sub-micron resolution necessary here. Hydrogen silsesquioxane (HSQ), a negative resist (i.e. the exposed resist becomes insensitive to the developing solvent), is used to reduce the exposed surface to the strict minimum and keep the exposure time as short as possible. After development, conventional reactive ion etching (RIE) with an SF_6 and C_4F_8 gas mixture is used to remove entirely the unprotected silicon layer. Issues related to waveguide wall roughness can arise during this step. SF_6-based anisotropic etching entails some roughness due to a chemical attack of the waveguide sides. More elaborated etch processes are considered in the literature [6.9], nonetheless their implementation from scratch in reactors is very time consuming. Since nanowires wall roughness mostly results in light scattering [6.10], we chose to tolerate some increased propagation losses. After etching, the hardened HSQ must be removed with hydrofluoric acid (HF) since it has a chemical composition similar to silica. This step is necessary to prevent the top HSQ layer from perturbing the waveguide dispersion. It is a critical stage as HF also dissolves the silica substrate and under-etches the nanowire. If precautions are not taken the waveguide is mechanically weakened, up to a point where it breaks away from the substrate, especially in the tapered region. Finally, a mesa must be defined around the waveguide to allow for end-fire coupling. The distance between the tapers tips and the mesa edge therefore has to be as short as possible, no more than the working distance of the lensed fiber (some tens of microns). The mesa pattern is defined by photolithography, before we etch through the silica layer with a C_4F_8 based mixture, and then deeply into the silicon substrate thanks to a Bosch process [6.11].

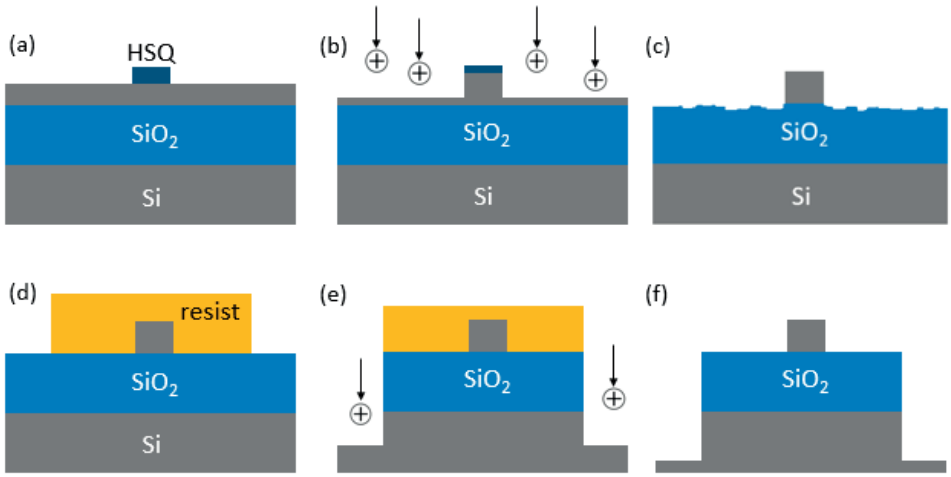

Figure 6.2: Simplified process flow for the fabrication of the SOI nanowires. It includes the following steps: (a) resist electron beam-patterning and development for the waveguide definition; (b) reactive ion etching to shape the waveguides in the Si top layer; (c) resist stripping in hydrofluoric acid, showing the silica layer attack; (d) photolithography patterning and development of the resist for the mesa definition; (e) reactive ion etching through the oxide layer and deep into the substrate; (f) resist stripping and final chip cleaning.

Some scanning electron microscope (SEM) pictures of the waveguides after fabrication are shown in Fig. 6.3. They exhibit a visually acceptable wall roughness and taper tip quality. However, many problems arose during the fabrication of unclad waveguides. The complexity of HSQ stripping was mentioned earlier, but in addition to this the photoresist tends to burn during the long Bosch process. This reaction lasts for several tens of minutes while heat accumulates in the sample. This problem can be handled to some extent by promoting heat conduction from the wafer to the reactor chuck, nevertheless we could not achieve a perfect cleaning of the waveguides after this step. With taper tips and cross sections that small, resist residues cause coupling and propagation losses far beyond what can be tolerated for nonlinear applications. Facet damage or waveguide fusion are to be expected for samples illuminated by Watt-level infrared lasers and contaminated with organic compounds. On top of this, two-photon absorption — still present at 2 µm [6.12] — and free-carrier absorption [6.13] reduce the potential of silicon. The sensitivity of unclad chips against aging and environmental conditions is also an issue. All of these shortcomings, plus those encountered during fabrication, led us to consider different integrated designs. As an alternative option, we tested silicon nitride waveguides clad in SiO_2.

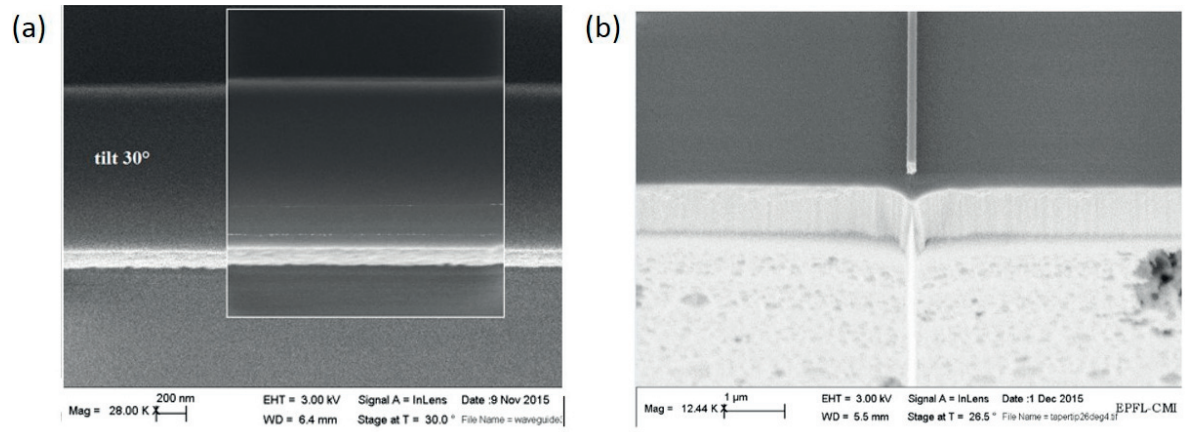

Figure 6.3: Scanning electron micrographs of (a) the tilted waveguide after the HSQ strip step. The image part in the rectangle corresponds to an averaged picture with an enhanced resolution, while the apparent waveguide offset has no physical reality. (b) Facet picture with the inverse taper tip reaching the mesa edge, after the final cleaning step. Striation, typical after a Bosch process, is visible on the substrate facet.

6.2. Silicon nitride buried waveguides

Silicon nitride (Si_3N_4 in its stoichiometric form) is a wide bandgap amorphous material. Consequently, it is free of flaws related to multi-photon absorption or free carrier absorption [6.14]. In the frame of a collaboration with the EPFL Laboratory of Photonics and Quantum measurement, we could characterize waveguides fabricated with the same technology as record-breaking microresonators [6.15]. The samples at our disposal are made according to the photonic Damascene process [6.16], schematically sketched in Fig. 6.4(a). Trenches are first etched in a silica layer, and low-pressure chemical vapor deposition SiN is then deposited onto the wafer. Such a deposition process, which fills up the trenches to define waveguides, protects the SiN layer from cracking. Afterward, the excess of SiN is removed thanks to a chemical-mechanical polishing of the wafer frontside. A low-temperature oxide (similar to silica) is finally deposited on top of it to obtain high quality buried waveguides, of which cross-section is depicted in Fig. 6.4(b). The waveguides are folded in meanders on 5 x 5 mm chips and can be as long as 4 cm.

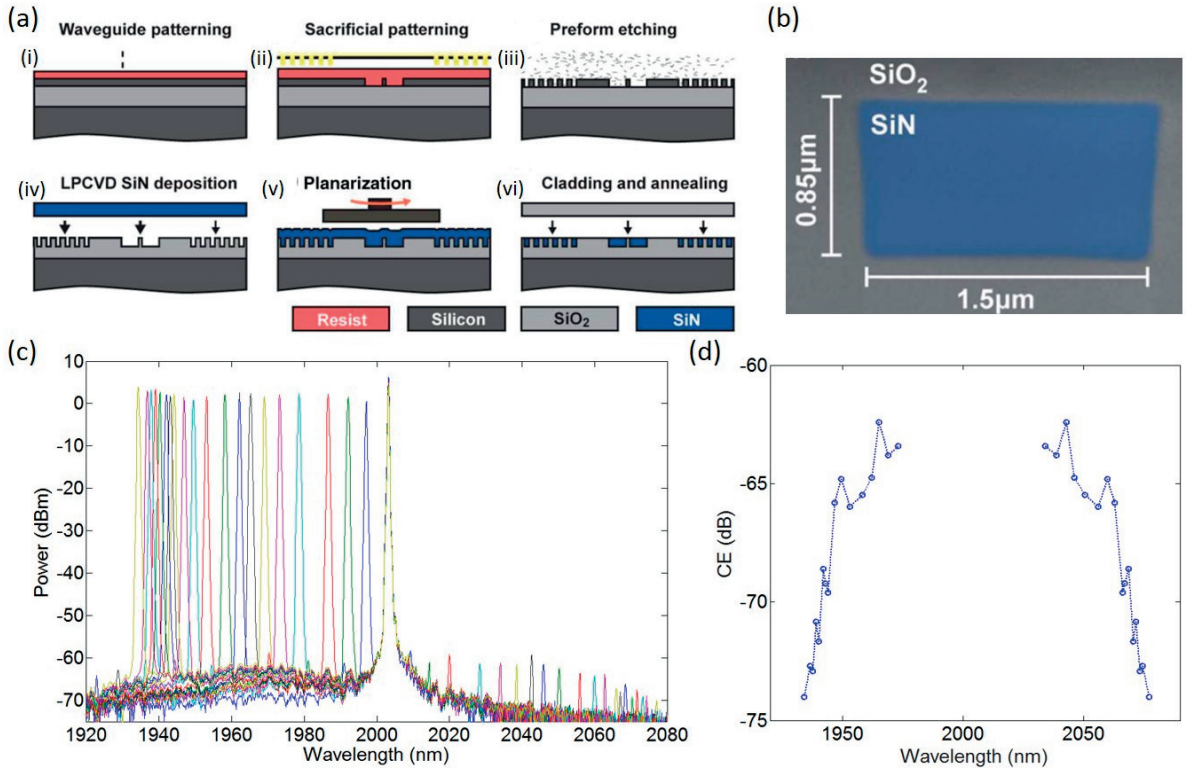

Figure 6.4: (a) Schematic process flow used to fabricate the waveguides. The steps order is given by the latin numbers in parentheses. (b) Electron microscope image of a waveguide cross section obtained with the Damascene process flow. The dimensions are arbitrary, but are similar to that of the waveguides we used. Adapted from [6.16]. (c) FWM spectra at the output of a 4 cm long SiN waveguide having the following cross section: 0.87 x 1.7 um, pumped in the TE mode by a 93 mW pump at 2003 nm. (d) Associated conversion efficiency.

The nonlinear capabilities of the waveguides at 2 µm are then probed with FWM, with a protocol identical to that used for the TDF in chapter 4. Two thulium-doped fiber lasers, one fixed in wavelength and the other tunable, are combined with a power coupler and then injected into the waveguide with the help of a lensed fiber. Another lensed fiber collects the power at the output facet and directs it towards an OSA. We estimate the in- and out-coupling losses to amount to 3 dB, while the propagation losses we recorded are of the order 0.2 dB/cm. The waveguide that we probed was 4 cm long, and its cross section has the following dimensions: 0.87 µm in thickness and 1.7 µm in width. The pump is centered at 2003 nm and the CW power coupled onto the TE mode was 93 mW. The signal is then swept from 1930 nm to 2000 nm, which yields the FWM spectra presented in Fig. 6.4(c). The associated experimental conversion efficiency is shown in Fig. 6.4(d). According to our finite-element mode solver, this waveguide has a ZDW near 2.17 µm for the fundamental TE mode. Thus, we pumped the waveguide deeply in the anomalous regime, and simulations indicate that distant CE lobes eventually exist in MIR. However the experimental CE magnitude (-60 dB at most), also in agreement with simulations, is too low for practical purposes. Even though SiN waveguides can feature nonlinear coefficients of the order of 1 $W^{-1}m^{-1}$ (while

$n_2 \sim 10^{-19}$ m^2W^{-1} [6.14]), this is not sufficient to compensate for the short interaction length compared to fibers, especially considering the relatively low pumping powers permitted by the on-chip coupling. We will see in the next section that chalcogenide fibers offer such high nonlinearity over much longer interaction distances.

While the short effective length of the available waveguides hindered their potential for single-pass FWM in CW regime in the thulium band, they still possess other qualities that render them highly suitable for alternative types of parametric conversion, in particular dispersive-wave based MIR light generation. When a pulse propagates in a waveguide featuring an anomalous dispersion, a stable solution of the NLSE presented in chapter 2 exists. The pulse envelope corresponding to this solution is called a soliton. Nevertheless, when dispersion terms of order higher than 2 are taken into account, this pulse is not stable anymore along propagation, and part of its energy transfers into a temporally spreading background (in the time domain). Such a phenomenon is called dispersive wave generation. Spectrally speaking, the dispersive wave appears where some phase matching constraint is respected [6.18]. Neglecting the SPM undergone by the pump, this constraint is given by Eq. 6.1.

$$\beta_{int}(\omega) = \beta(\omega) - \beta(\omega_p) - \beta_1(\omega_p) \cdot (\omega - \omega_p) = 0 \tag{6.1}$$

In this equation, β_{int} is the integrated dispersion, ω_p is the pump central frequency, while the β terms correspond to the dispersion orders, such as defined previously. Here again, given the frequency detuning at play (as verified experimentally on the spectra below), the waveguide dispersion is predominant and neglecting SPM is a fair approximation. In the frame of the MATISSE project, we investigated the outcome of SiN waveguide pumping by a femtosecond erbium-doped fiber laser [6.17].

The tested waveguides were similar to those used for FWM, excepted that they are straight and only 5 mm long. They are all 0.87 µm thick, but their width is varied from 1.3 to 1.7 µm. Fig. 6.5(a) presents the theoretical integrated dispersion curves computed for all these waveguides, for the fundamental TE mode. The zero-crossings corresponding to points where the dispersive is phase-matched with the pump. As seen on this figure, two dispersive waves, one in the visible and one in MIR, are expected at the waveguide output. Moreover, varying the waveguide width should allow for the control of the generated MIR wave position over the 2.6 — 3.6 µm range, while the visible one is fixed near 600 nm. The laser used is an amplified ELMO by Menlo Systems, and the pulse train we coupled in the waveguide onto the TE polarization has the following properties: 130 fs long Gaussian pulses at a 100 MHz repetition rate. The pump spectrum is centered at 1550 nm and the peak power reaches 4.2 kW. All this corresponds to a pulse energy of about 0.6 nJ. When the laser is injected in the 1.7 µm wide waveguide, a strong green/yellow light was scattered out of the chip, as seen in Fig. 6.5(b). The output spectrum, recorded partly with a grating OSA for the visible and near-infrared part, and with a Fourier-transform OSA for the MIR part,

indeed features two dispersive waves at the expected wavelengths (see Fig. 6.5(c)). One is located around 560 nm and explains the visible chip glow, while the other one is generated as deep in MIR as 3.5 µm. The total power collected at the chip output is 16 mW.

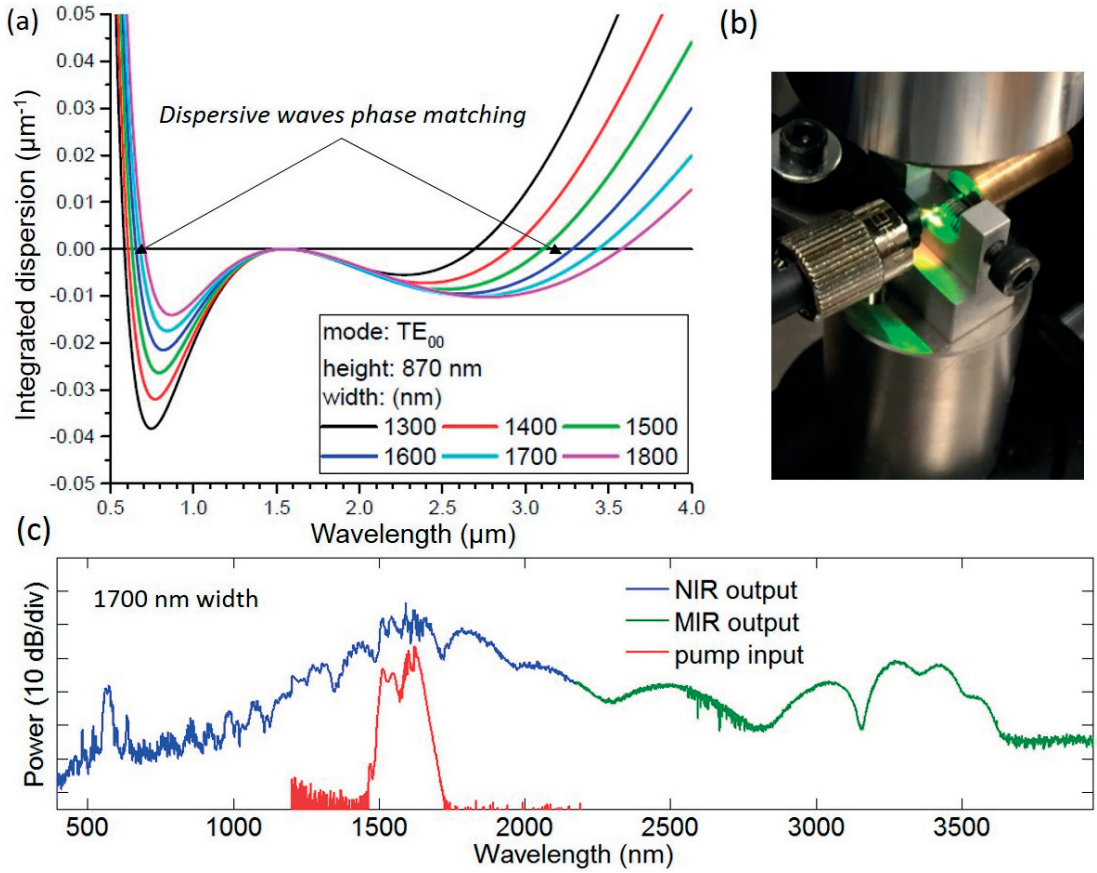

Figure 6.5: (a) Integrated dispersion curves for several SiN waveguide dimensions, given in the legend. The zero-crossing points indicate where the dispersive wave is phase-matched with the pump. (b) Picture of the dispersive wave generation setup in operation. The laser is injected from the right lensed fiber, and green-yellow light from the anti-Stokes dispersive wave is clearly visible. The output is collected by butt-coupling a multimode ZBLAN fiber on the left. (c) Supercontinuum generation, from the visible to the MIR, in the SiN waveguide pumped by a kW-level, femtosecond laser at 1.55 µm.

The dispersive wave generation behavior was further validated by injecting the laser in the 1.3, 1.4, 1.5 and 1.6 µm wide waveguides, still on the TE polarization. As seen in Fig. 6.7, the MIR dispersive wave position in each case agrees well with the integrated dispersion shown above. This parametric effect is therefore a straightforward way to generate pulsed MIR light from a compact and CMOS-compatible waveguide pumped by a communication band laser. However the output wavelength is defined by waveguide design, and the source properties are strongly constrained by the pulse requirements to obtain this soliton-related effect. Namely, the pulse duration should remain in the 100 fs order or below, and its

energy must be sufficiently high to trigger the dispersive wave generation. As such, it appears complicated to use a more compact source than the low repetition rate, mode-locked fiber laser employed here.

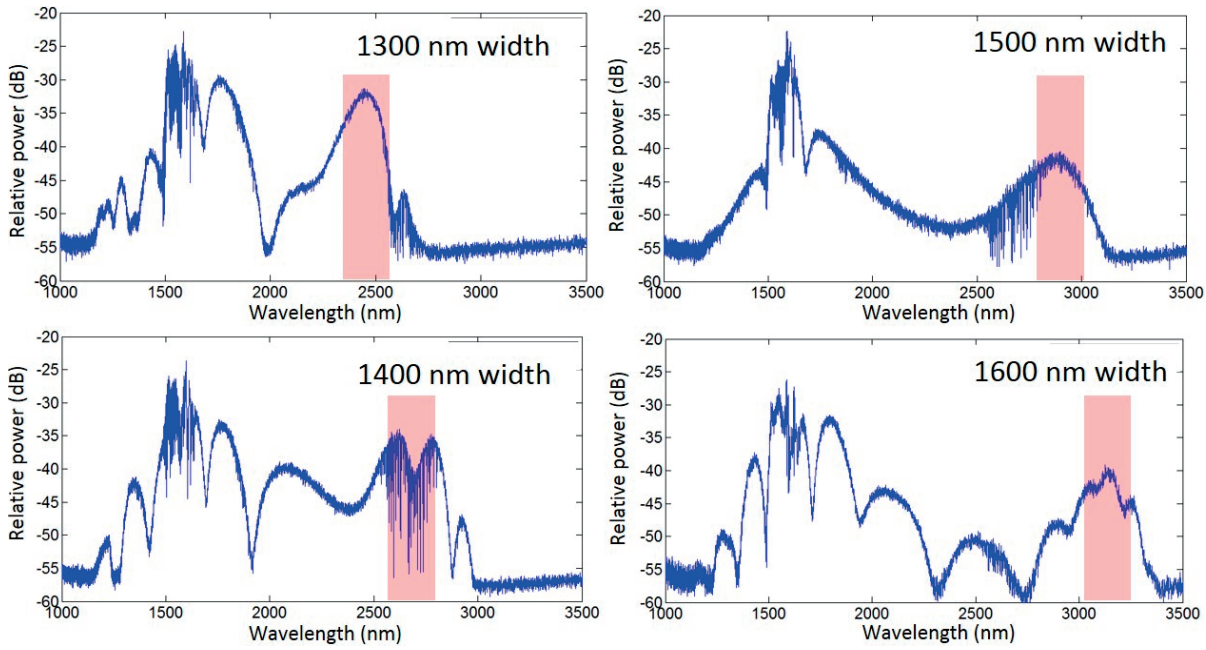

Figure 6.6: MIR dispersive wave spectra for various waveguide widths indicated in the figure legends. The pumping conditions are similar to that of Fig. 6.5(c).

6.3. Chalcogenide microstructured fibers

Chalcogenide glasses constitute a class of amorphous material containing one or more chalcogen element, which are sulfur, selenium and tellurium. Theses glasses are covalently bonded and form stable compound, even though their melting temperature is low compared to silica (between 200°C and 400°C [6.19]). They have a very broad transmission window in MIR, up to 20 µm for Te-based chalcogenide glass, and beyond 10 µm for the commonly used S- and Se-based ones [6.20]. This is due to their low phonon energy, which prevents multiphonon absorption to occur at these wavelengths. Moreover, they can be drawn into fibers thanks to extrusion processes [6.20], or shaped into waveguides via dry etch [6.21] or laser patterning [6.22]. All of this makes them very attractive for applications that require light guiding in MIR, such as astronomy or biosensing [6.23].

On top of these interesting transparency properties, chalcogenide glasses are extremely nonlinear. The nonlinear index can reach a value of the order of 10^{-17} m^2W^{-1} in AsSe glasses of high purity [6.24]. As a consequence, the Kerr effect is massive and allows to perform frequency conversion in C-band, very far from the ZDW [6.25] [6.26], while stimulated Raman [6.27] and Brillouin [6.28] scatterings are also magnified compared to the silica case. Moreover, given the possibility to draw microstructured fibers, of

which waveguide dispersion can compensate for an inappropriate material dispersion, materials such as AsSe and its derivative GeAsSe appear promising. The first one has a bulk ZDW beyond 5 µm while the second one's ZDW is located around 3.5 µm, although these figures can vary depending on the exact glass composition. For this reason, it is of interest to first characterize large core fibers, to extract some properties relative the bulk material. It is especially relevant in the 2 µm region, where our parametric pump for the second stage will be located. We had at our disposal two photonic crystal fibers (PCF), one made of $As_{38}Se_{62}$ (FUT1) and the other of $Ge_{10}As_{22}Se_{68}$ (FUT2). Their characterization protocol is once again identical to that used for the TDF and SiN waveguides characterization and aims at measuring the CE spectrum in SWIR. However, due to their low melting point chalcogenide fibers are still limited to sub-Watt power handling [6.29]. To perform the measurement, we built two CW ring cavity Tm-doped fiber lasers, similar to those presented in [6.30]. The pump and signal were injected in the PCFs either via but coupling them with a SMF-28, or through a lensed fiber. The experimental setup is shown in Fig. 6.7(a), while an example of FWM spectrum near 1980 nm, recorded for 54 mW of pump power injected in FUT1, is depicted in Fig. 6.7(b).

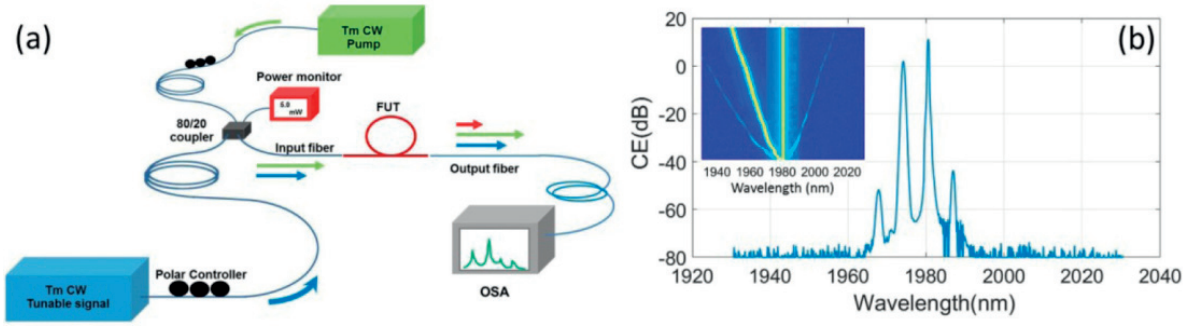

Figure 6.7: (a) Experimental setup used for the characterization of the chalcogenide fibers under test (FUT). (b) Example of FWM spectrum acquired in FUT1 with 54 mW pumping power and a signal power of 6 mW. The inset shows a colormap of the idler generation on the Stokes and anti-Stokes sides for a 1981 nm pump, and a signal swept from 1950 nm to 1978 nm.

We first tested FUT1, which is 31.5 cm long and has the following cross-section properties: the core, defined by a ring of holes arranged in a hexagonal pattern, has a 14 µm diameter, while the external diameter is 125 µm. The air hole diameter d and the pitch distance Λ are measured to be about 3.79 µm and 8.54 µm, respectively. The knowledge of these quantities allows for the waveguide dispersion simulation with a mode solver. The bulk glass index is given by the fiber manufacturer (SelenOptics). The expected GVD curve is shown in Fig 6.8(a), along with an SEM picture of FUT1's cross section. The fiber is expected to be single mode at 2 µm, and the simulations confirm that the ZDW is located far in the MIR (around 5.1 µm). The experimental CE spectra acquired with the abovementioned setup are shown in Fig. 6.8(b), for various power levels of the 1980 nm pump. By normalizing these CE curves to the square

of the pump power, it is possible to fit them to a normalized theoretical CE, which takes the linear attenuation into account. This fitting is presented in Fig. 6.8(c), and the dispersion and nonlinear parameters retrieved at 1980 nm are the following: $D = -336$ ps/nm/km (versus -334 ps/nm/km in the simulation) and a nonlinear coefficient of 0.53 $W^{-1}m^{-1}$. From this value and from the effective area computed with the mode solver, we estimate that $n_2 \approx 7.9 \cdot 10^{-18}$ m^2W^{-1}. This value is very close to that of silicon, however chalcogenide waveguides can be made much longer, and the total insertion loss (in- and out-coupling plus transmission) does not exceed 5 dB.

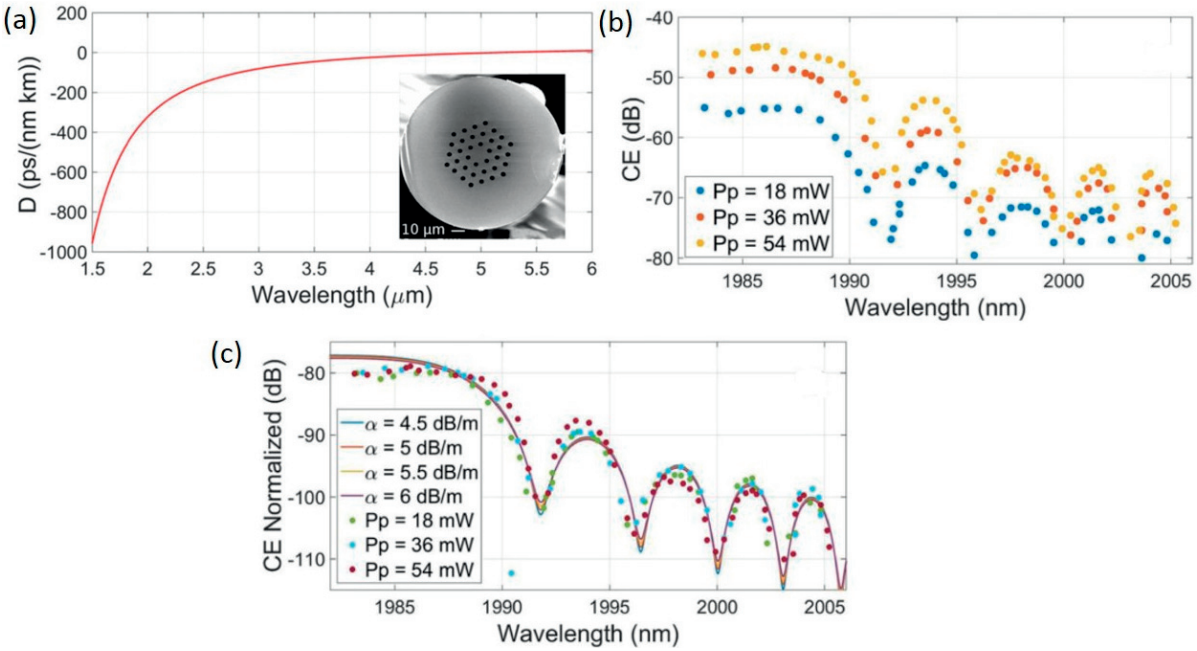

Figure 6.8: (a) Simulated group velocity dispersion (D) as a function of wavelength for FUT1. Inset: SEM image of the fiber cross section. (b) Experimental CE in FUT1 as a function of the idler wavelength for three coupled pump powers. (d) Same CE curves normalized to the square of the pump power (dots), and superimposed to normalized CE fits (solid lines), plotted for various attenuation values given in the legend.

The analysis of data from FUT1 reveals that, in spite of the high AsSe nonlinear index, the efficiency of the FWM process at 2 µm is still limited by the large phase mismatch and by the large A_{eff} which lowers the nonlinear coefficient. Diminishing the PCF core size simultaneously enhances γ and reduces the phase mismatch by blue-shifting the fiber ZDW towards 2 µm. From a technological point of view, low loss chalcogenide PCFs with core diameter smaller than 5 µm are very difficult to draw from AsSe glasses [6.31]. However, it has been shown that inserting a certain amount of germanium in the glass composition allows to draw small core PCFs featuring an attenuation lower than 1 dB/m at 2.5 µm [6.32]. GeAsSe appears a viable option and we therefore computed the dispersion of FUT2 in a similar fashion than FUT1. Its cross section properties are as follow: the core diameter is 4 µm, d is 1.28 µm and Λ is 2.68 µm.

The result is shown in Fig. 6.9(a), along with an SEM picture of the cross section, and indicates a ZDW at 3.015 µm. This value represents a strong improvement with respect to FUT1. The fiber was probed again via FWM for two pump wavelengths, namely 1981 nm and 2008 nm. The resulting CE curves are presented in Fig. 6.9(b) and (c). From the fitting, we find $D = -171$ ps/nm/km at 2008 nm and -183 ps/nm/km at 1981 nm. This is a bit lower than the numerical values, probably due to uncertainties in the bulk index value. For the 1981 nm pumping case, the CE amplitude 6 nm away from the pump is characterized as a function of the injected pump power. The results are presented in Fig. 6.8(d). Once again it was possible to inject more than 100 mW in the fiber to reach a CE of -25.4 dBm without facet or waveguide damage. The corresponding nonlinear parameters are $\gamma \approx 1.69\,\mathrm{W^{-1}m^{-1}}$ and $n_2 \approx 5.3 \cdot 10^{-18}\,\mathrm{m^2W^{-1}}$.

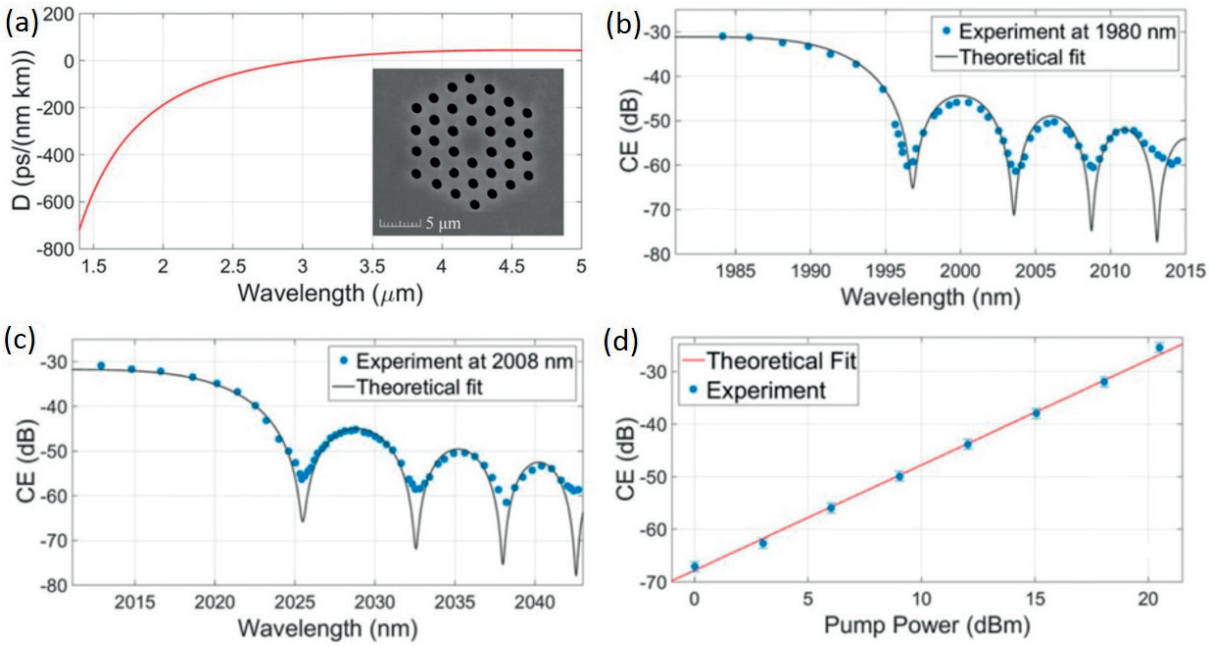

Figure 6.9: (a) Simulated group velocity dispersion curve for FUT2. Inset: SEM image of the fiber cross section. (b) Experimental CE superimposed to theoretical fits as a function of the idler wavelength, for a 100 mW pump at 1981 nm and (c) 2008 nm. (d) CE as a function of the coupled pump power for a 1981 nm pump and pump-signal detuning of 6 nm. Error bars are calculated considering a 0.5 dB uncertainty in the pump power. The red curve is a theoretical fit.

Despite the improved efficiency, the dispersion of FUT2 in SWIR is still too large, and must be compensated by a strong waveguide dispersion. The ZDW of a PCF strongly depends on the diameter-to-pitch ratio $r = {}^{d}/_{\Lambda}$ [6.33], and a raised ratio results in a further ZDW blue-shift. Nonetheless larger diameter-to-pitch ratio also increase the fabrication difficulty, especially with soft glasses. We performed numerical simulations to blue-shift the ZDW of a GeAsSe PCF, and preliminary results showed that varying this ratio alone (within a realistic upper limit of $r = 0.7$) is not sufficient to bring the ZDW down

to 2 µm. On top of this, it is necessary to shrink the core diameter φ, which implies fiber tapering. Assuming that the PCF core diameter can be tapered down to 1.5 µm with a good uniformity, setting $r = 0.66$ results in a ZDW located at 1963 nm, as shown in Fig. 6.10(a). This value is especially interesting since it corresponds to a band where the FOPA-TDFAs presented in the previous chapters perform very well. In comparison, the ZDW for the corresponding un-tapered geometry (4 µm core) is at 2.87 µm. The simulated CE of such a tapered fiber is displayed in Fig. 6.10(c), assuming a taper length of 1 m and an injected pump power of 50 mW at 1953 nm (normal dispersion regime) and at 1964 nm (anomalous regime). At these pump wavelengths, the calculated nonlinear parameter is $\gamma = 9.8\,\mathrm{W^{-1}m^{-1}}$, several times larger than that of FUT2 and of the integrated waveguides mentioned above. A maximum CE of -6 dB is computed for both pumping wavelengths. Nonetheless, the actual conversion efficiency is expected to be lower due to the attenuation in the taper, and to the optical leaks in the transition regions.

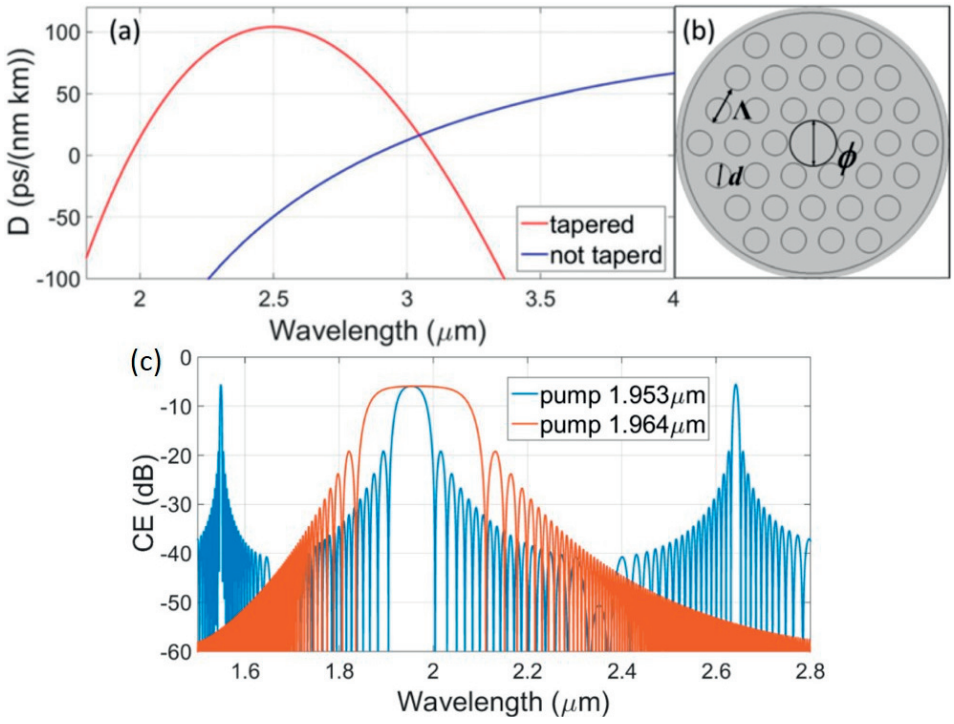

Figure 6.10: (a) Simulated group velocity dispersion for a tapered PCF featuring a 1.5 µm core size (red), and for a non-tapered PCG featuring a 4 µm core size (blue). (b) Structure of the simulated fiber, indicating the design parameters. (c) Simulated CE spectrum in a 1 m long tapered PCF pumped by a 50 mW laser.

By slightly tuning the pump wavelength, it is possible to obtain either a 200 nm wide conversion band around the pump, or a narrow CE lobe located beyond 2.6 µm, all of this with an SWIR pump. Tapered PCF thus theoretically address the need for a high nonlinear coefficient and a ZDW in SWIR. Moreover, compared to suspended core fibers, they exhibit a low number of guided modes. And compared to integrated waveguides, they allow much longer interaction length in relatively robust structures. We

pursued the research effort toward using these PCFs tapers, and CW parametric gain was observed at 2 μm during the redaction of this dissertation, as well as unprecedented CW power handling capabilities for chalcogenide fibers [6.34]. This represents a real breakthrough in this spectral band, and more impressive results are expected after optimization of the fiber dispersion.

6.4. References

[6.1] L. Zhang et al., "Nonlinear Group IV photonics based on silicon and germanium: from near-infrared to mid-infrared," Nanophotonics 3, 247–268 (2013).

[6.2] N. K. Hon et al., "The third-order nonlinear optical coefficients of Si, Ge, and $Si_{1-x}Ge_x$ in the midwave and longwave infrared," J. Appl. Phys. 110(1), 011301 (2011).

[6.3] H. Fukuda et al., "Four-wave mixing in silicon wire waveguides," Opt. Express 13, 4629-4637 (2005).

[6.4] S. Zlatanovic et al., "Mid-infrared wavelength conversion in silicon waveguides using ultracompact telecom-band-derived pump source," Nat. Photonics 4(8), 561–564 (2010).

[6.5] X. Liu et al., "Bridging the Mid-Infrared-to-Telecom Gap with Silicon Nanophotonic Spectral Translation," Nat. Photonics 6(10), 667–671 (2012).

[6.6] G. Z. Mashanovich et al., "Low loss silicon waveguides for the mid-infrared," Opt. Express 19, 7112-7119 (2011).

[6.7] V. R. Almeida et al., "Nanotaper for compact mode conversion," Opt. Lett. 28, 1302-1304 (2003).

[6.8] http://refractiveindex.info/?shelf=main&book=Si&page=Chandler-Horowitz (consulted in November 2016).

[6.9] T. Wahlbrink et al., "Highly selective etch process for silicon-on-insulator nano-devices," Microelectron. Eng. 78-79, 212–217 (2005).

[6.10] K. K. Lee et al., "Effect of size and roughness on light transmission in a Si/SiO2 waveguide: Experiments and model," Appl. Phys. Lett., 77, 1617 (2000).

[6.11] "Method of anisotropically etching silicon" US Patent US 5501893 A.

[6.12] S. Zlatanovic et al., "Mid-infrared wavelength conversion in silicon waveguides pumped by silica-fiber-based source," IEEE J. Sel. Top. Quantum Electron. 18, 612–620 (2012).

[6.13] Q. Lin et al., "Nonlinear optical phenomena in silicon waveguides: Modeling and applications," Opt. Express 15, 16604-16644 (2007).

[6.14] D. J. Moss et al., "New CMOS-compatible platforms based on silicon nitride and Hydex for nonlinear optics," Nature Phot. 7(8), 597–607 (2013).

[6.15] V. Brasch et al., "Photonic chip-based optical frequency comb using soliton Cherenkov radiation," Science 351(6271), 357–360 (2016).

[6.16] M. H. P. Pfeiffer et al., "Photonic Damascene process for integrated high-Q microresonator based nonlinear photonics," Optica 3, 20-25 (2016).

[6.17] D. Grassani et al., "Mid-infrared supercontinuum generation in a SiN waveguide pumped at 1.55 micron," in *Frontiers in Optics 2016*, OSA Technical Digest (online) (Optical Society of America, 2016), paper FTu5D.3.

[6.18] J. M. Dudley et al., "Supercontinuum generation in photonic crystal fiber," Rev. Mod. Phys. 78, 1135–1184 (2006).

[6.19] A. B. Seddon, "Chalcogenide glasses: a review of their preparation, properties and applications," J. Non-Cryst. Solids 184, 44 (1995).

[6.20] G. Tao et al., "Infrared fibers," Adv. Opt. Photon. 7, 379-458 (2015).

[6.21] S. J. Madden et al., "Long, low loss etched As_2S_3 chalcogenide waveguides for all-optical signal regeneration," Opt. Express 15, 14414-14421 (2007).

[6.22] A. Ródenas et al., "Three-dimensional mid-infrared photonic circuits in chalcogenide glass," Opt. Lett. 37, 392-394 (2012).

[6.23] B. Bureau et al., "Chalcogenide optical fibers for mid-infrared sensing," Opt. Eng. 53, 027101 (2014).

[6.24] R. E. Slusher et al., "Large Raman gain and nonlinear phase shifts in high-purity As_2Se_3 chalcogenide fibers," J. Opt. Soc. Am. B 21, 1146-1155 (2004).

[6.25] M. D. Pelusi et al., "Wavelength Conversion of High-Speed Phase and Intensity Modulated Signals Using a Highly Nonlinear Chalcogenide Glass Chip," IEEE Photon. Technol. Lett. 22(1), 3–5 (2010)

[6.26] C.-S. Brès et al., "Continuous-wave four-wave mixing in cm-long Chalcogenide microstructured fiber," Opt. Express 19, 621–627 (2011).

[6.27] M. Duhant et al., "Fourth-order cascaded Raman shift in AsSe chalcogenide suspended-core fiber pumped at 2 μm," Opt. Lett. 36, 2859-2861 (2011).

[6.28] D. Marpaung et al, "Low-power, chip-based stimulated Brillouin scattering microwave photonic filter with ultrahigh selectivity," Optica 2, 76-83 (2015).

[6.29] S. Xing et al., "Characterization and modeling of microstructured chalcogenide fibers for efficient mid-infrared wavelength conversion," Opt. Express 24, 9741-9750 (2016).

[6.30] S. Kharitonov et al., "Kerr nonlinearity of Thulium- doped fiber near 2 μm," in CLEO: Science and Innovations (Optical Society of America, 2015), paper JTu5A. 31.

[6.31] P. Toupin et al., "Small core Ge-As-Se microstructured optical fiber with single-mode propagation and low optical losses," Opt. Mater. Express 2(10), 1359–1366 (2012).

[6.32] H. G. Dantanarayana et al., "Refractive index dispersion of chalcogenide glasses for ultra-high numerical-aperture fiber for mid-infrared supercontinuum generation," Opt. Mater. Express 4(7), 1444–1455 (2014).

[6.33] P. S. J. Russell, "Photonic-crystal fibers," J. Lightwave Technol. 24(12), 4729–4749 (2006).

[6.34] S. Xing et al., "Mid-infrared continuous wave parametric amplification in tapered chalcogenide microstructured fibers," arXiv:1612.00707.

Chapter 7 General conclusion

7.1. Summary

The research work presented in this dissertation was part of the MATISSE project, aiming at prototyping versatile SWIR and MIR sources based on FWM. The setups envisioned in this project all consist of a first parametric stage, based on silica fibers, to down-convert light from the telecom bands (around 1.3 and 1.55 μm) towards SWIR. The second stage targets the same kind of conversion, but with a pump at 2 μm and a signal in the telecom bands, in order to generate light in the MIR atmospheric transmission windows. Most of the experimental work described throughout this dissertation was intended to address the problematics linked to the first conversion stage.

In this respect, we first reviewed some fundamental principles related to linear and nonlinear light propagation in optical fibers. To make the analysis as straightforward as possible, we considered single mode and non-birefringent fibers. As such, we could assume the propagating field to be scalar and quasi-Gaussian. Some explanations were also dedicated to stimulated Brillouin scattering, which is a problematic manifestation of the acousto-optic coupling in optical fibers. It prevents powerful, continuous-wave light to be sent through a fiber, and workarounds must be found to build efficient FOPAs. The physics of light amplification in rare earth-doped fiber was also introduced. Afterwards, we quantitatively reviewed concepts that are proper to broadband parametric conversion, when the pump-idler detuning is of the order of several tens of terahertz. In this regime, dispersion fluctuations originating from fabrication imperfections play a major role. These imperfections come from a non-uniform preform doping or fiber drawing, and tend to broaden and lower the FWM conversion efficiency spectrum.

On the experimental side, we first described the optical characterization of HNLFs and the various methods available to this aim. The one based on four-wave mixing and its spontaneous counterpart, modulation instability, were found to be the best suited for our purpose. The dispersion and nonlinearity of HNLFs and TDFs in different relevant spectral ranges have been precisely characterized thanks to this approach. On top of it, interferometric measurements yielded helpful results to crosscheck the previous evaluations. A HNLF was finally selected to be used in the first FOPA stage, and its performance in terms of FWM efficiency in CW regime were assessed. To make a better use of the parametric pump energy, we then showed that appending a TDF after the parametric converter strongly absorbs the undepleted pump, and reinforces the SWIR idler by several orders of magnitude. An extended setup using a TDF and a HDF is suitable to further shift the conversion band up to 2100 nm. These prototypes proved that rare-earth enhanced parametric conversion is a reliable option to build a SWIR source with a flat tuning band tens of nanometers wide, and an output power up to hundreds of milliwatts.

Afterwards, we reviewed the options to obtain a modulated or pulsed SWIR source based on the same principle. Theoretical limitations, such as phase-to-amplitude coupling in FWM, pump pulse broadening or walk-off between the pump and idler, were devised. Nonetheless we showed that our setup can operate in the picosecond pulse regime, and allows for wavelength-adjustable data transmission towards SWIR in a NRZ-OOK or RZ-OOK format. Wavelength multicasting at 2 μm was also demonstrated. In order to show an alternative to FWM-based frequency conversion, we presented our work on wavelength shifting from telecom bands towards SWIR thanks to Raman scattering. This is a straightforward way to build a broadband source out of a pulsed telecom pump and a HNLF featuring a large normal dispersion at 1.55 μm. The broadband output can then be spectrally sliced to make a wavelength tunable, picosecond pulsed source.

The last part of the dissertation dealt with advanced platforms for the SWIR-to-MIR conversion stage. We first described the fabrication of silicon-on-insulator waveguides, and the issues we encountered in the process. Silicon appeared well suited for nonlinear optics at 2 μm and longer because of its high nonlinear index, its high optical confinement power, and the reduced impact of two-photon absorption for lower photon energy. Nonetheless many problems arose during the fabrication and handling of submicron-scale, unclad waveguides, which forced us to consider other platforms. Buried silicon nitride waveguides are much more robust, while their dielectric nature prevents unwanted carrier excitation at high power. Unfortunately their nonlinearity was found too low for FWM on a chip in CW regime. Nevertheless they showed very promising MIR light generation capabilities under femtosecond pumping, thanks to the emergence of a strong dispersive wave. Finally, we described why chalcogenide fibers may be the best solution to build the second conversion stage. Chalcogenide glasses feature a massive nonlinear index, and they can be drawn into microstructured fibers of all kind. These designs, in conjunction with fiber tapering, theoretically allows for a ZDW shift down to the SWIR. We finally reported very encouraging results concerning parametric amplification at 2 μm in these fibers.

To offer an overview of the project objectives completion, we review in Table 7.1 the performances of the SWIR sources proposed in this dissertation. These performances, obtained both in CW and pulsed regime, are compared with the achievements of current conventional sources, based on mode-locked fiber lasers or semiconductor laser diodes. Our solution offers a unique combination of wavelength tunability, maximum power or pulse energy, and control over the pulse duration. To the best of our knowledge, no conventional laser can feature all these properties at the same time, apart from second-order OPAs. Nonetheless, as stated in the introduction, the latter are bulky and environment-sensitive.

	Criterion	This work	Conventional sources
CW regime	Optical power	>700 mW at 1900 nm. >100 mW at 2000 nm. >10 mW at 2050 nm.	~kW for fixed wavelength TDFLs. ~10 mW for tunable TDFLs. ~mW for single mode diode lasers.
	Wavelength tuning	Full tuning over 1850-2100 nm. ~50 nm for individual setups.	1700-2300 nm for fixed wavelength diode lasers. 1900-2000 nm for tunable TDFLs. Few nm for individual setups.
Pulsed regime	Pulse energy and duration	pJ pulse energy. Duration tunable from ps to ns.	Up to 100s nJ for femtosecond mode-locked TDFLs.
	Wavelength tuning	Full tuning over 1850-2100 nm. ~50 nm for individual setups.	Central wavelength factory defined for Q-switched and mode-locked lasers.

Table 7.1: Comparison between the SWIR sources proposed in this work and conventional solutions.

7.2. Outlooks

As far as the SWIR converter stage is concerned, being able to generate a highly coherent monochromatic output would be of interest in fields such as 2 µm communications, for which noise-free and wavelength tunable emitters are required. Or absorption spectroscopy, where the laser linewidth should ideally be entirely contained in the absorption line bandwidth. To realize a parametric converter able to conserve the coherence properties of the signal and pump seed lasers, stimulated Brillouin scattering must be quenched otherwise than by phase dithering. Waveguide engineering is a viable option. As explained in chapter 2, HNLFs of which dispersion is insensitive to straining exist [7.1]. As such they can be piecewise strained to reduce the SBS threshold, while their ability for broadband FWM is left unaffected. It would be valuable to demonstrate a FOPA-TDFA including such a HNLF. However these fibers apparently feature very little ZDW fluctuations, preventing the CE spectral flattening. The idler tuning would therefore require the adjustment of the pump wavelength [7.2]. In order to retrieve the gain broadening characteristics described in chapter 3, it is conceivable to concatenate pieces of strain-insensitive HNLFs with different ZDWs. Such an assembly would also allow for the conversion of several O-band signals simultaneously, to create a compact wavelength-division multiplexed laser bank at 2 µm.

Still concerning the first FOPA stage applications, reducing the idler wavelength down to 1.7 µm can be interesting for multiphoton microscopy [7.3]. Given that high pulse energies are required in this field, a pulsed setup is the most relevant option. And since the pump-idler detuning is limited for a 1.7 µm output compared to a 2 µm one, dispersion fluctuations should be less impactful. Higher conversion efficiencies

are therefore expected with a properly characterized HNLF. This higher efficiency is necessary, since the thulium fiber gain is far from being as efficient at 1.7 μm as it is at 1.9 μm [7.4]. Fortunately, in a pulsed pump scheme, Brillouin scattering is quenched. Thus long HNLF can be used to boost the CE. This also renders possible the use of Raman scattering to amplify the FWM efficiency, either in the HNLF or in an additional fiber. Since the Raman Stokes detuning is about 100 nm at the wavelengths of concern, a 1.6 μm pump would suit perfectly this design.

As far as the second parametric stage is concerned, the development of SWIR and MIR optics is full of promises. If the distant conversion itself turns out to work robustly in chalcogenide fibers, it should be possible to fabricate a rugged prototype approaching industry standards. For instance, development efforts should focus on the interface between the silica and chalcogenide waveguides, in order to reliably splice or glue them after alignment. And for applications requiring a simple continuous-wave MIR output, the substitution of the first-stage converter by a wavelength stabilized thulium- or holmium-doped fiber laser may also improve the overall source robustness.

7.3. References

[7.1] http://fiber-optic-catalog.ofsoptics.com/item/optical--fibers/highly-nonlinear-fiber-optical-fibers1/hnlf-spine-zdw-1540 (consulted in January 2017).

[7.2] B. P.-P. Kuo et al., "Continuous-wave, short-wavelength infrared mixer using dispersion-stabilized highly-nonlinear fiber," Opt. Express 20, 18422-18431 (2012).

[7.3] N. G. Horton et al., "In vivo three-photon microscopy of subcortical structures within an intact mouse brain," Nat. Photonics 7(3), 205–209 (2013).

[7.4] Z. Li et al., "Exploiting the short wavelength gain of silica-based thulium-doped fiber amplifiers," Opt. Lett. 41, 2197-2200 (2016).

Adrien BILLAT

Avenue d'Echallens 134
1004 Lausanne, Switzerland
+41 76 278 70 37

Experience

2017 – present: Fiber network engineer, CERN (Geneva, Switzerland)

2013 – 2017: Research Assistant, EPFL (Lausanne, Switzerland)

- Prototyping of versatile mid-infrared fiber lasers based on frequency conversion. Fabrication and characterization of photonic integrated waveguides for nonlinear optics.

- Undergrad teaching and graduate student supervision, scientific equipment procurement and maintenance

2012 – 2013: R&D intern, MBDA (Paris, France)

- Master thesis: design and prototyping of real-time computational geometry algorithms. Earned best possible grade.

2011: LabVIEW developper, Saphir Signal Physique et Instrumentation (Chambéry, France)

- Implementation of a plug-in to interface Matlab and the company's data analysis solution.

Education

2013 – present: PhD in Electrical Engineering
EPFL (Lausanne, Switzerland)

- Thesis research: design of mid-infrared laser sources based on parametric frequency conversion. Acquired an extensive hands-on experience with laser systems, optical and RF instrumentation, multiphysics software modelling, cleanroom processes and research projects planning.

- Post-thesis work on SiN integrated waveguides for nonlinear optics. Theoretical training in laser physics, laser material processing, photonic semiconductor physics and microfabrication technologies.

2011 – 2013: MSc in Electrical Engineering
EPFL (Lausanne, Switzerland)

- Master thesis: design and implementation of an algorithm to compute surface-trajectory intersections in real time. Prototyping in Matlab and Java. Semester project: Multiphysics modelling of an acoustic metamaterial transmission line with Comsol.

2009 – 2013: Diplôme d'Ingénieur in Electrical Engineering
Supélec (Paris, France)

- General cursus in electrical engineering and information technology, following two undergraduate years in physics. Fundamental training in control engineering, electrical machines, analog and digital electronics.

Technical expertise

- **Fiber and integrated optics**: optical communications, waveguide physics, on-chip and silicon photonics.

- **Lasers**: fiber laser design, laser mode-locking, laser spectroscopy, semiconductor lasers, laser operation and safety.

- **Clean room microfabrication**: electron beam (ebeam) lithography, reactive ion etching (RIE), wet etching, photolithography, scanning electron microscopy (SEM).

- **Radio-frequency** (RF) instrumentation: signal generation, handling and analysis.

- **Physical modelling**: Comsol Multiphysics, equation solvers programming.

- **Programming and CAD**: Matlab, LabVIEW, Java, L-Edit IC Layout, basics of SolidWorks.

Languages
Full working proficiency: **English** (C1), **French** (C2).
Limited working proficiency: **German** (B1-B2, in progress).
Notions: **Spanish** (A2)

Status
French citizen, 27 years old.

Publication record

Journal articles:

- **A. Billat**, S. Cordette, Y.-P. Tseng, S. Kharitonov, C.-S. Brès, “High power parametric conversion from near to short wave infrared,” Optics Express 22, 14341 (2014).
- **A. Billat**, S. Cordette, C.-S. Brès, “Broadly tunable source around 2050 nm based on wideband parametric conversion and thulium–holmium amplification cascade,” Optics Express 22, 26635 (2014).
- **A. Billat**, S. Cordette, C.-S. Brès, “Versatile High Repetition Rate 2-μm Pulsed Source Based on Wideband Parametric Conversion,” IEEE Journal of Lightwave Technology 34, 879 (2015).
- S. Xing, D. Grassani, S. Kharitonov, **A. Billat**, C.-S. Brès, "Characterization and modeling of microstructured chalcogenide fibers for efficient mid-infrared wavelength conversion," Optics Express 24, 9741 (2016).
- S. Kharitonov, **A. Billat**, C.-S. Brès, "Kerr nonlinearity and dispersion characterization of core-pumped thulium-doped fiber at 2 μm," Optics Letters 41, 3173 (2016).
- **A. Billat**, D. Grassani, M. Pfeiffer, S. Kharitonov, T. Kippenberg, C.-S. Brès, “Large second harmonic generation enhancement in SiN waveguides by all-optically induced quasi phase matching,” arXiv:1701.03005 (2017).
- C. Herkommer, **A. Billat**, D. Grassani, H. Guo, M. Pfeiffer, C.-S. Brès, T. Kippenberg, “Mid-infrared dispersive wave generation in silicon nitride nano-photonic waveguides,” arXiv:1704.02478 (2017).

Peer-reviewed conference proceedings:

- **A. Billat**, S. Cordette, Y.-P. Tseng, C.-S. Brès, "Thulium Assisted Parametric Conversion from Near to Short Wave Infrared," CLEO, San Jose (2014).
- S. Cordette, **A. Billat**, Y. P. Tseng and C.-S. Brès, "Tunable Thulium-assisted parametric generation of 10 Gb/s intensity modulated signals near 2 μm," The European Conference on Optical Communication (ECOC), Cannes, (2014).
- S. Cordette, **A. Billat**, Y. P. Tseng and C.-S. Brès, "Widely Tunable Picosecond-Pulsed Source near 2 μm based on Cascaded Raman Wavelength Shifting," The European Conference on Optical Communication (ECOC), Cannes, (2014)
- S. Cordette, S. Kharitonov, **A. Billat**, C.-S. Brès. “High Power Sub-Picosecond Pulsed SWIR Source Based on Thulium Assisted Raman Wavelength Shifting,” Optical Fiber Communication Conference (OFC), Los Angeles (2015).
- D. Grassani, S. Xing, S. Kharitonov, **A. Billat**, S. Cordette, A. Vedadi, and C. Brès, "Continuous wave four-wave mixing at 2 micron in Chalcogenide microstructured fiber," Advanced Solid State Lasers, Berlin (2015).
- **A. Billat**, S. Cordette, C.-S. Brès, “2 microns all-fiber picosecond pulse source with gigahertz repetition rate” CLEO Europe, Munich (2015).
- **A. Billat**, S. Cordette, C.-S. Brès, “Wavelength Multicasting and Amplification of 5 Gb/s Data in the 2 Micron Band,” Optical Fiber Communication Conference (OFC), Los Angeles (2016).
- S. Xing, D. Grassani, S. Kharitonov, **A. Billat**, C.-S. Brès, " Small core Chalcogenide photonic crystal fiber for midinfrared wavelength conversion: experiment and design," CLEO, San Jose (2016).
- D. Grassani, **A. Billat**, M. Pfeiffer, H. Guo, T. North, T. Kippenberg, C.-S. Brès, “Mid-infrared supercontinuum generation in a SiN waveguide pumped at 1.55 micron,” Frontiers in Optics, Rochester (2016).
- C. Herkommer, H. Guo, **A. Billat**, D. Grassani, M. Pfeiffer, M. Zervas, C.-S. Brès, T. Kippenberg, “A Chip-based Silicon Nitride Platform for Mid-Infrared Nonlinear Photonics,” CLEO, San Jose (2017).

- D. Grassani, **A. Billat**, M. Pfeiffer, S. Kharitonov, T. Kippenberg, C.-S. Brès, “All-optically induced quasi phase matching in SiN waveguides for second harmonic generation enhancement,” CLEO, San Jose (2017).